CuAg bimetallic nanoparticles for the electrochemical reduction of carbon dioxide

Dissertation

Submitted in partial fulfilment for the degree of Master of Science in Chemical Engineering

Prepared by:

Gcinisizwe Dlamini

Supervised by:

Prof. Patricia Kooyman

A/Prof. Pieter Levecque

Department of Chemical Engineering

Catalysis Institute

University of Cape Town

October 2020

“Get wisdom, get understanding; do not forget my words or turn away from them...”

- *Proverbs 4:5*

Acknowledgements

I am grateful that I went on this journey to explore worlds within and outside of myself. I am grateful to the Chemical Engineering Department for growing my curiosity since I began my university journey in 2014. In particular, thank you to the Catalysis Institute for building a culture of collaboration among students and academics.

To Patricia Kooyman, thank you so much for supporting me from the day I entered your office in 2017. You have spent early mornings teaching me how to use the TEM. You have challenged my approaches on numerous occasions, teaching me to see patterns, and embedding within me lessons from your rich experience. Thank you.

To Pieter Levecque, I am in awe as to how great it has been to learn from you. My first encounter with you was when you first took me through Thermodynamics I. Since then and now, your passion for the wellbeing of students sits at such a close place in your heart. Thank you for taking the time with me, we have spent so many hours troubleshooting reactors and having edifying scientific discussions.

To Mohamed at the Electron Microscope Unit, I have learnt so much from you about life, and of course how to better operate the TEM.

I wish to gratefully acknowledge the Centre for High Resolution Transmission Electron Microscopy, especially Dr. J.E. Olivier and Dr. J.H. O'Connell, at Nelson Mandela University (NMU) in Port Elizabeth for their assistance and use of their facilities.

I wish to thank the Mandela Rhodes Foundation for seeing within me a spirit of education, entrepreneurship, reconciliation, and leadership. I would like to thank the whole organisation for funding my studies and for gifting me with the book 'The Native Commissioner' by Shaun Johnson, which has shaped large parts of my life.

To my family, my mother Nonhlanhla, my father Bernard, and my siblings Tenkhosi and Lungelo Dlamini, I thank you for your undying support throughout this journey. I appreciate you all.

To Lindelwa Sambo. We have been counting stones together, since the day we met in 2012. I really thank you for being a voice of reason. Thank you for having endless discussions with me on nanoparticles and for pushing yourself to understand. Above all else, I thank you for being present Lindelwa Sambo.

Synopsis

The electrochemical reduction of carbon dioxide is a surface reaction, involving the conversion of carbon dioxide and water to hydrocarbons and oxygenates in an electrolytic environment. This reaction grants an opportunity for the rerouting of carbon dioxide from expulsion to the atmosphere towards the production of chemical products. Due to the stable C-O bond in carbon dioxide, this reaction requires a catalyst and an external energy source to activate it. The use of renewable energy as an energy source would ensure that the electrochemical reduction process is carbon neutral.

Cu has been identified as a promising catalyst for the electrochemical reduction of carbon dioxide, as it is more active and produces higher amounts of hydrocarbons and oxygenates relative to other transition metals,. However, Cu is unselective towards a specific product, and it highly active for the undesirable hydrogen evolution reaction (Kuhl et al., 2014). On the other hand, under electrochemical conditions, Ag yields mainly CO, which has been shown to compete with the hydrogen evolution reaction (Hori, Murata & Takahashi, 1989).

This study focuses on the synthesis of different ratios of CuAg bimetallic nanoparticles, and their electrocatalytic performance evaluation for the electrochemical reduction of carbon dioxide. Bimetallic nanoparticles were synthesised via a wet chemical method using two synthesis routes. One synthesis was performed in the presence of hexadecylamine (HDA), surfactant, while the other was performed in its absence. The electrocatalytic performance evaluation was conducted using two reactors, a batch reactor with a gas diffusion electrode, and a rotating disc electrode reactor.

It was found that catalysts synthesised in the absence of HDA had a phase-separated atomic arrangement, forming islands of Cu and Ag. On the other hand, synthesis conducted in the presence of HDA culminated in a CuAg solid solution.

The two synthesis routes resulted in catalysts that had distinct product distributions. Catalysts prepared in the absence of HDA predominantly formed formate, with catalysts that had a higher Cu content forming methanol and CO. The yield of formate for catalysts synthesised under the absence of HDA did not decline at higher potentials relative to Cu catalysts which suffered from hydrogen production. On the other hand, bimetallic catalysts synthesised in the presence of HDA demonstrated behaviour similar to monometallic catalysts. Catalysts with a higher Cu content predominantly produced formate, while catalysts with a high Ag content produced a CO rich stream.

This study indicates a profound dependency of the catalyst activity and product distribution on the CuAg bimetallic ratio and atomic arrangement. This study adds knowledge on the synthesis of CuAg

bimetallic nanoparticles, and the design of catalysts for the electrochemical reduction of carbon dioxide.

Contents

Acknowledgements ii

Synopsis iii

List of Figures ix

List of Tables xiii

Nomenclature xiv

- Symbols xiv
- Glossary xiv
- Chemicals xv

1 Chapter 1 – Introduction 1

2 Chapter 2 - Literature Review 3

- 2.1 Technologies for the reduction of carbon dioxide: Hydrogen gas vs H^+ ion technology 3
  - 2.1.1 Sabatier process 3
  - 2.1.2 Electrochemical reduction of CO_2 3
- 2.2 Reactions in the electrochemical reduction of carbon dioxide 5
- 2.3 CO_2RR Mechanism 5
  - 2.3.1 Formation of C_1 products 7
  - 2.3.2 Formation of C_{2+} hydrocarbons and oxygenates 8
- 2.4 Performance of transition metal catalysts in the CO_2RR 9
  - 2.4.1 Performance of transition metals based on CO adsorption 9
  - 2.4.2 Transition metals selectivity towards hydrocarbons vs alcohols 10
- 2.5 Copper as a catalyst for CO_2RR 12
  - 2.5.1 Trends in product distribution on Cu as an electrocatalyst 12
  - 2.5.2 The role of copper oxides on CO_2RR 13
- 2.6 Trends in Ag product distribution 14
- 2.7 Bimetallic catalysts 15
- 2.8 Geometric and electronic effects of bimetallic catalysts 16
- 2.9 Strategies in limiting the Hydrogen Evolution Reaction (HER) 18

2.10 Nanoparticle nucleation and growth 20

2.11 Cu and Ag nanoparticles synthesis routes 21

2.11.1 Chemical reduction 21

2.11.2 Laser irradiation 22

2.11.3 Thermal decomposition 22

2.11.4 Microemulsion 22

2.11.5 Electrodeposition 23

2.12 Electrochemical cells for CO_2RR nanoparticle evaluation 23

2.12.1 Flow cell with gas diffusion electrode 23

2.12.2 Batch cell with a gas-diffusion electrode 25

2.12.3 Electrochemical cell with rotating ring disc electrode 26

2.13 Electrochemical cell standard conditions 27

3 Chapter 3 – Objectives and key questions 28

3.1 Research objectives 28

3.2 Key Questions 28

4 Chapter 4 – Methodology 30

4.1 CuAg nanoparticles synthesis 30

4.1.1 Method A 30

4.1.2 Method B 31

4.2 Investigation of washing procedure 32

4.3 Deposition of nanoparticles onto carbon support 32

4.4 Physical Characterisation 33

4.4.1 Transmission Electron Microscopy (TEM) 33

4.4.2 Powder X-ray Diffraction (PXRD) 34

4.4.3 Energy Dispersive X-ray spectroscopy (EDX) 34

4.4.4 Thermogravimetric Analysis (TGA) 34

4.5 Electrocatalytic characterisation with gas diffusion electrode 35

4.5.1 Overview of electrochemical cell setup 35

4.5.2 Electrochemical cell design 35

4.5.3 Catalyst ink preparation and spraying on GDE 36

4.5.4 Electrocatalytic evaluation procedure 38

4.6 Characterisation and quantification of products 39

4.6.1 Gas products 39

4.6.2 Liquid products identification and quantification 40

4.6.3 Computation of electrochemical performance 40

4.7 Electrocatalytic characterisation with rotating ring disc electrode 41

4.7.1 Cell setup 42

4.7.2 RRDE ink and electrode preparation 42

4.7.3 Electrochemical products calibration 43

4.7.4 RRDE cyclic voltammetry 43

5 Chapter 5 – Results and Discussion 45

5.1 Development of synthesis methodology for CuAg bimetallic nanoparticles 45

5.1.1 CuAg nanoparticle growth series 45

5.1.2 Influence of precursor concentration and temperature on nanoparticle morphology 46

5.1.3 Nanoparticle deposition on carbon support 49

5.2 Catalysts Physical Characterisation 50

5.2.1 Monometals physical characterisation 50

5.2.2 Method A bimetallic catalysts physical characterisation 54

5.2.3 Method B bimetallic catalysts physical characterisation 59

5.3 Development of batch reactor 65

5.3.1 Improvement of cell design 65

5.3.2 Initial catalytic evaluation 66

5.4 Catalyst evaluation in RRDE setup 67

5.4.1 Electrochemical calibration of Pt ring electrode 67

5.4.1 Monometallic catalyst evaluation 69

5.4.2 Method A catalyst evaluation 72

5.4.3 Method B catalyst evaluation 75
5.5 Comparison of catalytic performance of Method A and Method B 78
6 Conclusion 80
7 Recommendations 82
7.1 Nanoparticle synthesis and characterisation 82
7.2 Electrochemical batch reactor evaluation 82
7.3 Rotating ring disc electrode 83
8 Appendices 84
8.1 Effect of storage on bimetallic nanoparticles 84
8.2 GC TCD calibration 84
9 List of references 85

List of Figures

Figure 2-1: Illustration of the reduction of carbon dioxide in a one-unit electrochemical cell at ambient pressure and temperature 4

Figure 2-2: Proposed mechanisms for the formation of C_1 and C_2+ compounds in the electrochemical reduction of carbon dioxide. (a) Adapted from Hori, Murata & Takahashi (1989) , (b) Adapted from Schouten et al. (2011) (c) Adapted from Nie et al. (2013) (d) Adapted from Garza, Bell & Head-Gordon (2018). 7

Figure 2-3: Volcano plot of CO_2RR current density at -0.8 V vs RHE for metals with CO binding strength on. Adapted from Kuhl et al. (2014). 10

Figure 2-4: CO_2RR Products' FEs at various applied potentials [V vs RHE] on a Cu electrocatalyst. Adapted from a study by Hori, Murata & Takahashi (1989). 12

Figure 2-5: Performance of Cu based catalysts prepared under various conditions: (a) Current densities at various potentials (b) Ethylene FE at various potentials. Adapted from Mistry et al. (2016). 14

Figure 2-6: Reduction products FEs on Ag electrocatalyst, at various potentials in a 0.1M KHCO3 electrolyte. Adapted from Hatsukade et al. (2014). 15

Figure 2-7: Various atomic arrangements of CuPd electrocatalysts (Ma et al., 2017). 17

Figure 2-8: Product FE efficiency over applied potential range for CuPd (1:1) with ordered, disordered, and phase separated mixing patterns. Replotted from Ma et al. (2017). 18

Figure 2-9: Illustration of the LaMer mechanism model. Redrawn from Polte (2015). 20

Figure 2-10: Electrolytic cell with gas diffusion electrode. Adapted from Jeanty et al. (2018). 24

Figure 2-11: Expansion of the gas-diffusion electrode. 24

Figure 2-12: Illustration of a 1L batch electrochemical cell with a gas-diffusion electrode, adapted from Geschiere (2014). 25

Figure 2-13: Three cell electrode with an expansion of the rotating disc electrode, adapted from Zhu et al. (2018). 26

Figure 4-1: Electrocatalytic evaluation setup. 35

Figure 4-2: Electrochemical cell design adapted from work by Geschiere (2014). 36

Figure 4-3: An expanded view of the cathode of the electrochemical cell. 36

Figure 4-4: Prona ® Air spray RH-CP used to spray catalyst layer onto GDE. 37

Figure 4-5: Catalyst ink spraying pattern on gas diffusion layer. 37

Figure 4-6: An illustration of the gas ampoule sampler 39

Figure 4-7: Illustration of rotating disc electrode, (a) concentric view with dimensions, (b) axial view illustrating the flow direction of electrolyte due to electrode rotation. 42

Figure 5-1: Time series of the growth of nanoparticles during synthesis. **A**: 15 mins (after the last drop of $NaBH_4$), **B**: 45 mins, **C**: 1h. 46

Figure 5-2: CuAg(50:50) nanoparticles synthesised at different precursor concentrations and 0 °C, after 1 h. Total metal concentration: (a) 1.25 mM, (b) 3.5 mM, (c) 7.0 mM. 47

Figure 5-3: CuAg(50:50) nanoparticles synthesised at different temperatures, and a fixed precursor concentration of 3.5 mM for 1h. (a) 0 °C, (b) 25 °C, (c) 50 °C. 48

Figure 5-4: X-ray diffractograms of CuAg(50:50) synthesised under different temperature conditions. 48

Figure 5-5: The effects of washing with various solvents, with each round of washing performed for 15 minutes with stirring at 500 rpm. (a) washing with ethanol, followed by water, and then acetone, (b) washing with acetone, (c) washing with water, (d-1): one round of washing with ethanol, (d-2): two rounds of washing with ethanol. 49

Figure 5-6: CuAg(50:50) supported on carbon after washing and drying in an oven operated at 60 °C. 50

Figure 5-7: TEM images of as-prepared and supported bimetallic nanoparticles prepared in the presence of HDA at 0°C (Method B). 51

Figure 5-8: Particle size distribution histograms for as prepared and supported monometallic nanoparticles synthesised via Method B. 52

Figure 5-9: X-ray Diffraction of CuAg(100:0)/C_B, and CuAg(0:100)/C_B 53

Figure 5-10: CuAg(1:0)/C, CuAg(0:1)/C, and Vulcan (XC-72R) Thermogravimetric analysis profile. Performed at a ramp rate of 5˚C/min in air which was fed at a rate 10 ml/min. 53

Figure 5-11: TEM images showing as-prepared and supported bimetallic nanoparticles prepared in the absence of HDA at 0°C (Method A). 55

Figure 5-12: Particle size distribution histograms for as prepared and supported nanoparticles, synthesised via Method A. 56

Figure 5-13: X-ray diffractogram of bimetallic samples synthesised via Method A. 57

Figure 5-14: CuAg(20:80)/C_A, CuAg(50:50)/C_A, CuAg(80:20)/C_A and Vulcan (XC-72R) Thermogravimetric analysis profile. Performed at a ramp rate of 5˚C/min in air which was fed at a rate 10 ml/min. 58

Figure 5-15: TEM images showing as-prepared and supported bimetallic nanoparticles prepared in the presence of HAD (Method B) 60

Figure 5-16: Particle size distribution histograms for as prepared and supported nanoparticles, synthesised via Method B. 61

Figure 5-17: High angle annular dark field (HAADF) scanning electron microscope (STEM) images, and energy dispersive X-ray (EDX) mapping indicating O, Cu, and Ag mapping of carbon supported CuAg nanoparticles synthesised via Method B. 63

Figure 5-18: X-ray diffractogram of bimetallic samples synthesised in the presence of HDA. 64

Figure 5-19: Thermogravimetric plots of nanoparticles supported on Vulcan XC-72R. Performed at a ramp rate of 5˚C/min in air which was fed at a rate of 10 ml/min. 64

Figure 5-20: Illustration of electrode housing during cell leakage test. (a) Electrode chamber without the addition of silicon carbide (b) Electrode chamber with silicon carbide. 65

Figure 5-21: Cyclic voltammetry of monometallic catalysts and empty GDE under CO_2RR conditions. This was done in the range -0.4 and -1.10 V vs RHE, at a scan rate of 50 $mV.s^{-1}$. 66

Figure 5-22: Pt-ring cyclic voltammetry scans for calibration of CO_2RR products in CO_2-saturated 0.1M $NaHCO_3$. Cyclic voltammetry scans were performed between 0 and 1.3V vs RHE, at a scan rate of 50 $mV.s^{-1}$, and rotation of 1500 rpm. (a) Blank cyclic voltammetry with no species added (b) Carbon monoxide (c) Potassium formate (d) Methanol. 69

Figure 5-23: Cyclic voltammetry scans of the RRDE in Ar and CO_2 conditions. The disk electrode containing supported monometallic nanoparticles was cycled between 0 and -1.7 V vs RHE. The Pt-ring electrode was held at a potential of 0.9 V vs RHE. Scan rate: 100 $mV.s^{-1}$, constant rotating speed of 1500 rpm 70

Figure 5-24: Cyclic voltammetry scans of the Pt-ring electrode, while holding the disc electrode at fixed potentials. Pt-ring scanned between 0 and 1.3 V vs RHE. Scan rate: 100 $mV.s^{-1}$, constant rotating speed of 1500 rpm. The disc has deposited monometallic catalysts, CuAg(100:0)/C_B and CuAg(0:100)/C_B. 72

Figure 5-25: Cyclic voltammetry scans of the RRDE in Ar and CO_2 conditions. The disk electrode containing supported CuAg bimetallic nanoparticles prepared via Method A was cycled between 0 and -1.7 V vs RHE. The Pt-ring electrode was held at a potential of 0.9 V vs RHE. Scan rate: 100 $mV.s^{-1}$, constant rotating speed of 1500 rpm. 73

Figure 5-26: Cyclic voltammetry scans of the Pt-ring electrode, while holding the disc electrode at fixed potentials. Pt-ring scanned between 0 and 1.3 V vs RHE. Scan rate: 100 $mV.s^{-1}$, constant rotating speed of 1500 rpm. The disc has deposited bimetallic catalysts prepared via Method A. 74

Figure 5-27: Cyclic voltammetry scans of the RRDE in Ar and CO_2 conditions. The disk electrode containing supported CuAg bimetallic nanoparticles prepared via Method B was cycled between 0 and -1.7 V vs RHE. The Pt-ring electrode was held at a potential of 0.9 V vs RHE. Scan rate: 100 $mV.s^{-1}$, constant rotating speed of 1500 rpm. 76

Figure 5-28: Cyclic voltammetry scans of the Pt-ring electrode, while holding the disc electrode at fixed potentials. Pt-ring scanned between 0 and 1.3 V vs RHE. Scan rate: 100 mV.s^{-1}, constant rotating speed of 1500 rpm. The disc has deposited bimetallic catalysts prepared via Method B. 77
Figure 5-29: Proposed mechanism, adapted from Hatsukade et al. (2014). 79
Figure 8-1: CuAg (50:50)/C_A nanoparticles after storage for 3 months. 84

List of Tables

Table 2-1: The standard potentials of the main reactions occurring at the cathode of the electrochemical cell, sourced from Qiao et al. (2014) 5

Table 2-2: Product selectivity (%) over Ag-Co electrocatalyst, from Singh et al. (2017). 17

Table 5-1: Expected and actual metal loading of monometallic catalysts. These were obtained from TGA analysis. 54

Table 5-2: SEM EDX results of various ratios of supported nanoparticles prepared via Method A. 56

Table 5-3: Expected and actual metal loading of bimetallic catalysts prepared via Method A. These were obtained from TGA analysis. 58

Table 5-4: SEM EDX results of various ratios of supported nanoparticles prepared via Method B. 61

Table 5-5: Expected and actual metal loading of bimetallic catalysts prepared via Method B. These were obtained from the TGA analysis. 65

Table 8-1: GC-TCD calibration data and response factors 84

Nomenclature

Symbols

Symbol	**Unit**	**Description**
g	-	Gram
FE	%	Faradaic efficiency
I	mA	Current
θ	°	Bragg angle
β	-	Peak width
λ	nm	Wavelength

Glossary

Abbreviation	**Description**
CO_2RR	Carbon dioxide electrochemical reduction reaction
CuAg (x:y)_Z	As prepared copper silver bimetallic nanoparticles prepared via method Z. x and y are the copper and silver molar ratios added to the nanoparticle synthesis vessel.
CuAg(x:y)/C_Z	Copper silver bimetallic nanoparticles supported on carbon prepared via method Z. x and y are the copper and silver molar ratios added to the nanoparticle synthesis vessel.
DFT	Density Functional Theory
FID	Flame Ionisation Detector
GDE	Gas Diffusion Electrode
HDA	Hexadecylamine
HPLC	High Performance Liquid Chromatography
HER	Hydrogen Evolution Reaction
GC	Gas Chromatography
NMU	Nelson Mandela University
RHE	Reversible Hydrogen Electrode
Rpm	Revolutions per minute
RRDE	Rotating Ring Disc Electrode
TCD	Thermal Conductivity Detector
TEM	Transmission Electron Microscope

TGA	Thermogravimetric analysis
XRD	X-ray Diffraction

Chemicals

Symbol	**Description**
Ag	Silver
$AgNO_3$	Silver nitrate
Ar	Argon
Au	Gold
CH_3OH	Methanol
CO	Carbon monoxide
CO_2	Carbon dioxide
Cu	Copper
CuAc	Copper Acetate
$Cu(NO_3)_2.3H_2O$	Copper nitrate trihydrate
H_2	Hydrogen
N_2	Nitrogen
Ni	Nickel
Pd	Palladium
Pt	Platinum
Zn	Zinc

1 Chapter 1 – Introduction

Fuels and chemicals that drive the global economy can potentially be produced via the electrochemical reduction of CO_2, which can occur at room temperature and atmospheric pressure (Hori et al., 1988). As this process requires energy input, intermittent renewable energy such as solar and wind can be coupled to this process, thus allowing for renewable energy to be stored in the form of chemical bonds.

The electrochemical reduction of CO_2 offers a carbon-neutral route for renewable energy storage. Electrochemical reduction of CO_2 is characterised as a surface reaction between carbon dioxide and water which occurs in an electrolytic medium to form hydrocarbons and/or oxygenates. Due to the stability of the carbon to oxygen bond (750 $kJ.mol^{-1}$), carbon dioxide reduction requires a catalytic site and an external energy source, in which renewable energy is proposed. This reaction also provides an alternative route towards the utilisation of carbon dioxide, rather than its direct release to the atmosphere.

In studies of the electrochemical reduction of CO_2, various transition metal electrocatalysts have been explored. The current challenges of these electrocatalysts are that at low overpotentials most of the current is dedicated towards the undesired hydrogen evolution reaction (HER) rather than the formation of hydrocarbons or oxygenates, and they require operation at high overpotentials to produce a desired product yield.

Recent work has identified CO as a key intermediate for the electrochemical reduction of CO_2. Kuhl et al. (2014) modelled the activity of transition metals based on their CO binding strength. It was observed that metals such as Pt and Ni, which have a high CO adsorption strength, are poisoned by the CO intermediate, culminating into the production of a H_2-rich stream through the competing HER. On the other hand, elements such as Ag, Au, and Zn, which have a low CO adsorption strength, will instead produce a CO-rich stream. Amongst these transition metals, copper, which has an intermediate CO binding strength, has been the most attractive as it produces hydrocarbons with a Faradaic efficiency (FE) greater than 50% (Hori et al., 1988). However, copper still suffers from producing undesired H_2 at low overpotentials — which is the desired operating range in the electrochemical cell.

In the electrochemical reduction of carbon dioxide, bulk transition metals have been used as a potential electrocatalyst. However, nanostructured particles have shown higher carbon dioxide reduction reaction (CO_2RR) activity and selectivity (Manthiram, Beberwyck & Alivisatos, 2014). Additionally, nanostructured particles allow for better control of particle composition and morphology (Ferrando, Jellinek & Johnston, 2008). The most common nanoparticle synthesis method is the wet chemical method, which involves the introduction of metal precursors in solution, followed by their reduction using a reducing agent (Quang Huy, Van Quy & Anh-Tuan, 2013). The wet chemical method may also be performed in the presence of a surfactant which aids in controlling particle morphology.

This current study investigates the synthesis of various ratios of CuAg bimetallic nanoparticles and evaluates their potential as catalysts in the electrochemical reduction of carbon dioxide. The performance of the prepared bimetallic catalysts is contrasted with control experiments of monometallic Cu and Ag nanoparticles. The nanoparticles are synthesised through the wet chemical method while the effect of hexadecylamine (capping and reducing agent) on nanoparticle morphology and composition is investigated. Two reactor setups were utilised in evaluating the nanoparticle catalytic properties: a gas diffusion electrode coupled to a gas chromatograph, and a rotating disc electrode (RRDE). On the RRDE, reaction products are identified through their immediate oxidation.

2 Chapter 2 - Literature Review

This section will review literature regarding the electrochemical reduction of carbon dioxide. It will also give a review of various cathode electrocatalysts and reactors that have been employed for this reaction, and the factors that influence their performance. Then finally, it will grant an overview of various catalyst synthesis methods.

2.1 Technologies for the reduction of carbon dioxide: Hydrogen gas vs H^+ ion technology

2.1.1 Sabatier process

There has been a growing interest in the reduction of CO_2, as it provides an alternative to its release into the atmosphere by converting it to useful chemicals or fuels. The Sabatier process is one of these reduction methods. It involves the production of hydrogen gas via electrolysis, through the water-splitting reaction. This hydrogen is then fed to a reactor where it reacts with carbon dioxide through the catalytically enhanced Sabatier reaction to form methane (Brooks et al., 2007). In this process, methane yields and selectivities of 26% and 96%, respectively, have been reported (Guerra et al., 2018). The drawback of this process is that it requires multiple process units, with the main reaction occurring at mild conditions, at pressures between 1 to 8 bar, a temperature range between 180 ˚C to 240 ˚C, and it requires H_2 gas as a feedstock, which is produced from energy intensive processes (Brooks et al., 2007).

2.1.2 Electrochemical reduction of CO_2

Hori et al. (1988) were the first to show that reduction of carbon dioxide to ethylene and methane can be performed on a copper electrode at ambient temperature and pressure in an aqueous electrolyte. The advantage of this process over the Sabatier process is that the reduction of carbon dioxide can be performed in one unit - an electrochemical cell - shown in Figure 2-1.

The overall chemical transformation, as illustrated in Figure 2-1, is:

$$CO_2 + H_2O \rightarrow C_xH_yO_z + O_2 \qquad (2\text{-}1)$$

Which is the sum of the following half-cell reactions. Water oxidation (oxygen evolution reaction, OER):

$$H_2O \rightarrow O_2 + 4H^+ + 4e^- \qquad (2\text{-}2)$$

and the carbon dioxide reduction reaction (CO_2RR):

$$yCO_2 + zH^+ + ne^- \rightarrow C_yH_aO_b + cH_2O \qquad (2\text{-}3)$$

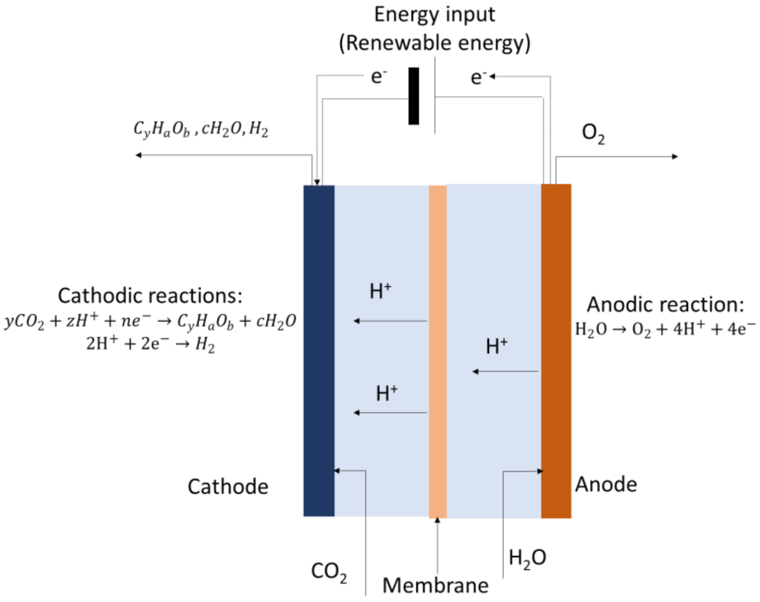

Figure 2-1: Illustration of the reduction of carbon dioxide in a one-unit electrochemical cell at ambient pressure and temperature.

The electrochemical cell has two electrodes, the cathode and anode, which are both in contact with a proton conducting electrolyte, as illustrated in Figure 2-1. The overall process involves the generation of H^+ ions at the anode, which migrate through a proton selective membrane to the cathode of the cell (see equation (2-2)). At the anode, an oxygen evolution reaction (OER) catalyst is used to generate H^+ ions, with platinum primarily being used due to its electrochemical stability (Hori et al., 1988). At the cathode, the CO_2 is reduced by a catalytic electrode referred to as an electrocatalyst. This CO_2RR involves the adsorption of CO_2 onto the catalyst surface forming various intermediates which react with H^+ ions to form hydrocarbons and/or oxygenates (Hori et al., 1988). The most pronounced and desired products on copper electrodes are ethylene, methane, and methanol (Kuhl et al., 2014). However, for reaction (2-3) to proceed, it requires an external energy source to drive the reaction at the cathode as indicated in Figure 2-1. To ensure that this process is carbon-neutral, renewable energy is proposed as an energy source.

The performance of an electrocatalyst in an electrochemical cell is usually measured using two factors: current density and Faradaic Efficiency (FE). The current density describes the amount of charge transferred throughout the entire reaction process, and it indicates the activity of the catalyst. The FE of a product represents the total current required to produce a certain amount of that product relative to the total current passed throughout the electrochemical reduction experiment, and it is an indication of the catalyst's selectivity towards that product.

2.2 Reactions in the electrochemical reduction of carbon dioxide

Table 2-1 below compliments Figure 2-1 and shows the potential reactions that could occur at the cathode of the electrochemical cell. From a thermodynamic perspective, Table 2-1 indicates that CH_4 should be the first and simplest hydrocarbon that forms, forming at 0.169 V_{SHE} (Peterson & Nørskov, 2012). However, these potentials do not give an indication of the kinetics of the reactions. Current studies have shown that to enhance the yields of hydrocarbons and oxygenates, electrocatalysts require operations at an excess voltage than the thermodynamic potential (Qiao et al., 2014). This excess voltage is referred to as the overpotential. Since the hydrogen evolution reaction (HER) occurs at 0.0 V_{SHE} at standard conditions, it is expected to be a competing reaction to CO_2RR at negative potentials (Peterson & Nørskov, 2012). Another competing reaction that should be noted is carbon monoxide formation. Additional to the desired reactions shown in Table 2-1, Kuhl et al. (2014) has shown that copper electrocatalysts are capable of forming other carbonyls, such as aldehydes and ketones, although at low concentrations.

Table 2-1: The standard potentials of the main reactions occurring at the cathode of the electrochemical cell, sourced from Qiao et al. (2014)

Cathode half-cell reaction	Electrode potential vs SHE under standard conditions (V)
$2H^+ + 2e^- \rightarrow H_2(g)$	0.00
$CO_2(g) + 2H^+ + 2e^- \rightarrow CO(g) + H_2O\ (l)$	-0.106
$CO_2(g) + 6H^+ + 6e^- \rightarrow CH_3OH(l) + H_2O\ (l)$	0.016
$CO_2(g) + 8H^+ + 8e^- \rightarrow CH_4(g) + 2H_2O\ (l)$	0.169
$2CO_2(g) + 12H^+ + 8e^- \rightarrow CH_2CH_2(g) + 4H_2O\ (l)$	0.064

The commercial viability of this process hinges on an electrocatalyst that is active and selective to a specific product, operating at a low overpotential while producing desired products at a high current density and limiting the production of undesired products.

2.3 CO_2RR Mechanism

Understanding the reaction mechanism for the CO_2RR to hydrocarbons and/or oxygenates is vital in the design and synthesis of new electrocatalysts. This is because the formation of certain products is primarily influenced by the interaction of reaction intermediates with the catalyst surface, and the catalyst's ability to stabilise certain reaction intermediates (Peterson & Nørskov, 2012). A comprehensive reaction mechanism should be able to explain the observed product distribution. However, at this stage, the mechanism for the CO_2RR is still under debate. This section aims to amalgamate commonalities and contrast differences in the reaction mechanisms that have been proposed thus far. It is worth noting that most of the work in proposing new reaction mechanisms has been performed on copper electrocatalysts. These proposed reaction mechanisms based on experiments conducted on copper also offer insight about possible reaction pathways on other transition metals (Hori, Murata & Takahashi, 1989). Studies on decoupling the reaction mechanism have been based on Density Functional Theory (DFT), while others have been based on feeding possible reaction intermediates into the electrochemical cell. The various proposed reaction mechanisms are presented in Figure 2-2.

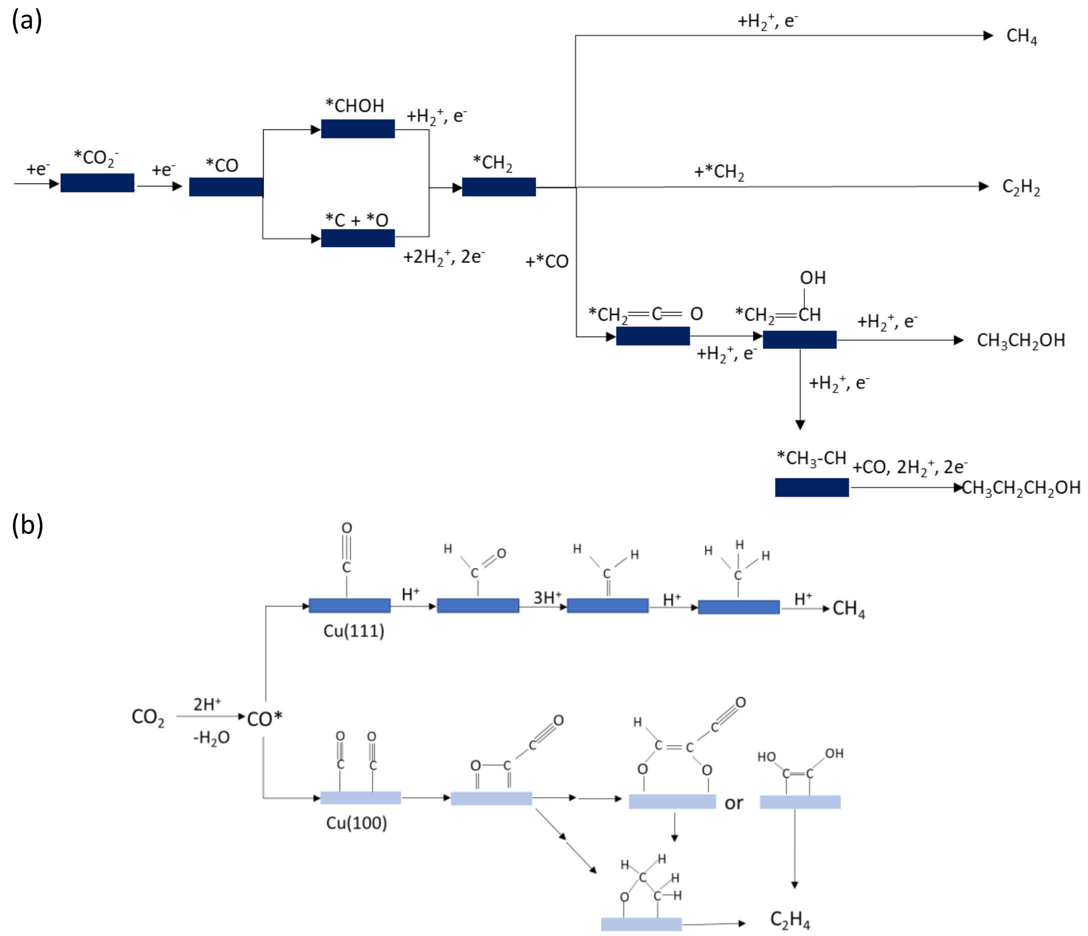

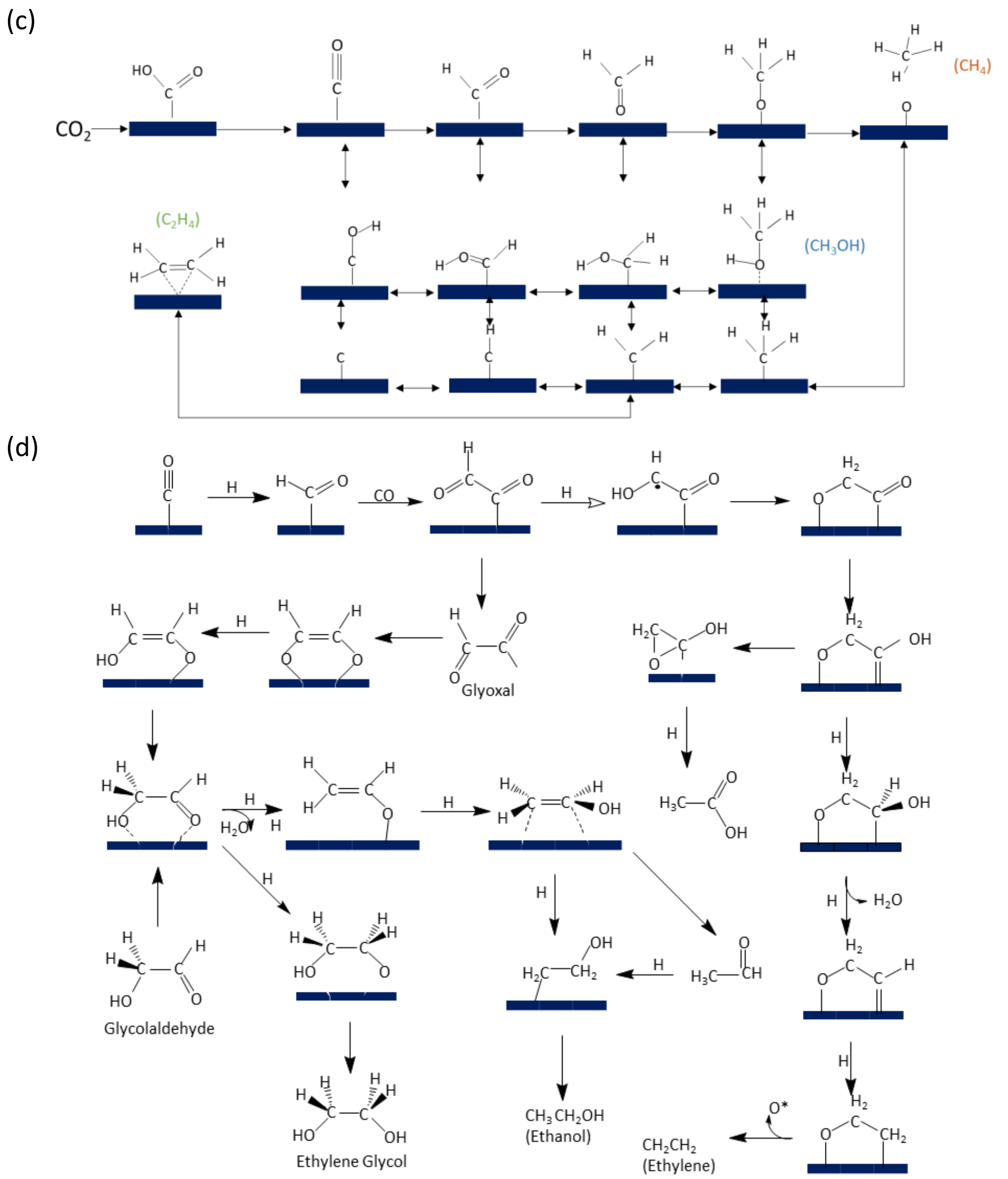

Figure 2-2: Proposed mechanisms for the formation of C_1 and C_2+ compounds in the electrochemical reduction of carbon dioxide. (a) Adapted from Hori, Murata & Takahashi (1989) , (b) Adapted from Schouten et al. (2011) (c) Adapted from Nie et al. (2013) (d) Adapted from Garza, Bell & Head-Gordon (2018).

2.3.1 Formation of C_1 products

Hori, Murata & Takahashi (1989) proposed a Fischer-Tropsch like mechanism for the CO_2RR on a copper electrode, as shown in Figure 2-2(a). The formation of C_1 products is proposed to be through the adsorption of CO_2 onto the catalyst, where it is deoxygenated to CO (Hori, Murata & Takahashi (1989), Schouten et al. (2011), and Garza, Bell & Head-Gordon (2018). The CO formation pathway involves the hydrogenation of CO_2 to form a formic acid intermediate, which upon deoxygenation forms CO as illustrated in Figure 2-2(c). The formation of CO through the formate route is in agreement with DFT studies by Peterson & Nørskov (2012). Both formate and CO can desorb from the catalyst surface as products. At low potentials (below -0.8V_{RHE}), FEs of 20% on a Cu catalyst have been reported for formate and CO. Alternatively, adsorbed CO can be hydrogenated to form *CHOH or deoxygenated to form atomic carbon, which both lead to the formation of the -CH_2- monomer, whereupon protonation forms methane (CH_4). The hydrogenation of *CO to *CHOH weakens the C-O bond, allowing for easy cleaving of the oxygen (Peterson & Nørskov, 2012) to form CH_4. Alternatively, the hydrogenation of the *CHOH intermediate gives rise to methanol (CH_3OH) formation. The formation of methanol or methane extends to other transition metal electrocatalysts, such as Au, Ag, Fe, and Ni have been shown to produce significant amounts of these products (Kuhl et al., 2014). Hori, Murata & Takahashi (1989) attributed the formation of methanol to the presence of Cu_2O films on the catalyst surface. The role of Cu_2O in the electrochemical cell is explored in section 2.5.2.

2.3.2 Formation of C_{2+} hydrocarbons and oxygenates

Schouten et al. (2011) have proposed that two distinct reaction pathways occur on Cu(111) and Cu(100) facets, which are illustrated in Figure 2-2(c). Electrochemical reduction of carbon dioxide was performed on Cu(111), and Cu(100) single crystal electrodes, and the proposed mechanism is illustrated in Figure 2-2 (b). From the experimental work, it was shown that Cu(100) yields ethylene (C_2H_4) as the predominant product, while Cu(111) yields a methane (CH_4) rich product stream. These differences in product distribution of these two facets are consistent with experimental findings by Hori et al. (2002).

The C-C bond formation, which leads to C_{2+} products, is proposed to occur via three routes: CO-CO dimerization, CHO-CO coupling, and -CH_2- to -CH_2- or CO coupling. It should be noted that CO is a common intermediate towards the formation of C_{2+} products.

In the Fischer-Tropsch like mechanism proposed by Hori, Murata & Takahashi (1989), ethylene formation occurs through the coupling of two CH_2 moieties, or through CH_2 and CO insertion. The CH_2 and CO insertion route in this mechanism is also speculated to lead to the formation of aldehydes and alcohols.

The CO dimerization route involves the hydrogenation of *COCO to form *COCOH, which upon further reduction forms a vinyl alcohol species (*CH_2=CHO). The reduction of adsorbed vinyl alcohol culminates into the formation of ethylene and ethanol. Ethylene is formed through the cleaving of the C-O bond, whilst hydrogenation of the vinyl alcohol species leads to the formation of acetaldehyde and ethanol. In comparison, the coupling of CHO and CO leads to the formation of *COCHO. Reduction of *COCHO leads to the formation of COCHOH, which is a pathway towards ethylene or glyoxal formation as well as a pathway towards the formation of ethylene glycol and ethanol, as illustrated in Figure 2-2(c). DFT studies have shown that both the CO dimerization and the CHO-CO coupling route are both plausible routes towards the formation of C_{2+} products, with the former being dominant at low overpotentials, whilst the latter is dominant at high overpotentials (Goodpaster, Bell & Head-Gordon, 2016).

The formation of the CHO* intermediate is not limited to Cu, as Pd, Ni, Au and Ag have been shown to stabilise this intermediate (Peterson & Nørskov, 2012). However, other transition metals such as Pt and Rh, which have a strong CO binding strength, are in contrast proposed to form the COH* intermediate rather than the CHO* intermediate, because of the non-availability of the carbon electrons (Peterson & Nørskov, 2012).

Even though there still exists a debate on the exact mechanism for the electrochemical reduction of carbon dioxide, work by Schouten et al. (2011), Kuhl et al. (2014), Peterson & Nørskov (2012), and Hori, Murata & Takahashi (1989) has highlighted CO as a common intermediate towards the formation of both C_1 and C_{2+} hydrocarbons. The proposed mechanisms by Schouten et al. (2011), Hori, Murata & Takahashi (1989), and Garza, Bell & Head-Gordon (2018) suggests that an increased coverage of adsorbed CO would lead to a higher yield for C_{2+} hydrocarbons.

2.4 Performance of transition metal catalysts in the CO_2RR

2.4.1 Performance of transition metals based on CO adsorption

Various transition metal electrocatalysts have been explored for the reduction of carbon dioxide. These transition metals can be divided into two groups based on their ability to reduce CO – a key CO_2RR intermediate. These two groups are shown in Figure 2-3, which shows the volcano plot of transition metal CO_2RR current density plotted against their CO binding strength. The current density follows a volcano trend, with the transition metals on the left reflecting metals with a strong CO binding energy, whilst elements on the right have a weak CO binding energy. The first group of transition metals has been reported to produce a H_2-rich stream, whilst the second group of transition metals produces a CO rich stream (Kuhl et al., 2014).

DFT indicates that the group of transition metals on the right of Figure 2-3 bind CO weakly, such that it is released without further reduction to hydrocarbons and/or oxygenates (Peterson & Nørskov, 2012). In contrast, the second group of transition metals, which includes Ni, Pt, and Fe, strongly bind the CO intermediate culminating in a high CO coverage on the catalyst surface (Peterson & Nørskov, 2012). This strong CO adsorption leads to the poisoning of the catalyst surface, limiting the further reduction of CO on the catalyst surface, and through carbon to carbon steric hindrances inhibits more CO_2 from readsorbing on the catalyst surface (Peterson & Nørskov, 2012). On these catalyst surfaces, the competitive HER becomes the dominant reaction, resulting in hydrogen being the most pronounced product. Cu has an intermediate CO binding strength, and amongst transition metals, it has shown the highest activity and selectivity towards hydrocarbons and oxygenates. However, Cu still suffers from significant H_2 formation.

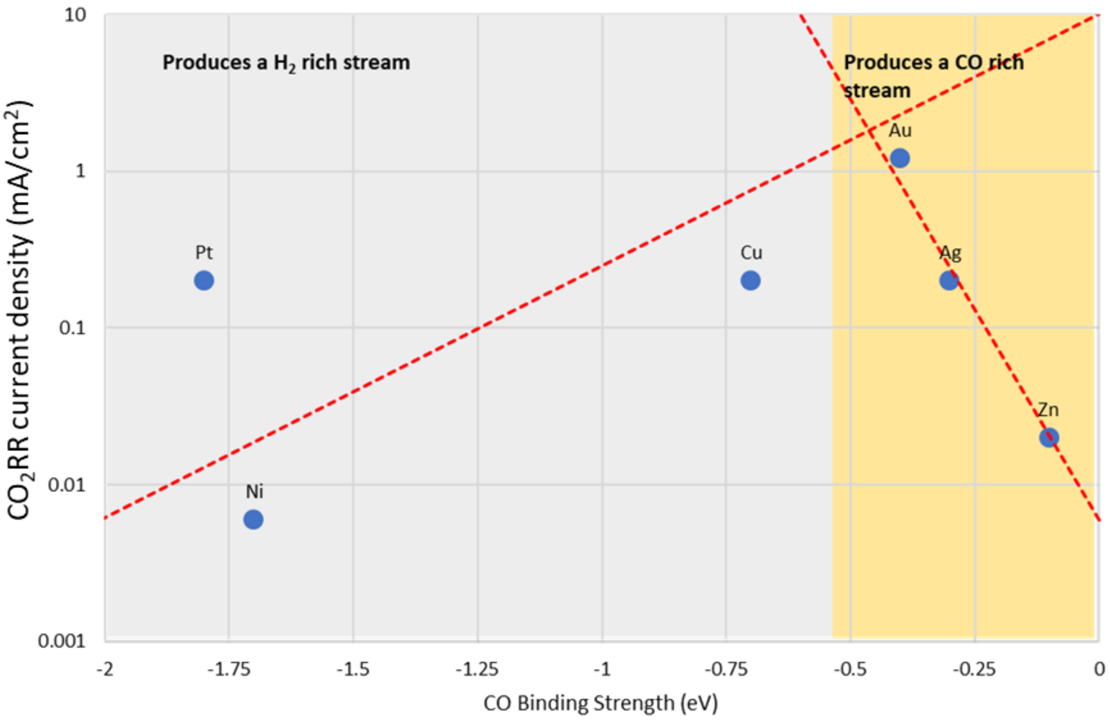

Figure 2-3: Volcano plot of CO_2RR current density at -0.8 V vs RHE for metals with CO binding strength on. Adapted from Kuhl et al. (2014).

2.4.2 Transition metals selectivity towards hydrocarbons vs alcohols

This section will discuss the factors that determine the selectivity of hydrocarbons vs. alcohols, as for example Kuhl et al. (2014) report that the yield of methane is four times that of methanol on Cu surfaces.

It had been widely thought in previous studies that transition metals, apart from Cu, are only capable of producing carbon monoxide, hydrogen and/or formate (Kuhl et al., 2014). However, studies have shown that Au, Ag, Zn, Ni, Pt, and Fe are also capable of producing further reduced products, such as methane and/or methanol (Kuhl et al., 2014). This correlates with DFT studies by Peterson & Nørskov

(2012) which aimed to predict the methane onset potential on various transition metals. In this study, it was revealed that Rh, Pt, Pd and Ni, which strongly bind the *CO intermediate, can yield methane at high overpotentials. This occurs through the protonation of *CO to form the *COH intermediate, which can be further reduced to methane. However, from a mechanistic perspective, Peterson & Nørskov (2012) did not offer insight on the ability of metals with a weak CO binding strength, such as Au, Ag, and Zn, to produce methane and/or methanol as reported by Kuhl et al. (2014).

In CO_2 electrochemical reduction using Au nanoparticles as an electrocatalyst, Dohyung et al. (2014) identify carbon monoxide and hydrogen as the only reduction products. However, Dohyung et al. (2014) performed experiments up to a limited overpotential of -1.1 V_{RHE}, while Kuhl et al. (2014) show that by working at an extended potential of -2.0 V_{RHE}, Au electrocatalysts produce methanol and methane. In addition to this, Kuhl et al. (2014) show that by increasing the sensitivity of the Gas Chromatography (GC) and Nuclear Magnetic Resonance (NMR), trace amounts of methanol and methane formation can be detected using a Au electrocatalyst.

By investigating the tendency of other metals being able to produce methanol, Kuhl et al. (2014) offer insight towards the design of electrocatalysts which are selective to methanol or methane production. By relating the oxygen binding energy of transition metal electrocatalysts towards their methane and methanol yield, Kuhl et al. (2014) produced a volcano trend akin to Figure 2-3. The results show that elements that have a low oxygen binding energy form a large amount of methanol relative to methane. For example, Au, which has the least oxygen affinity of the evaluated transition metals produces, only methanol and no methane (Kuhl et al., 2014). Coupled with this, oxyphilic elements were reported to produce a large amount of methane relative to methanol. This was to the extent that Fe, which has a strong oxygen binding energy, was found to produce only methane and no methanol (Kuhl et al., 2014). This finding is vital because it proposes that if it is desired to produce methane, an oxyphilic catalyst site should be used, whilst to produce methanol, the oxyphilicity of the catalyst should be minimised.

Schouten, Perez Gallent & Koper (2013) show that methanol and methane have the same onset potential at varying pH conditions, within the range -0.8V and -0.9V. This suggests that they undergo the same rate determining step, thus methanol and methane follow the same reaction pathway. Kuhl et al. (2014) propose that this pathway involves oxygen being cleaved from a C-O intermediate at a later stage in the reaction mechanism. This is supported by Peterson & Nørskov (2012), who state that if oxygen were to be cleaved early in the reaction mechanism, the addition of oxygen at a later stage in the reaction mechanism would be a thermodynamically highly energetic step. Therefore, early cleaving of the oxygen is the least likely step.

2.5 Copper as a catalyst for CO_2RR

Figure 2-3 indicates that from all metals that were evaluated, Au had the highest activity for CO_2RR. However, Au has low hydrocarbons and oxygenates selectivity, and produces a CO rich product stream, as it has a weak CO binding strength. In contrast, Cu which has a slightly higher CO binding energy relative to Au produces significant amounts of methane and methanol. This is because of its intermediate binding energy which allows Cu to further reduce CO rather than it being desorbed from the catalyst surface (Peterson & Nørskov, 2012). To confirm these observations Dohyung et al. (2014) show that on Au, CO FE reaches a maximum of 65% and is the major product at normal CO_2RR operating potential. Whilst on Cu, the hydrocarbon FE is usually greater than 50% (Peterson & Nørskov, 2012). Copper is a unique electrocatalyst due to its high selectivity towards hydrocarbon production.

2.5.1 Trends in product distribution on Cu as an electrocatalyst

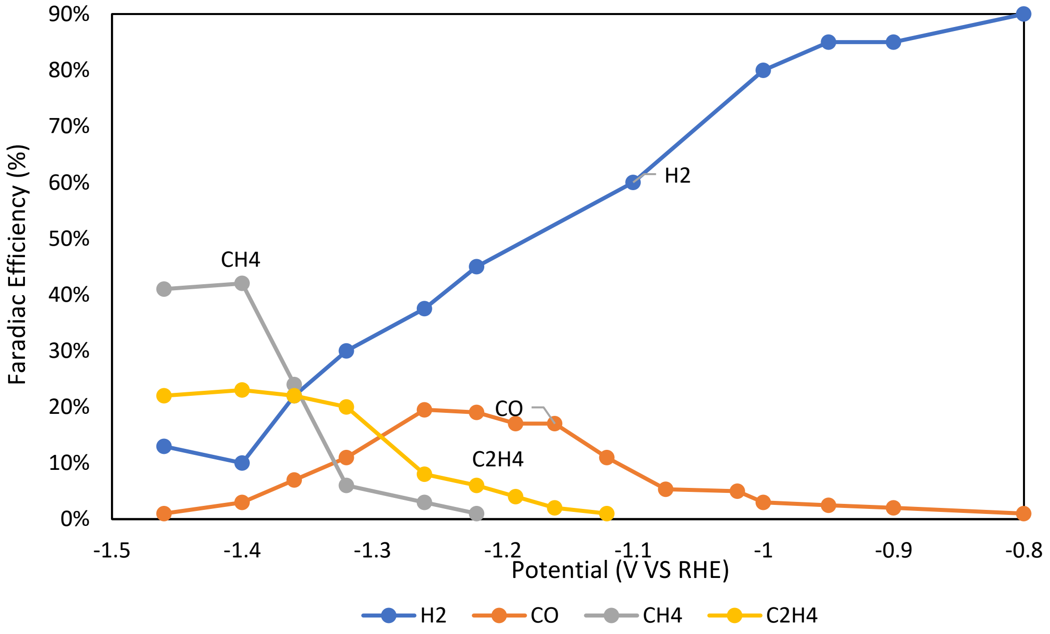

Figure 2-4: CO_2RR Products' FEs at various applied potentials [V vs RHE] on a Cu electrocatalyst. Adapted from a study by Hori, Murata & Takahashi (1989).

Figure 2-4 shows the dependency of reduction products' FEs on the applied potential. At potentials close to -0.8 V_{RHE}, the HER is the most pronounced reaction, culminating in a H_2-rich product stream. Increasing the overpotential leads to an increase in CO formation, which begins to rise at -0.9 V_{RHE}. At more negative potentials, as the CO formation rises, hydrogen evolution begins to drop. Hori, Murata & Takahashi (1989) have attributed this to the increased CO coverage on the copper catalyst surface, which limits the HER. This competition between the CO_2RR and the HER is clear, as an increase in the CO formation correlates to a decrease in hydrogen formation at potentials below -1.4V_{RHE}. The competitive formation of CO and H_2 has also been reported by Kuhl et al. (2014). The increased production of CO increases the coverage of CO on the catalyst surface, and further reduction of adsorbed *CO leads to the formation of hydrocarbons on the catalyst surface (Hori, Murata & Takahashi, 1989). This is supported by the observation that an increase in CO production precedes the formation of ethylene and methane as shown at a potential of -1.1 V in Figure 2-4.

In comparison to the equilibrium potentials shown in Table 2-1, Figure 2-4 shows that the copper electrode requires operation at high overpotentials – further away from equilibrium – in order to produce a significant amount of ethylene and methane.

2.5.2 The role of copper oxides on CO_2RR

Copper is susceptible to oxidation in air to CuO and/or Cu_2O (Hung, Ling-I et al., 2010). It is thus vital to evaluate the role of copper oxides during the electrochemical reduction. In the CO_2RR, it is unclear whether copper oxides are active in the reaction.

Li & Kanan (2012) argue that oxidising the copper electrode, followed by in-situ reduction in an electrochemical cell, leads to an increase in the activity of the copper electrode. Li & Kanan (2012) state that the activity is dependent on the initial thickness of the Cu_2O before reduction in the electrochemical cell. It is also claimed that a thick Cu_2O film may reduce the overpotential of the Cu electrocatalyst by up to 0.5 V.

The increase in activity of the Cu catalyst is also consistent with work by Mistry et al. (2016). In this study, an electropolished polycrystalline Cu foil was exposed to either O_2 or H_2 plasma treatment of varying power and duration. After O_2 plasma treatment, three distinct regions in the catalyst were observed via elemental mapping and EDS: Cu rich, Cu_2O, and CuO. Following the CO_2RR, it was observed that oxygen was depleted on the catalyst surface, resulting in only Cu rich and Cu_2O rich regions remaining. Figure 2-5 (a) indicates that the presence of oxygen species on the catalyst surface after O_2 plasma treatment leads to an increase in the activity of catalyst. In addition to this, Figure 2-5

(b) indicates that the presence of oxygen species on the catalyst surface also leads to an increase in ethylene selectivity, and an early ethylene onset potential relative to the electropolished Cu foil. Therefore, based on these observations, the study by Mistry et al. (2016) concludes that both Cu^0 and Cu^+ species are active in CO_2RR.

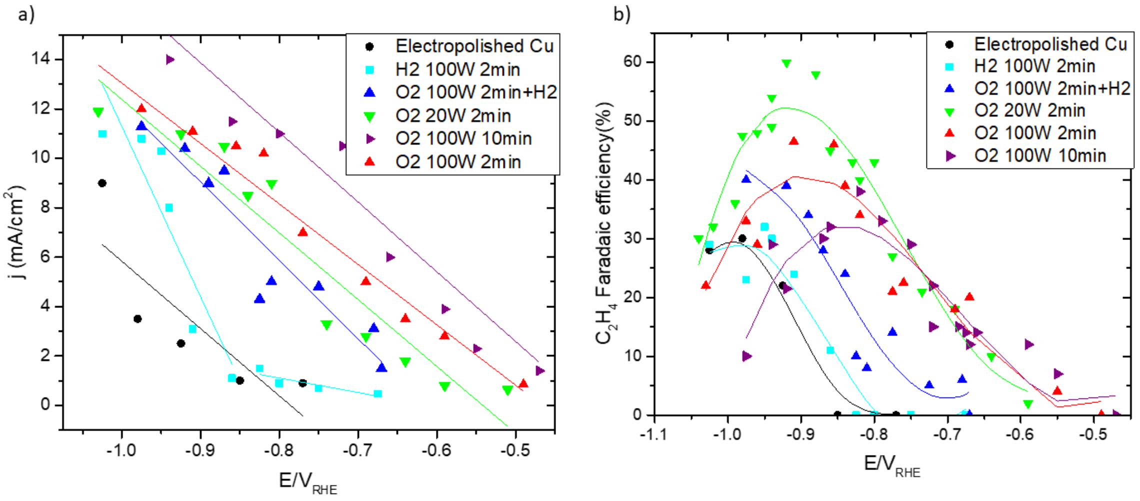

Figure 2-5: Performance of Cu based catalysts prepared under various conditions: (a) Current densities at various potentials (b) Ethylene FE at various potentials. Adapted from Mistry et al. (2016).

The mechanism of copper oxides in CO_2RR remains unexplained. An ethylene onset potential for copper oxides relative to pure copper was observed by Kas et al. (2014). However, electrodes studies by Kas et al. (2014), were prepared by the electrodeposition of Cu_2O on copper electrodes. Relative to the work by Li & Kanan (2012), the Cu_2O film was not reduced to pure copper prior to the commencement of the electrochemical reduction of carbon dioxide. This work observed that O_2 plasma treated Cu had a higher ethylene selectivity relative to a pure copper foil. Kas et al. (2014) noted that reduction of carbon dioxide did not occur on Cu_2O sites, but rather appeared on Cu^0 sites. In addition to this, work by Le et al. (2011) showed that electrodeposited Cu_2O on a copper electrode, lead to the formation of significant amounts of methanol relative to a pure copper electrode.

2.6 Trends in Ag product distribution

Figure 2-3 reveals that Ag weakly binds CO, hence under CO_2RR conditions, it is predicted to elute a CO rich stream with limited further reduction of CO to final products.

The product distribution of Ag as an electrocatalyst is shown in Figure 2-6 over a wide range of applied potential. This figure can be divided into three potential regions: low overpotential (-0.6 V to -1.0 V vs RHE), intermediate overpotential (-1.0 V to -1.2 V vs RHE), and high overpotential (-1.2 V to -1.4 V vs

RHE). In all three potential regions, the combined FEs for CO and H_2 are above 90%. In the low overpotential region, the HER dominates over CO formation. Moving towards more negative potentials culminates in a drop in H_2 production and a rise in CO production. In the intermediate potential region, the production of CO dominates over H_2 production. This also correlates to the formation of formate ($HCOO^-$), which does not exceed a FE of 7% (Hatsukade et al., 2014). In the high overpotential region, the HER rises again, whilst CO production is limited. However, in the high overpotential region, there is a rise in the rate of CO reduction relative to CO desorption (Hatsukade et al., 2014). Thus, with CO as a key reaction intermediate, the production of methane, methanol and ethanol can be observed. The alternating rise and fall of CO and H_2 production in the three regions further shows that the competitive formation of H_2 and CO production exists not only on Cu catalysts, as observed by Hori, Murata & Takahashi (1989), but Ag catalysts also display this phenomenon. At a potential of -1.0 V, the Ag catalyst has a maximum CO FE of 90%. In contrast, a Cu catalyst only achieves a maximum CO FE of 20%, at a larger overpotential of -1.2 V, as indicated by Figure 2-6.

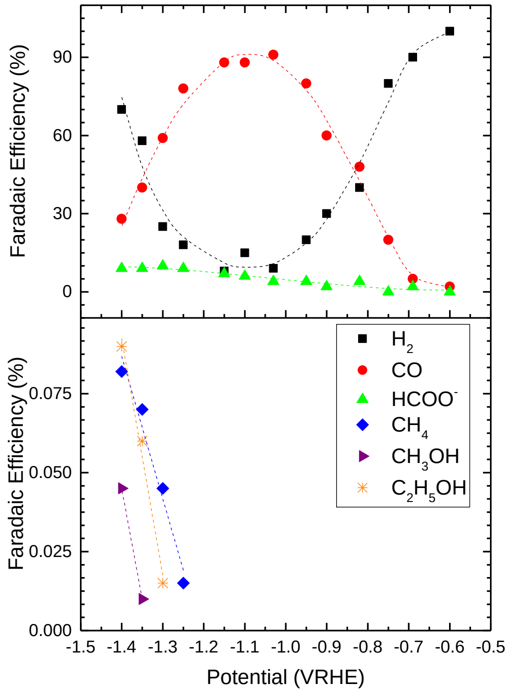

Figure 2-6: Reduction products FEs on Ag electrocatalyst, at various potentials in a 0.1M $KHCO_3$ electrolyte. Adapted from Hatsukade et al. (2014).

2.7 Bimetallic catalysts

Most studies in the field of electrochemical reduction of carbon dioxide have made use of bulk transition metals as electrocatalysts. Recent studies have shown that monometallic nanoparticles show superior activity and selectivity profiles relative to their bulk transition metals (Manthiram, Beberwyck & Alivisatos, 2014). Nanoparticles are defined as particles in the size range 1-100 nm.

From investigating the performance of transition metals, monometallic catalysts have not been shown to yield high activities whilst improving selectivity and limiting the HER. It is proposed that a synergy of the properties of the various monometallic catalysts leads to improved catalytic performance (Chen & Holt-Hindle, 2010). Through the tuning of the bimetallic nanoparticle composition and mixing patterns, the chemical properties can be altered, such that they hold distinct properties relative to their pure monometallic nanoparticles (Ferrando, Jellinek & Johnston, 2008).

Mixing patterns of bimetallic nanoparticles can be categorised into four distinct groups as described by Ferrando, Jellinek & Johnston (2008). The first being the ‘core-shell’ structure, where atoms of element A form a shell around atoms of element B. The second is ‘phase-separated’ bimetallic structure which forms subclusters of elements A and B while sharing a mixed interface. The third is the ‘mixed structure’ where atoms of element A and B are randomly arranged within the bimetallic structure. Then finally, the ‘multi-shell’ bimetallic structures have alternating shells of elements A and B.

2.8 Geometric and electronic effects of bimetallic catalysts

Bimetallic catalysts are shown to alter the binding energy of some monometallic catalysts, hence making them favourable for CO_2RR. In investigating the Ag-Co complex as a potential catalyst, Singh et al. (2017) argue that electron-rich Co donates electrons to Ag, and hence change the binding strength of the electrocatalyst towards reaction intermediates. Through XRD analysis, Singh et al. (2017) show that the AgCo form a heterostructure, which allows for significant electron sharing.

Control experiments by Singh et al. (2017) indicated that monometallic Ag and Co catalyst produce a predominantly CO stream. However, as shown in Table 2-2, the Ag-Co bimetallic catalyst increases the selectivity towards methane and ethylene formation over various potentials. This difference is due to the increased binding energy of the CO intermediate in the bimetallic alloy, relative to the individual elements, thus allowing for further reduction of CO (Singh et al., 2017).

Table 2-2: Product selectivity (%) over Ag-Co electrocatalyst, from Singh et al. (2017).

Applied voltage (V vs RHE)	**CH_4**	**CO**	**C_2H_4**
-1.5	13.5	86.4	0
-1.8	38.3	61.6	0
-2.0	37.6	60.2	2.0
-2.3	68.7	31.2	0
-2.5	16.6	83.4	0
-3.0	18.6	81.3	0

Ma et al. (2017) investigated CuPd bimetallic nanoparticles for the CO_2RR. The study was performed for bimetallic structures with different mixing patterns, ranging from ordered, disordered, and phase-separated atomic arrangements as shown in Figure 2-7 for a fixed Cu to Pd atomic ratio of 1:1. Other disordered bimetallic structures with Cu to Pd atomic ratios of 1:3, and 1:4 were also investigated. Figure 2-8 shows the product FEs from CuPd (1:1) with various mixing patterns. XPS revealed that Cu had a different valency states in each structure, which correlates with findings by Singh et al. (2017), indicating that the CuPd bimetallic structures have different electronic states relative to their monometallic electronic states.

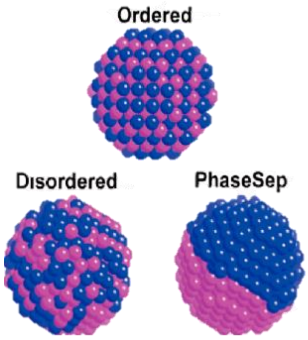

Figure 2-7: Various atomic arrangements of the CuPd electrocatalysts (Ma et al., 2017).

Figure 2-8 illustrates that all CuPd (1:1) mixing patterns exhibit a CO FE of above 10% over the applied potential range. However, from all mixing patterns, the phase-separated CuPd (1:1) has the highest selectivity for C_2 products (ethanol and ethylene) while the ordered and disordered structures preferentially produce methane over the applied potential range. Section 2.3.2 has highlighted the importance of CO intermediate in the formation of C_{2+} products. The preferential production of C_2 products from the phase-separated structure may be due to favourable molecular distance between the Cu and Pd islands, which limits steric hindrance between adsorbed CO, culminating in the ease of CO dimerization, which is a precursor to C_2 products formation (Ma et al., 2017). Pd has a high oxygen affinity (Peterson & Nørskov, 2012) and would thus serve two functions in disordered and ordered structures. The first would be to stabilise the *CHO intermediate – a methane precursor – by forming a bond with oxygen. The second would be cleaving of the oxygen bond as the *CHO intermediate is further protonated, thus weakening the C-O bond.

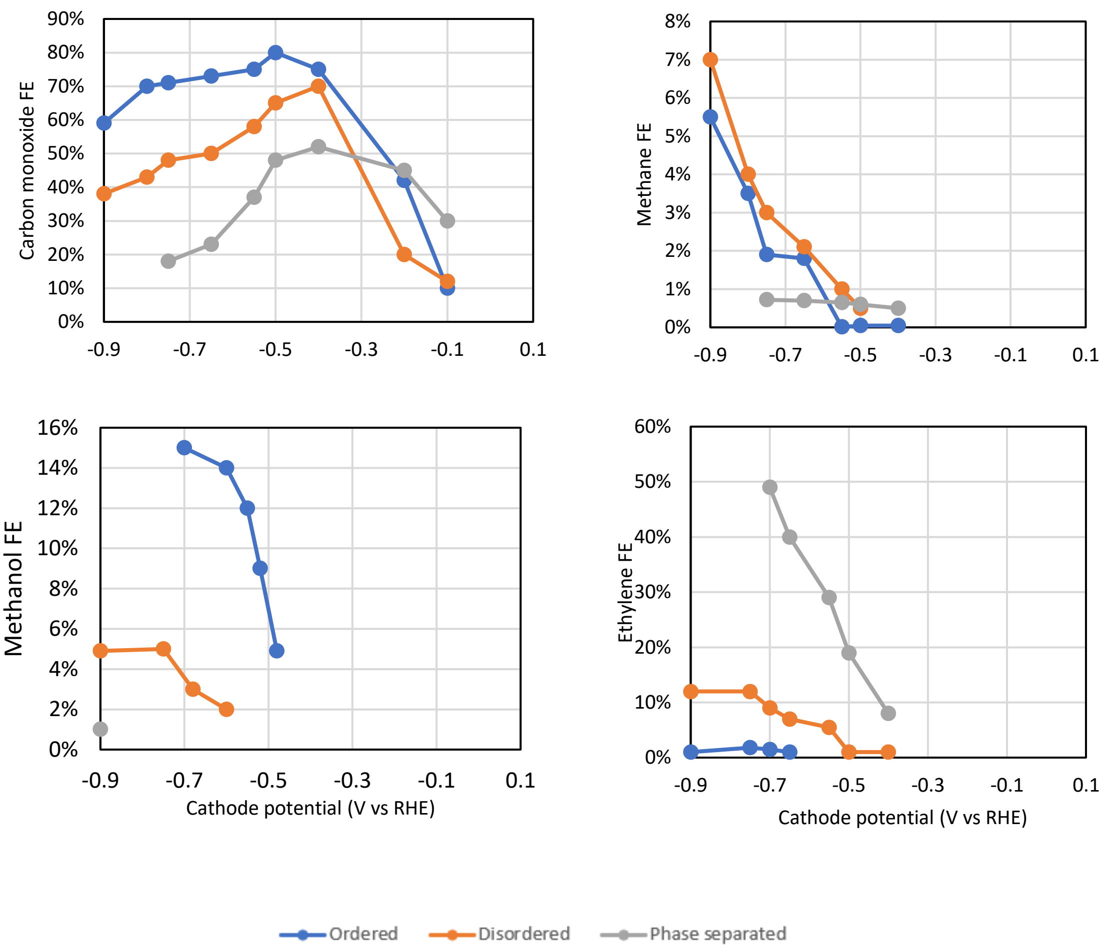

Figure 2-8: Product FE efficiency over applied potential range for CuPd (1:1) with ordered, disordered, and phase separated mixing patterns. Replotted from Ma et al. (2017).

2.9 Strategies in limiting the Hydrogen Evolution Reaction (HER)

The formation of hydrogen follows a simple reaction pathway and could occur via the Tafel-Volmer and/or the Tafel-Heyrovsky pathways shown in the following equations (Zheng et al., 2016).

Tafel

$2H_{ad} \leftrightarrow H_2 + 2^*$ (2-4)

Tafel-Heyrovsky

In acidic environment,

$H_{ad} + H^+ + e^- \leftrightarrow H_2 + {}^*$ (2-5)

In basic environment,

$H_{ad} + H_2O + e^- \leftrightarrow H_2 + OH^- + {}^*$ (2-6)

Tafel-Volmer

In acidic environment,

$H^+ + e^- \leftrightarrow H_{ad}$ (2-7)

In a basic environment,

$H_2O + e^- + {}^* \leftrightarrow H_{ad} + OH^-$ (2-8)

From the reactions above, it can be observed that the formation of hydrogen follows a two-step process, the adsorption of H^+ on the catalyst surface, and later hydrogenation to H_2 or the reaction between two H_{ad} species to form H_2. The low activation barrier of this reaction makes it difficult to inhibit. For CO_2RR, various strategies have been employed to limit the HER.

A study by Feaster et al. (2017) explored the use of an ionic electrolyte, 1-ethyl-3-methylimidazolium chloride ([EMIM]Cl), to suppress the formation of H_2 in basic and acidic conditions. Here, catalytic experiments using Fe, Ag, and Cu were performed without the introduction of CO_2. The electrolyte was prepared using 0.1M KOH, and 0.05M H_2SO_4, with a final 0.1M concentration of [EMIM]Cl was ensured. The three metals were chosen based on their different product distributions under CO2R conditions. From this work, it was observed that under acidic conditions H_2 was suppressed by up to 75% on Fe, 30% on Cu, and 10% on Ag catalysts, whilst under basic conditions, no significant suppression of H_2 was observed. Feaster et al. (2017) postulated that under acidic conditions, the cation, [EMIM]+ adsorbs onto the catalyst surface which leads to the repulsion of H^+ ions. Even though this work has shown that H_2 can be suppressed with the addition of [EMIM]Cl, it does not show the effect this has on the product distribution. In addition to this, [EMIM]Cl blocked catalytic sites, which culminated in the lowering of the overall activity of the three evaluated catalysts. Additionally, NMR data indicated that it decomposed under electrochemical conditions.

2.10 Nanoparticle nucleation and growth

Nucleation is the first step towards nanoparticle formation. Nuclei act as seeds and are the templates for crystal growth. Nuclei formation typically involves the decomposition of a metal precursor or its reduction to a zero valent atom. Homogenous nucleation occurs when nuclei form uniformly through the solvent, and this most likely culminates in a narrow particle size distribution (Polte, 2015). On the other hand, heterogeneous nucleation occurs when nuclei form in structural inhomogeneities, such as the walls of containers and grain boundaries (Polte, 2015).

Nucleation and growth of nanoparticles typically follows the LaMer mechanism (LaMer & Dinegar, 1950), shown in Figure 2-9. Nanoparticle formation through the LaMer mechanism can be divided into three distinct phases. Phase I involves the formation of an atomic monomer through the reduction of precursor or its decomposition. As the concentration of the monomer increases, the system goes through Phase II where the monomer undergoes 'burst nucleation' where clusters of particles begin to form. In Phase III, the concentration of the monomers begins to decrease as monomers diffuse to clusters to form nanoparticles. During the growth period nanoparticles may undergo Ostwald ripening. This is the transfer of smaller nanoparticles to larger nanoparticles, due to the instability of smaller nanoparticles (Gommes, 2019).

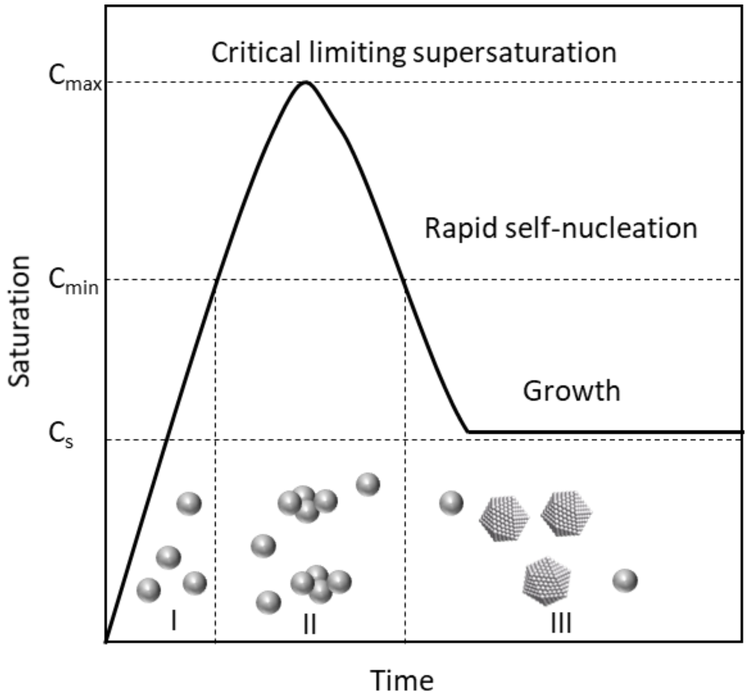

Figure 2-9: Illustration of the LaMer mechanism model. Redrawn from Polte (2015).

2.11 Cu and Ag nanoparticles synthesis routes

There are multiple routes for the synthesis of nanoparticles. The synthesis methods explored in this section are electrodeposition, microemulsion, chemical reduction, laser irradiation and thermal decomposition. Most of these methods take measures to prevent the oxidation of copper to CuO or Cu_2O when exposed to air (Hung, Ling-I et al., 2010).

2.11.1 Chemical reduction

This route is the most widely employed process for the synthesis of silver nanoparticles (Quang Huy, Van Quy & Anh-Tuan, 2013). This chemical reduction process can be achieved in an aqueous or organic solution. It requires the use of a metal salt precursor, and reducing agent(Quang Huy, Van Quy & Anh-Tuan, 2013). A surfactant can be added to the synthesis vessel to control the nanoparticle size.

In the synthesis of Cu nanoparticles, ascorbic acid has been widely used as a reducing agent, because of its ability to scavenge oxygen molecules, and thus prevent the oxidation of copper during preparation and storage (Yu et al., 2009). Even though this is the case, Ali et al. (2018) report that the nanoparticles employed in this method were still susceptible to oxidation to Cu_2O. Other reducing agents such as hydrazine, sodium borohydride, and polyol can be employed.

This method has been associated with a wide particle size distribution. Yu et al. (2009) showed that this can be combatted by making use of polyvinyl pyrrolidone (PVP) as a capping agent. It was shown that increasing PVP concentrations correlate to a reduction in the mean particle size. The mechanism of the size control by PVP is through PVP binding onto the surface of the Cu nuclei, which induces steric repulsion to prevent particle agglomeration (Thi My Dung et al., 2011). Thi My Dung et al. (2011) showed that a copper mean particle size of 6 nm with a narrow variance can be achieved through the chemical reduction process.

The production of silver nanoparticles of a specific shape and size is highly sensitive to experimental conditions and procedures (Quang Huy, Van Quy & Anh-Tuan, 2013). For example, Dongjo, Sunho & Jooho (2006) have shown that by injecting a silver nitrate solution at 100 ˚C at a rate of 2.5 $ml.s^{-1}$ in an ethylene glycol and PVP solution, spherical particles with a diameter of 17 (±2) nm can be synthesised. This is in comparison with heating a solution containing the silver nitrate salt, PVP, and ethylene glycol without injection to the same temperature, which yields a particle size of 27 (±10) nm. The injection of the hot solution introduces rapid nucleation thus a narrow particle size distribution can be achieved (Dongjo, Sunho & Jooho, 2006).

2.11.2 Laser irradiation

This synthesis method involves the preparation of nanoparticles from a metal precursor and surfactant in an aqueous solution, without the addition of a reducing agent (Abid et al., 2002). A pulse laser of a known wavelength is irradiated on the prepared solution containing the precursor and surfactant, which triggers the photolysis of water to form radicals (Belloni et al., 1998). The formed $H\cdot$ radical, and solvated electrons (e_{aq}^{-}) act in the place of the reducing agent, thus reducing the metal ion (M^{+}) to its zero oxidation state (M^{0}) (Abid et al., 2002). These reducing routes are shown below.

$$M^{+} + e_{aq}^{-} \rightarrow Ag^{0}$$

$$M^{+} + H \cdot \rightarrow Ag^{0}$$

For silver nanoparticles synthesis employing this route, Abid et al. (2002) report a large average particle diameter of 13.3 nm and a narrow standard deviation of 2.6 nm. However, they report a low silver nanoparticle yield in the range 10 to 20%. Belloni et al. (1998) attributes this low yield for this synthesis route due to the formation of an $OH\cdot$ radical during the photolysis of water. This is capable of oxidising Ag^{0} to Ag^{+}. To circumvent this, Belloni et al. (1998) propose that this synthesis route should include the addition of a chemical capable of scavenging $OH\cdot$ radicals.

2.11.3 Thermal decomposition

The synthesis of copper nanoparticles via this process has been achieved by Hung, Ling-I et al. (2010). This synthesis process involves two steps: surface oxidation and vacancy coalescence. Since copper nanoparticles are susceptible to oxidation in air, this process is based on creating a surface oxide layer (passivation), which will prevent further oxidation of these nanoparticles (Hung, Ling-I et al., 2010). In this process, Hung, Ling-I et al. (2010) thermally decomposed copper(I) acetate in trioctylamine in tetradecylphosphonic acid (TDPA). This was followed by precipitation using ethanol, which was followed by dispersion using hexane or chloroform. The copper nanoparticle size could be controlled by altering the ratio of the copper precursor and TDPA, where the smallest particle sizes of 8.4(±0.8) nm were achieved at a copper precursor to TDPA ratio of 2:1. By decreasing the copper precursor to TDPA ratio to 1:1, an average particle size of 14.7 nm was achieved. Manthiram, Beberwyck & Alivisatos (2014) used this method to synthesise Cu nanoparticles, which were evaluated in CO_2RR conditions. Higher rates of methanation on these copper nanoparticles of up to four times were achieved, relative to a copper foil. The ratio of organic solvent and reducing agent to copper nanoparticles yield is unclear in this process.

2.11.4 Microemulsion

The microemulsion synthesis process involves the use of three phases, oil, water and surfactants. The surfactants form an interface between the oil and water as they exist in both phases (Parveen et al., 2016). The particle growth is reported to occur in the microemulsions in the oil phase, and this limits the oxidation of copper nanoparticles (Parveen et al., 2016). Various factors have been recognised to affect the size distribution of the particles, such as surfactant type, the concentration of the precursor salt, as well as the water to oil ratio (Parveen et al., 2016).

This method reports narrower particle size distribution relative to chemical reduction, however, a low nanoparticle yield has been reported (Ali et al., 2018).

2.11.5 Electrodeposition

Electrodeposition is the induction of a potential difference between two electrodes in an electrochemical cell, which drives the reduction and thus coating of metals on the cathode electrode surface. In this context, this requires preparation of a solution containing a copper salt.

Through the electrodeposition process, employing a copper nitrate solution, Bandyopadhyay & Chakravorty (2011) synthesised nanoparticles in the size range of 3.1 to 11.4 nm. This indicates the difficulty of controlling the size distribution Cu in this method. Additionally, the occurrence of this process in an aqueous system increases the susceptibility of Cu to oxidation.

2.12 Electrochemical cells for CO_2RR nanoparticle evaluation

2.12.1 Flow cell with gas diffusion electrode

The flow cell consists of three electrodes: a gas diffusion electrode where the CO_2 reduction occurs, a reference electrode, and a counter electrode. This is shown in Figure 2-10. The gasdiffusion electrode consists of an assembly of supported nanoparticles, Nafion®, carbon cloth, and a silver gauze, shown in Figure 2-11. The Nafion® serves as a catalyst binder to the gas diffusion electrode and aids in proton transfer to the catalyst site, whilst the silver gauze acts as an electron conductor. Another feature of the electrolytic cell is that it has a Nafion® membrane, separating the cathode and anode side of the cell. This membrane only allows for the passage of protons, and thus preventing the transfer of CO_2 reduction products to the anode where they could possibly be oxidised (Kuhl et al., 2012).

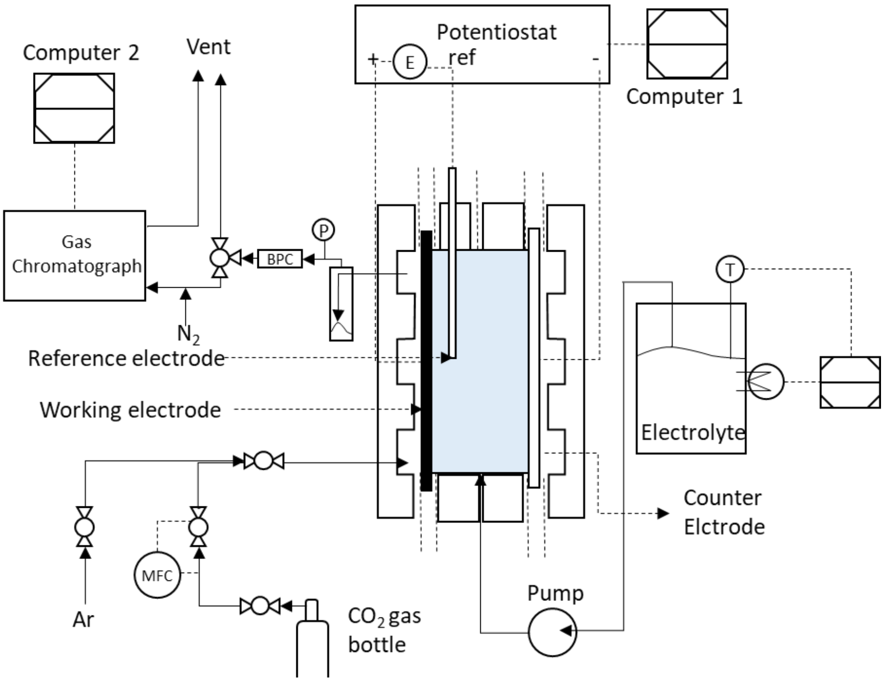

Figure 2-10: Electrolytic cell with gas diffusion electrode. Adapted from Jeanty et al. (2018).

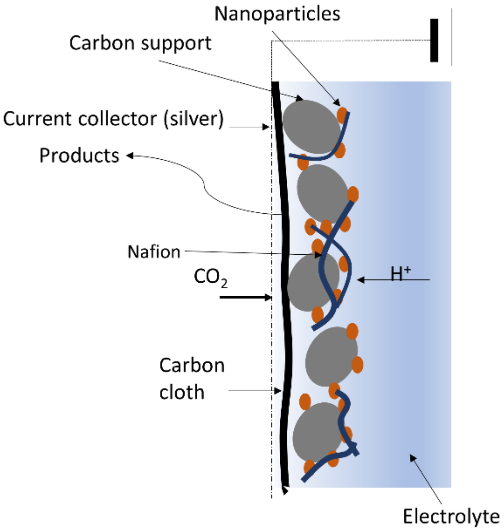

Figure 2-11: Expansion of the gas-diffusion electrode.

The CO_2 is introduced through the gas diffusion electrode, where it is reduced by the catalyst to various products. The advantage of this cell design is the exposure of the reactant gas to high surface area gas diffusion electrode. For this type of design, the liquid electrolyte is continuously pumped out and replenished, to limit the accumulation of products. Based on this design, both liquid and gas products formed during CO_2 reduction can be identified and quantified. The gas product analysis involves the use of gas chromatography, which is coupled with a Flame Ionisation Detector (FID) and

Thermal Conductivity Detector (TCD). To analyse liquid products, High Performance Liquid Chromatography (HPLC) and/or NMR can be employed.

The challenge with this electrolytic cell design at the lab-scale is the difficulty in the assembly of all cell components, to ensure that no leakage occurs. In addition to this, the electrolyte volume must be optimised to be low to allow for the identification of liquid products formed during reduction. Other variations of this cell design exist, which do not include the Nafion® membrane, and no replenishment of the electrolyte (Lu et al., 2016).

2.12.2 Batch cell with a gas-diffusion electrode

The batch cell with a gas-diffusion electrode is an adaptation of the electrolytic cell design shown in Figure 2-10. The glass cell-design shown in Figure 2-12 is based on work from Geschiere (2014) which made use of a 1 L cell. This cell design makes use of three electrodes, a gas diffusion electrode as the cathode, a reference electrode, and a counter electrode.

The gas diffusion electrode has a glass tube which transports CO_2 gas to the electrode chamber. This chamber consists of a perforated metal conductor (usually silver gauze is used), and a gas porous carbon cloth which has the supported catalyst and Nafion® deposited on it. The metal conductor is connected to the potentiostat via a metal wire. The carbon cloth for this cell is designed to be porous and hydrophobic to allow for unhindered gas flow to the catalyst site and to prevent water seepage into the electrode compartment. The carbon cloth has a Teflon layer, which ensures that it is hydrophobic, thus preventing electrolyte from being in contact with the conducting wire.

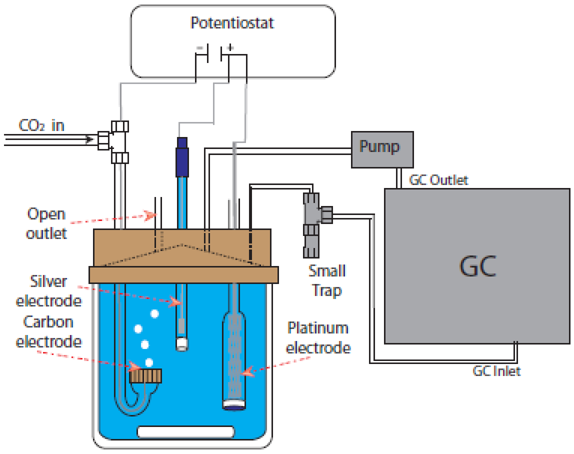

Figure 2-12: Illustration of a 1L batch electrochemical cell with a gas-diffusion electrode, adapted from Geschiere (2014).

Similar to the electrolytic cell, both gas and liquid products formed during CO_2 reduction can be identified and quantified with this electrochemical cell design. However, the batch cell, as designed by Geschiere (2014), does not have a proton membrane, separating the cathode and anode. This increases the possibility of CO_2 products oxidation on the anode. On a lab-scale basis, the batch cell tends to be easier to assembly and construct, relative to the flow cell.

2.12.3 Electrochemical cell with rotating ring disc electrode (RRDE)

Similar to the electrolytic and batch cell with GDE, this cell design uses three electrodes, namely, the working electrode, a reference electrode, and counter electrode. The RRDE is used as the working electrode. This cell design is illustrated in Figure 2-13. The RRDE consists of a glassy carbon disc located in the middle – where the catalyst can be deposited – and a Pt ring as shown in Figure 2-13. The disc and ring are both separated by PTFE.

The disc and ring of the RRDE can be operated at different potentials in the same experiment. Additionally, the RRDE can be rotated at a specified speed through a connected shaft, which controls the mass transfer to the disc. Thus, in the context of CO_2 electrochemical reduction, the reaction products formed on the disc are transferred by convection to the ring where they are detected through the application of an oxidative ring potential (Zhu et al., 2018).

For the electrochemical reduction of carbon dioxide, two types of experiments have been performed using a RRDE: (i) scanning the disc potential and holding the ring at an oxidative potential, allowing for product detection, (ii) holding the disc at a fixed potential, and scanning the ring potential, which aids in identifying at which potential a certain product is formed (Zhu et al., 2018).

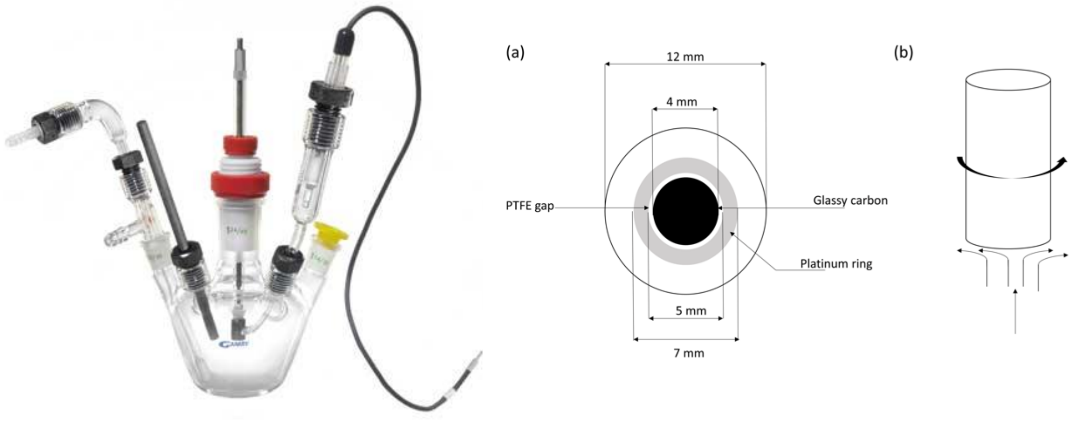

Figure 2-13: Three cell electrode with an expansion of the RRDE, adapted from Zhu et al. (2018).

2.13 Electrochemical cell standard conditions

In addition to the factors described in the preceding sections, various other factors can affect the CO_2RR. These include operating temperature, type of electrolyte, the concentration of electrolyte and pH. There are no reported standard conditions for the electrochemical reduction of carbon dioxide.

Ahn, Abu-Baker & Palmore (2017) investigated the effect of electrolyte temperature on product selectivity on copper electrodes. In experiments ranging from a temperature of 2 to 42˚C, it was found that at low temperatures, the formation of methane (CH_4) and carbon monoxide (CO) is favoured rather than the formation of ethylene (C_2H_4) and HCOO. Ahn, Abu-Baker & Palmore (2017) attribute this observation to the rise in carbon dioxide concentration, [CO_2], at lowered temperatures, which leads to acidic conditions, thus favouring CH_4 formation. Additionally, Ahn, Abu-Baker & Palmore (2017) have shown that the HER is favoured at elevated temperatures, with hydrogen formation increasing by 400% between 2 ˚C and 42˚C.

The purpose of the electrolyte is to reduce solution resistance and to act as a buffer to reduce the change in pH (Varela et al., 2016). In work on polycrystalline copper, Schouten et al. (2011) showed experimentally that the formation of methane (CH_4) is favoured under acidic conditions, and the formation of ethylene is favoured in alkaline conditions. The pH near the electrode surface has been reported to be higher than the bulk pH due to the consumption of H^+ ions at the electrode (Varela et al., 2016). This highlights the importance of the ability of an electrolyte to act as a buffer. In investigating different concentrations of $KHCO_3$ (0.005 M, 0.1 M and 0.2 M), Varela et al. (2016) show that hydrogen and methane formation is inhibited at low electrolyte concentrations (0.005M), whilst the production of carbon monoxide and ethylene are not affected. This is attributed to the high local pH and thus limiting the amount of H^+ ions present near the electrode surface.

3 Chapter 3 – Objectives and key questions

Cu is currently the most promising catalyst for the electrochemical reduction of carbon dioxide, but it still suffers from the undesired hydrogen evolution reaction (HER) and being unselective to a specific hydrocarbon or oxygenate product. From the literature survey, it has been shown that there exists a competition between CO formation and the HER. On the other hand, Ag has been shown to preferentially produce CO under normal carbon dioxide electrochemical reduction conditions.

This study will investigate the use of CuAg nanoparticles as a potential catalyst for the CO_2RR, evaluating the impact of catalyst composition and atomic arrangement on CO_2RR product distribution and activity relative to monometallic catalysts. In addition to this, there exists a gap for a synthesis route for CuAg nanoparticles with limited agglomeration.

3.1 Research objectives

The following are the research objectives of this work:

- To synthesise different atomic ratios of CuAg bimetallic nanoparticles supported on carbon.
- To investigate the effect of low-temperature conditions, precursor concentration, and surfactant on the morphology of CuAg bimetallic nanoparticles.
- To commission and evaluate the performance of an electrochemical reactor with a gas-diffusion electrode, which will allow for the analysis of gas and liquid products.
- To evaluate the electrocatalytic performance of CuAg nanoparticles in the electrochemical reduction of carbon dioxide.
- To understand the effect of the CuAg bimetallic ratio and atomic arrangement on the observed activity and product distribution.

3.2 Key Questions

The following are the proposed key questions of the investigation:

- How does the morphology of CuAg nanoparticles change over the synthesis period?
- What is the effect of synthesis temperature on the nanoparticle morphology?
- What is the effect of precursor concentration on the nanoparticle morphology?
- What is the influence of the presence of surfactant on the morphology, and composition of CuAg bimetallic nanoparticles?

- What is the electrochemical activity and product distribution in CO_2RR for nanoparticles synthesised with surfactant?
- What effect does CuAg bimetallic ratio have on the CO_2RR product distribution?

4 Chapter 4 – Methodology

Sections 4.1 to 4.4 of this chapter discuss the synthesis routes and physical characterisation undertaken for carbon-supported silver, copper, and various ratios of copper-silver bimetallic catalysts. Sections 4.5 to 4.6 discuss the design of the two electrochemical evaluation setups used in this work, and their associated product analysis methods. The first of these setups is a batch cell with a gas diffusion electrode, and the second is a three-electrode cell with an RRDE.

It should be noted that this section covers the final methodology employed for both the synthesis of nanoparticles and batch electrochemical cell. For a discussion on the development of the synthesis methods, as well as the development of the batch electrochemical setup design, refer to sections 5.1 and 5.3, respectively.

4.1 CuAg nanoparticles synthesis

CuAg bimetallic nanoparticles were synthesised via a chemical reduction route, using two methods named Method A, and Method B. The notation 'CuAg (x:y)' is used to refer to synthesised CuAg nanoparticles, where x and y refer to the $Cu(NO_3)_2.3H_2O$ and $AgNO_3$ relative molar ratio added to the synthesis vessel, respectively.

4.1.1 Method A

CuAg bimetallic nanoparticles were prepared via co-reduction of the two metal nitrate salt precursors, namely, silver nitrate ($AgNO_3$, 99.0%, Sigma Aldrich) and copper nitrate trihydrate ($Cu(NO_3)_2.3H_2O$, 98.0%, Sigma Aldrich) under inert and ice-cold conditions. The varying ratios of CuAg that were synthesised were as follows: CuAg(20:80), CuAg(50:50) and CuAg (80:20). In this synthesis, sodium borohydride ($NaBH_4$, Sigma-Aldrich) was employed as the reducing agent, and ethanol as the solvent (EtOH, 99.99%, Sigma-Aldrich).

A 250 ml three-neck flask was used as the synthesis vessel. This was covered in foil to prevent the photochemical reduction of $AgNO_3$, and it was also submerged in ice. For all the Cu to Ag bimetallic ratios, it was ensured that the total metal concentration was fixed at 4.5 mM. Since there is a wide difference between the Ag^+/Ag reduction potential (0.80 V), and the Cu^{2+}/Cu reduction potential (0.34 V), $NaBH_4$ was introduced in excess by ensuring a total concentration of 75 mM, to prevent the preferential reduction of Ag over Cu.

The proposed mechanism for the co-reduction is as follows:

Ionic dissociation

$NaBH_4 \rightarrow Na^+ + BH_4^-$ 4-1

$AgNO_3 \rightarrow Ag^+ + NO_3^-$ 4-2

$Cu(NO_3)_2.3H_2O \rightarrow Cu^{2+} + 2NO_3^- + 3H_2O$ 4-3

Reduction

$2Ag^+ + 2BH_4^- \rightarrow Ag^0 + 2H_2 + B_2H_6$ 4-4

$Cu^{2+} + 2BH_4^- \rightarrow Cu^0 + 2H_2 + B_2H_6$ 4-5

To prepare the reducing agent solution, 567 mg of $NaBH_4$ was mixed with 80 mL of ethanol. This was stirred for 5 minutes to ensure complete dissolution of $NaBH_4$. This solution was then transferred into a burette, which was placed above the synthesis vessel submerged in ice. Subsequently, the specific amounts of $Cu(NO_3)_2.3H_2O$ and $AgNO_3$ for the desired Cu to Ag bimetallic ratio were added to the reaction vessel together with 120 ml of ethanol. The contents of the synthesis vessel were vigorously stirred for 10 min at 1400 rpm, whilst bubbling argon. The purpose of this step was to deaerate the synthesis vessel as Cu nanoparticles are susceptible to oxidation, and this was to also allow for the dissolution of the metal precursors. Following this, the $NaBH_4$ ethanol solution was introduced to the reaction vessel dropwise over a 15 min period via the slight opening of the burette, whilst continuing to bubble argon. The total reaction time was 1 h, started at the release of the first drop of sodium borohydride. Argon was bubbled throughout the synthesis, whilst the contents of the vessel were continuously stirred at 1400 rpm in ice-cold conditions. After an hour, a sample for Transmission Electron Microscopy (TEM) was taken with a Pasteur pipette, to evaluate the immediate morphology after the synthesis period (see section 4.4.1 on how a TEM sample was prepared).

4.1.2 Method B

To understand the effect of the surfactant on the synthesis of the nanoparticles, this method followed the same procedure as Method A, except that hexadecylamine (HDA, 90% technical grade, Sigma-Aldrich) surfactant was added during synthesis. The surfactant, HDA, was added ensuring a total metal precursor to surfactant molar ratio of 1:2.5.

The monometals CuAg(0:100) and CuAg(100:0), and bimetallic nanoparticles: CuAg(20:80), CuAg(50:50), and CuAg(80:20) were synthesised via this method.

4.2 Investigation of washing procedure

For the prepared nanoparticles, it was vital that precursor and reducing agent ligands, as well as the surfactant, were removed, as these could impact the catalytic performance of the final catalyst. For the Cu-Ag system, the effect of the washing procedure on the prepared nanoparticle morphology and size was investigated. This is because of the reported sensitivity of Cu nanoparticles to oxidation. To perform this analysis, CuAg(50:50) prepared via Method A was used as a model for this investigation, as nearly equal amounts of both Cu and Ag are introduced to the synthesis vessel, and nanoparticles are without possible surfactant protection from oxidation.

During synthesis, TEM samples were taken at fixed time intervals: 15 minutes (or after the addition of the last drop of $NaBH_4$ solution), 45 minutes, and 1h (after synthesis). It was ensured that the sample was taken at the bottom of the synthesise vessel to ensure a representative sample. Following the hour-long synthesis, the contents of the vessel retained a black precipitate.

The as-prepared nanoparticles were left to settle for 15 minutes. Following this, the ethanol supernatant decanted, only leaving a thin film above the particles. A TEM sample was then taken of these nanoparticles. To investigate the effect of the washing procedure, the as-prepared nanoparticles were split into equal volumes of **Sample A**, **Sample B**, **Sample C**, and **Sample D**.

Sample A

The following washing procedure was followed for Sample A:

1. 50 mL of deionised water was added to the precipitate. This was stirred at 1000 rpm for 5 minutes.
2. The liquid was then decanted and discarded.
3. Steps 1 to 2 were repeated separately with 50 ml of ethanol, then 50 ml of acetone.
4. A TEM sample after washing with acetone was then taken.

Sample B, **Sample C** and **Sample D**

Sample B, Sample C and Sample D made use of acetone, ethanol and water, respectively. About 50 ml of the solvent of interest was added to the as-prepared nanoparticles, and this was stirred at 1000 rpm for 5 minutes. The liquid layer was then decanted and discarded, which was followed by a TEM sample of the nanoparticles being taken.

4.3 Deposition of nanoparticles onto carbon support

The deposition of the prepared nanoparticles onto a substrate offers the advantage of increasing the distribution of the prepared nanoparticles and limiting agglomeration during electrochemical evaluation (Sharma & Pollet, 2012). Additionally, it lessens the extent of nanoparticle sintering during electrocatalytic evaluation, whilst providing an electron pathway during electrocatalytic testing.

The as-prepared nanoparticles were deposited onto the carbon support (Vulcan XC-72R) via a colloidal deposition method. The target metal loading was 30wt%, therefore for all the prepared nanoparticles, 265 mg of carbon support was used.

The carbon support was first crushed with a mortar and pestle. Then 60 ml of ethanol was added to the support, and this colloid was sonicated for 30 minutes to ensure the dispersal of the support. The as-prepared nanoparticles in 20 ml of ethanol were then added dropwise to the support colloid via a Pasteur pipette, and this new colloid was further sonicated for 30 mins.

Following this, ethanol and any trace water were removed by employing a rotary evaporator. This step involved the colloid being continuously rotated whilst being submerged in a 60˚C water bath. The vacuum was set at 175 mbar for 45 mins to remove ethanol. Then the vacuum was set to 72 mbar for 15 mins to allow for the removal of any water that may have been present.

The dried and supported catalyst was then stored in a glass vial.

4.4 Physical Characterisation

4.4.1 Transmission Electron Microscopy (TEM)

At various points of the catalyst synthesis, TEM samples were prepared. The model procedure involved making use of copper grids which have an electron transparent carbon film coating.

Dry samples were slightly crushed using a pestle and mortar, then a small amount of the sample (~5 mg) was transferred to a micro-vial. To this, a small volume of ethanol (~2 ml) was added, after which the resulting colloid was sonicated for 30 seconds. A small volume of this colloid was then extracted using a Pasteur pipette, and one or two drops were placed on the copper grid, and this was then dried in ambient air for 15 minutes. For colloidal samples, the same process was followed, without the crushing step.

The samples were analysed on a Tecnai F20 transmission electron microscope was operated at 200 kV. The source of the high energy electrons was a zirconia-coated tungsten crystal heated at 2100°C. The nanoparticle size distribution was then determined with- Image J, where at least 500 particles were considered for the particle size distribution.

High Angle Annular Dark Field (HAADF) imaging, elemental mapping, and Electron Dispersive Spectroscopy (EDS) was performed on the supported nanoparticles which were prepared on Nickel quantifoil grids. For this analysis, a Scanning Transmission Electron Microscope Bright Field (STEM-BF) were recorded using a JEOL JEM-ARM200F double Cs-corrected TEM equipped with a Field Emission Gun (FEG), a STEM unit and an HAADF detector, operated at 200 kV. The purpose of this analysis was to determine the extent of Cu and Ag elemental mixing on nanoparticles for the different bimetallic ratios prepared.

4.4.2 Powder X-ray Diffraction (PXRD)

Powder X-ray Diffraction (PXRD) was performed on supported catalysts to determine the crystalline phases present, and crystallite size. These analyses were performed on a Bruker AXS D8 Advance, which made use of a Co X-ray source (λ=1.79026 Å) and operated at 35 kV and 40 mA. The analysis was performed at a 2θ range from 20˚ to 120˚ for a period of 2 hours. The produced diffractograms were analysed against reference patterns in the ICDD PDF2 2006 database.

Scherrer's equation was used to determine the crystallite size of the nanoparticles. For this, the most pronounced diffraction line of the sample was used in the computation.

$$\tau = \frac{K\lambda}{\beta cos\theta} \qquad \text{4-6}$$

Where,

K is the sphericity of the particle, in this case, a value of K=1 was used

λ is the X-ray source wavelength, in this case, λ=1.79026 Å

β is the peak broadening at half of the diffraction line maximum

θ is Bragg's angle of the diffraction line.

4.4.3 Energy Dispersive X-ray spectroscopy (EDX)

Energy Dispersive X-ray spectroscopy (EDX) coupled to a Scanning Electron Microscope was used to determine the Cu to Ag atomic ratios of the supported CuAg nanoparticles. This analysis was carried out on an FEI Field Emission Nova NanoSEM 230.

4.4.4 Thermogravimetric Analysis (TGA)

Thermogravimetric Analysis (TGA) was employed to determine the metal loading of the supported nanoparticles. The basis for this analysis is that in an oxidative atmosphere, the supported catalyst would lose mass due to the oxidation of carbon at high temperatures. This analysis was performed on a TA SDT650 instrument.

To perform this analysis, the masses of two aluminium oxide crucibles were first tared against each other. About 2 to 5 mg of catalyst was placed on one of the aluminium oxide crucibles, whilst the other crucible (without sample) was used as the reference crucible throughout the analysis. The temperature was ramped at a rate of 5˚C/min, from 50 ˚C to 600 ˚C, whilst flowing synthetic air at a flowrate of 10 ml/min in the TGA chamber. Throughout this temperature range, the changes in mass and heat flow were tracked.

4.5 Electrocatalytic characterisation with gas diffusion electrode

4.5.1 Overview of electrochemical cell setup

The setup illustrated in Figure 4-1 was one of the setups designed for purposes of electrocatalytic evaluation of the synthesised catalysts. Only one gas was fed to the electrochemical cell at a time, with the flowrate into the cell being confirmed with a volumetric flow meter before every run.

The outlet of the electrochemical cell was sent to a cold trap to condense any entrained water which could adversely affect the GC upstream. The outlet of this cold trap was mixed with the GC reference gas, N_2, of which the volumetric flowrate of N_2 was confirmed for every run with a volumetric flowmeter. This mixed stream fed the online GC, which had a Thermal Conductivity Detector (TCD). At specified intervals, samples for offline GC with a Flame Ionization Detector (FID) were taken, through a glass ampoule for full characterisation of the product stream.

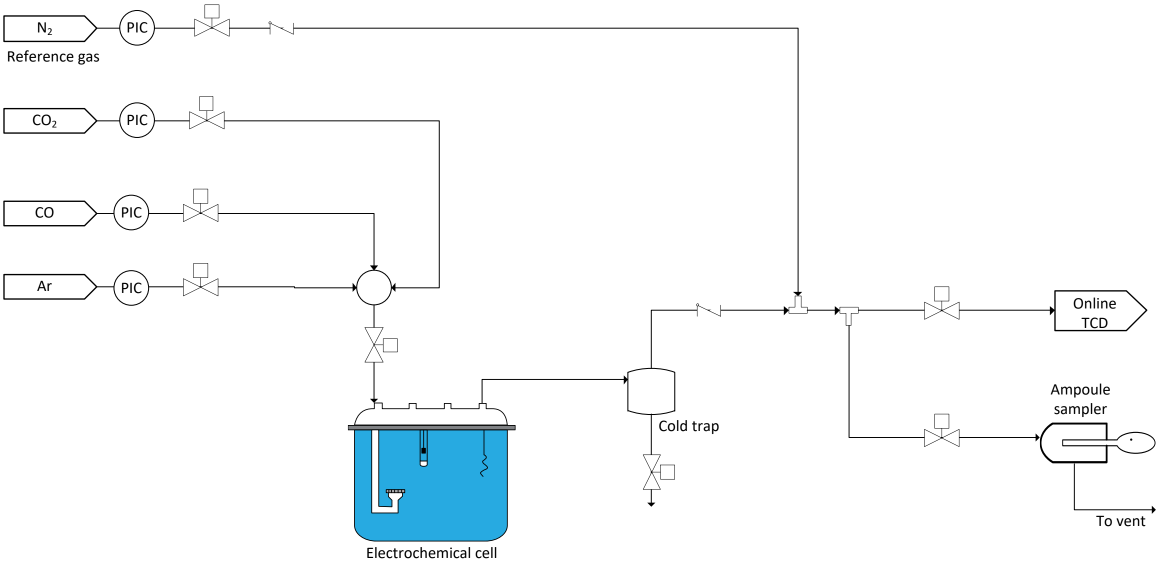

Figure 4-1: Electrocatalytic evaluation setup.

4.5.2 Electrochemical cell design

A four-port, one-litre electrochemical cell (GlassChem) was designed based on work from Geschiere (2014), as shown in Figure 4-2. The cell was designed to have a gas diffusion working electrode, which enables the direct contact of an introduced gas with electrolyte. The details of this working electrode are further expanded in Figure 4-3.

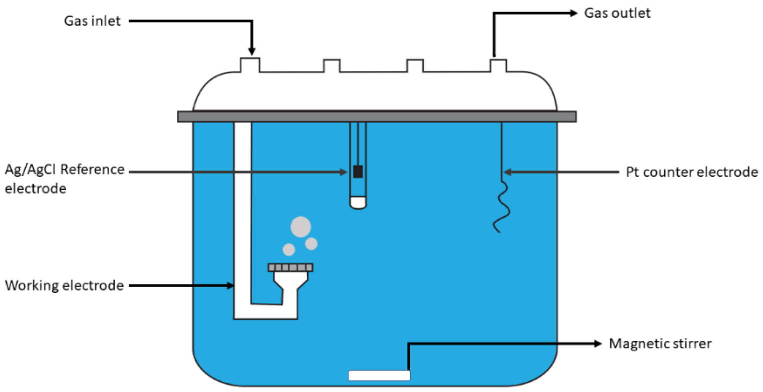

Figure 4-2: Electrochemical cell design adapted from work by Geschiere (2014).

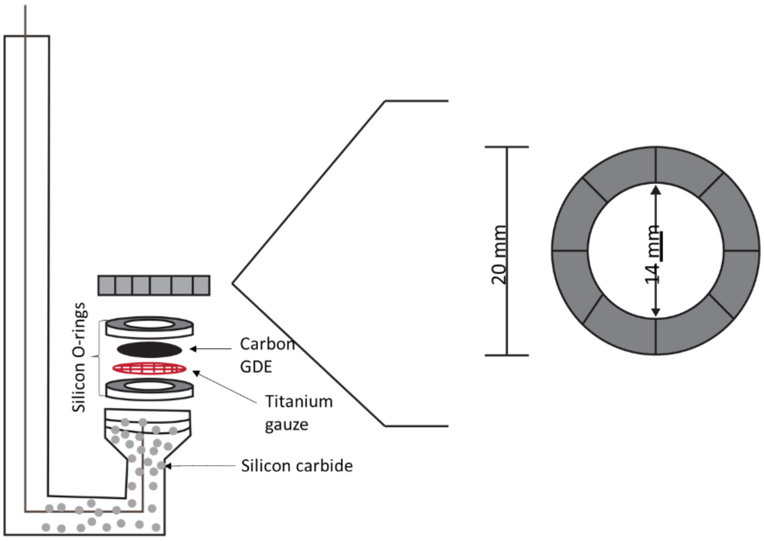

Figure 4-3: An expanded view of the cathode of the electrochemical cell.

The working electrode comprised of four key components: gas diffusion electrode (GDE), titanium gauze, silicon carbide, silicon O-rings. The purpose of the titanium gauze was to offer mechanical stability and allow for electron flow to the carbon GDE. Additionally, the titanium gauze and the silicon carbide ensured a uniform gas distribution on the GDE (as discussed in section 2.12.1). The silicon O-rings provided mechanical stability for the titanium gauze and GDE.

4.5.3 Catalyst ink preparation and spraying on GDE

The gas diffusion layer shown in Figure 4-3 was prepared to have an evenly distributed top catalyst layer. This was done by spraying a prepared ink of the supported nanoparticle catalysts onto a carbon cloth (Avcarb). The carbon cloth is both hydrophobic and permeable to gas, which allows for the simultaneous contact of catalyst layer, electrolyte, and gas, whilst preventing the seepage of electrolyte into the working electrode chamber. The air spray employed for this process is shown in Figure 4-4.

Figure 4-4: Prona ® Air spray RH-CP used to spray catalyst layer onto GDE.

The catalyst ink was prepared by dispersing 100 mg of the prepared catalyst in 200 ml of ethanol. The low catalyst to ethanol ratio was chosen to prevent clogging of the spray nozzle. Aqueous 5wt% Nafion® solution was then added to the catalyst-ethanol colloid, ensuring a 30wt% Nafion® fraction relative to the catalyst. This colloid was then sonicated for an hour to ensure homogenous mixing of the Nafion® and catalyst.

The spraying of the catalyst onto the carbon cloth was performed in a fume hood. The Prona ® Air spray was connected to a 1 bar argon line. Argon acted as the catalyst carrier gas during spray. A 4.5 cm x 4.5 cm carbon cloth was cut and weighed. This carbon cloth was then placed atop of a heating plate. A small volume of prepared ink was then poured onto the air-spray chamber, ensuring that it is ¾ full. This was to ensure an even distribution of catalyst throughout the GDE, the spraying pattern that was followed is shown in Figure 4-5.

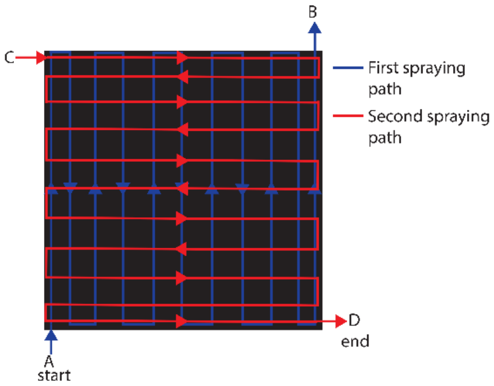

Figure 4-5: Catalyst ink spraying pattern on GDE.

First, the heating plate was set to 110 ˚C, which led to the evaporation of water and ethanol during spraying. Spraying onto the catalyst layer began by placing the air-spray approximately 10 cm away from the carbon cloth. A vertical path, A → B (blue), was followed at the commencement of spraying. Following this, spraying was stopped for 1 minute, to allow for the evaporation of solvents. A horizontal spraying path, C → D (red), was then followed. After drying, the process was started again from point A. During spraying, the mass of the GDE was measured, and this was compared to the mass of the carbon cloth prior to spraying. Spraying was stopped when a catalyst loading on the carbon cloth of 5 mg/cm^2 was achieved. This spraying procedure resulted in catalyst losses via entrainment of air in the fume hood, as well as due to spraying outside of the carbon cloth area, hence the total volume sprayed was almost twice the required amount.

4.5.4 Electrocatalytic evaluation procedure

The electrochemical evaluation was performed in a 1 litre, three-electrode, batch cell. A Ag/AgCl electrode was used as the reference electrode, and during each experiment, this was placed as close as possible to the working electrode. Pt wire was used as the counter electrode for the cell. For electrochemical evaluation, 0.1 M potassium phosphate buffer at a pH of 7 was used as the electrolyte, and was prepared from potassium biphosphate, and potassium monophosphate with 18 MΩ.cm deionised water. Throughout the electrocatalytic evaluation the electrolyte was stirred at 700 rpm.

To begin electrocatalytic evaluation, 750 ml of electrolyte was used in the electrochemical cell. The cell was first deaerated by bubbling argon for an hour, after which the cell was saturated with CO_2 for an hour. During this time, the online GC was run to ensure that only CO_2 peaks were present in the GC, indicating removal of other compounds from previous runs in the pipeline. Following this, the working electrode with GDE, as shown Figure 4-3, is submerged in the electrolyte. CO_2 at 1.0 bar, at a volumetric flowrate of 10 ml/min is then introduced through the working electrode.

At the beginning of electrocatalytic evaluation, potentiostatic electrochemical impedance spectroscopy (PEIS) is performed to determine solution resistance. This is taken at the potential of interest and in the frequency range 1 MHz to 1 Hz. To reduce any surface metal oxide present in the catalyst layer, 20 cycles of cyclic voltammetry (CV) at a scan rate of 50 mV/s, in the voltage range -0.4 to -1.1 V vs RHE are then performed. PEIS is again performed to account for the solution resistance. Then chronoamperometry (CA) is performed at the desired potential for 60 mins, at which at 10 mins intervals PEIS is performed to account for solution resistance. At the end of the CA, a CV is performed at similar conditions as the initial CV. During each experiment, a gas product sample is injected to the online GC equipped with a TCD and a manual sample taken for an offline GC equipped with FID at 10 mins intervals (see section 4.6.1).

4.6 Characterisation and quantification of products

4.6.1 Gas products

Sample preparation

The gaseous effluent of the electrochemical cell was characterised and quantified via online and offline gas chromatography (GC) instruments, which were equipped with a Thermal Conductivity Detector (TCD) and a Flame Ionization Detector (FID), respectively. The GC-TCD was used to detect and quantify the amount of CH_4, CO_2, CO, and H_2. For this GC, N_2 and Ar were used as reference and carrier gas, respectively.

The GC-FID was employed to detect and quantify the amount of hydrocarbons in the electrochemical cell effluent. To prepare the sample, a vacuum-sealed glass ampoule was inserted into the mouth of the ampoule sampler as shown in Figure 4-6. Following this, the needle valve was slightly opened to allow gas to flow into the ampoule chamber. The ampoule was then unsealed by breaking it using the needle, which led to the flow of gas into the ampoule. The ampoule is then removed from the sampler and sealed using a butane flame.

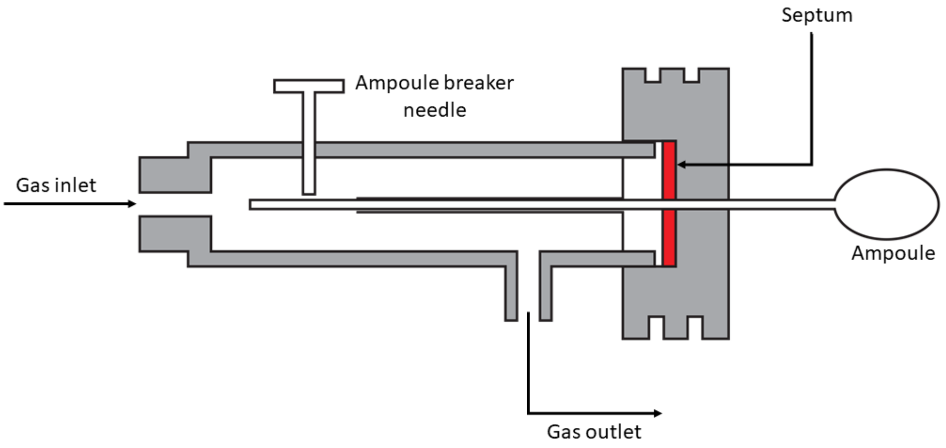

Figure 4-6: An illustration of the gas ampoule sampler.

Sample quantification

To determine the product flowrates, the GC-TCD was calibrated with a cylinder with known gas concentrations (CO=25%, CO_2=5%, CH_4=5%, H_2=45%, N_2=5%, Ar=15%). From this calibration, a response factor for each compound relative to that of N_2 could be determined. This related the area under the peak for a certain substance to the N_2 peak area, as shown ~~so~~ in equation 4-7. From these response factors, the molar flowrate of each compound could ~~thus~~ be determined, based on the N_2 flow rate, as shown in equation 4-8.

$$R_i = \frac{A_{N_2}}{A_i} \cdot \frac{C_i}{C_{N_2}} \qquad 4\text{-}7$$

$$n_i = R_i \cdot n_{N_2} \cdot \frac{A_i}{A_{N_2}} \qquad 4\text{-}8$$

Where

R_i is the response factor for the compound of interest i,

A_i is the area of the compound of interest i,

C_i is the known concentration from calibration cylinder,

n_i is the molar flowrate of the compound of interest i.

4.6.2 Liquid products identification and quantification

Liquid products identification and quantification was performed with HPLC.

A Thermoscientific Spectra system AS3000, connected to Thermoscientific Spectra P4000 (pump) and an ERC RefractorMax520 (RI detector) as the HPLC setup. A 5 mM solution of sulphuric acid (Merck, 98%, H_2SO_4) was used as mobile phase, while an Aminex HPX-87H column was used as the stationary phase. The mobile phase flowrate was set at 0.5 ml/min, with each sample run time set at 30 min. Both the column oven and the RI detector were set at a temperature of 40 °C, while the pump was set at a pressure of 937 PSI.

Standards in the range 0 g/L and 1 g/L were prepared for methanol, ethanol and formic acid, using the prepared mobile phase as a diluent.

4.6.3 Computation of electrochemical performance

To determine the electrochemical performance of a catalyst, the current density, and faradaic efficiency were computed.

The current density was computed as the average current over CA performance evaluation and normalised by the geometric area of the working electrode, which was determined from TGA. The current density was used to indicate the activity of the catalyst.

$$Current\ density = \frac{Average\ current}{Geometric\ area\ of\ GDE} \qquad 4\text{-}9$$

The faradaic efficiency (FE) of the catalyst was computed to signify the product selectivity of the catalyst at a certain potential. This is since the FE shows the fraction of electrons dedicated to the formation of a certain product relative to the total electrons. For liquid and gas products the FE was computed using equations 4-10 and 4-11, respectively.

Liquid products

$$FE = \frac{\dot{n}_i \cdot n_e \cdot F}{C_T} \tag{4-10}$$

Gas products

$$FE = \frac{n_i \cdot n_{e^-,i} \cdot F}{I_{at\ sampling\ time} \cdot \frac{60}{\dot{V}}} \tag{4-11}$$

Where,

$\dot{n}_i$ is molar flowrate of product i

n_i is the total number of moles of product i computed based on equation 4-8

$n_{e^-,i}$ is the number electrons required for the formation of one mole of product i

F is Faradays number which is the amount of charge per mole of electrons (96485C/ mol_e^-)

C_T is the total charge transferred

$I_{at\ sampling\ time}$ is the average current at the time of gas sampling

$\dot{V}$ is the gas inlet gas volumetric flowrate.

4.7 Electrocatalytic characterisation with rotating ring disc electrode

The catalytic evaluation of the synthesised supported nanoparticles was also performed in a conventional three-electrode cell (Gamry Instruments). Pt wire and Ag/AgCl was used as the counter and reference electrodes, respectively. An RRDE was used as the working electrode.

The following methodology was adapted from a study by Zhu et al. (2018).

4.7.1 Cell setup

The RRDE consists of a glassy carbon electrode centre - where the prepared catalyst can be deposited - and a Pt ring, shown in Figure 4-7. The ring and disc are separated from each other via a PTFE gap. The design of the RRDE allows for the glassy carbon and Pt ring to be at different potentials. For this study, as products are formed, the rotation of the RRDE allows for them to be swept onto the Pt ring, where an oxidising potential is applied. The Pt ring is set at a potential that will lead to the oxidation of products, as soon as they are formed on the glassy carbon electrode ring (Zhu et al., 2018). Hence, this process can lead to the immediate identification of products formed on the electrode.

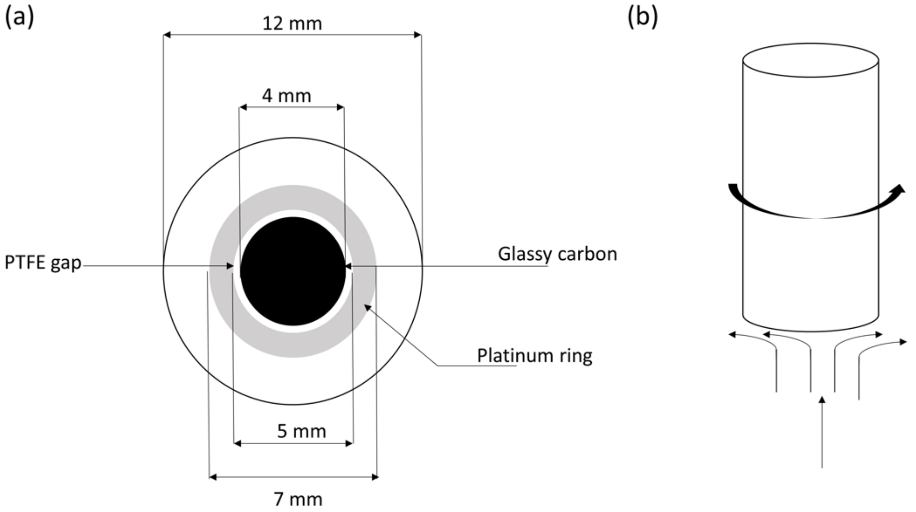

Figure 4-7: Illustration of RRDE, (a) concentric view with dimensions, (b) axial view illustrating the flow direction of electrolyte due to electrode rotation.

For all the experiments a 0.1M $NaHCO_3$ (Sigma-Aldrich, ACS reagent 99.7%) electrolyte was prepared using 18.2 $M\Omega.\mathrm{cm}$ deionised water.

4.7.2 RRDE ink and electrode preparation

The ink preparation method for the catalysts tested in the RRDE was adapted from a study by Zhu et al. (2018). To prepare the catalyst ink, 14.2 mg of supported catalyst was mixed with 10 ml isopropanol, 3 ml of 18.2 $M\Omega.cm$ deionised water, and 62.8 μL of a 5 wt% Nafion® solution. This colloid was then ultrasonicated for an hour. For each run, the electrode was mechanically polished with alumina paste with subsequent decreasing particle size, from 1 µm to 0.05 µm alumina. The electrode was then rinsed in deionised water.

The ink was deposited onto the electrode in multiple steps. A micropipette was used to deposit 5 μL of ink onto the disc of the RRDE. The electrode was dried under a beaker at normal atmospheric conditions until a uniform film of catalyst had formed on the electrode. This deposition process was repeated five more times, to bring the total volume of ink used in each run to 30 μL. The final supported catalyst loading on the disc was therefore 0.0326 mg.

4.7.3 Electrochemical products calibration

For the electrochemical reduction of carbon dioxide, a range of products can be formed. These products will have a peak at different oxidising potentials. To determine the position of the peaks, cyclic voltammetry was performed on the Pt-ring of the RRDE, with the pure products in the electrolyte. The RRDE was calibrated for the following products: methanol, formate, and carbon monoxide, as these compounds are electroactive.

To characterise the Pt ring electrode's electrochemistry two solutions were prepared with 120 ml of 0.1 M $NaHCO_3$ electrolyte, where: (i) 15 ml of methanol was added, (ii) 5g of Potassium formate was added. Each of these solutions were added to the electrochemical cell where Ar was first bubbled at a flow rate of 20 ml/min for a period of 30 mins. The electrolyte was then saturated with CO_2 via its bubbling at a 20 ml/min for a period of 30 mins. The RRDE was rotated at 1500 rpm, and the disc was without any deposited catalyst. Five cyclic voltammetry scans were performed on the Pt ring electrode over a potential range of -0.210 to 1.090 V vs Ag/AgCl, and a scan rate of 100 mV.s^{-1}. To perform CO characterisation on the Pt ring, similar experiments were performed, however, these were done with a blank 0.1M $NaHCO_3$ electrolyte, where CO was bubbled at a rate of 20 ml/min.

4.7.4 RRDE cyclic voltammetry

Two types of cyclic voltammetry experiments were performed: (i) scan of disc potential, while holding the ring at a fixed potential, which were performed in Ar saturated, and CO_2 saturated electrolytes; (ii) holding the disc at fixed potentials, whilst scanning the ring potential. These were all done in 140 ml of 0.1M $NaHCO_3$ electrolyte for each of the prepared catalysts.

The cyclic voltammetry of the disc whilst holding the ring potential at a fixed potential was done to compare the activity of the catalysts at different gas conditions. To do this, Ar was bubbled through the electrolyte for a period of 30 mins. Five cyclic voltammetry scans were applied on the disc in the voltage bounds -0.210 to -1.910 V vs Ag/AgCl and scan rate of 100 mV.s^{-1}, whilst the ring was held at 0.690 V vs Ag/AgCl, with the RRDE rotating via a shaft at 1500 rpm. The same CV experiment was then performed for CO_2, which was first also bubbled through the electrolyte for 30 mins.

After these experiments with CO_2 still bubbling through the electrolyte, the disc was held at a fixed potential, whilst cyclic voltammetry of the ring was performed. The disc was held at potentials between -0.910 V to -1.910 V vs Ag/AgCl at step increases of 100 mV. For each of these fixed disc potentials, five ring cyclic voltammetry scans were performed in the potential bounds -0.210 to 1.090 V vs Ag/AgCl at a scan rate of 100 mV.s^{-1}, and RRDE rotation of 1500 rpm. The peak positions obtained here will be compared to the calibration data, to identify the products formed at each of the fixed disc potentials.

5 Chapter 5 – Results and Discussion

This section of the report will present and discuss the characterisation of the synthesised nanoparticles, and it will finally present the electrocatalytic evaluation experiments of the synthesised nanoparticles.

5.1 Development of synthesis methodology for CuAg bimetallic nanoparticles

A wet chemical synthesis route towards the production of carbon supported CuAg nanoparticles was investigated. The conditions of success for this was to ensure that nanoparticles with a narrow size distribution and limited agglomeration could be synthesised. The process is divided into three unique steps: the synthesis of unsupported nanoparticles, washing of unsupported nanoparticles and the deposition of nanoparticles onto carbon support. In all the process steps, CuAg(50:50) prepared without the use of hexadecylamine (HDA) surfactant was used as a model sample. This synthesis route and CuAg ratio were chosen to evaluate the effect of metal to metal interaction on particle morphology.

A nanoparticle growth series was developed to understand the growth mechanism followed by CuAg nanoparticles. This was done by taking TEM samples at specific periods during the synthesis. To establish appropriate synthesis conditions, the effect of total precursor concentration, synthesis temperature, and washing solvents on nanoparticle morphology was investigated.

5.1.1 CuAg nanoparticle growth series

To investigate the formation of CuAg nanoparticles, TEM samples were taken over the synthesis period. Figure 5-1 shows the CuAg(50:50) nanoparticle growth time series. After the addition of the last drop of reducing agent, $NaBH_4$, the particles exhibit the widest size distribution and largest mean particle size. As the addition of $NaBH_4$ occurred over an extended period of 15 mins, the synthesis vessel contains both newly formed particle nuclei and particle clusters that have already formed through nuclei aggregation. As the synthesis progresses, the particle size distribution becomes narrower, as the rate of nucleation decreases, due to the lower precursor and reducing agent concentration. After an hour of synthesis, monodisperse nanoparticles are formed (Figure 5-1 (c)). Figure 5-1 shows that the CuAg(50:50) follows the classic LaMer mechanism for nanoparticle formation (Polte, 2015).

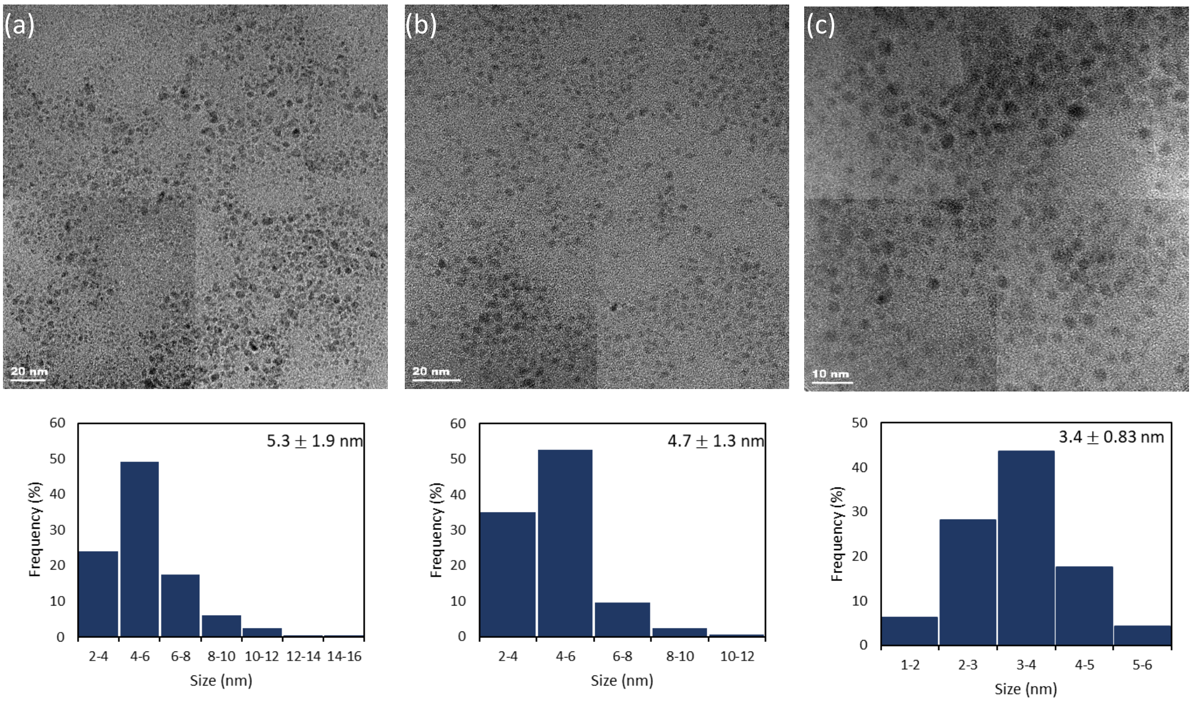

Figure 5-1: Time series of the growth of nanoparticles during synthesis. **A**: 15 mins (after the last drop of $NaBH_4$), **B**: 45 mins, **C**: 1h.

5.1.2 Influence of precursor concentration and temperature on nanoparticle morphology

Experiments were conducted to investigate the appropriate precursor concentrations that would culminate into a narrow particle size distribution. Figure 5-2 shows the TEM images and particle size distribution of nanoparticles synthesised at different precursor concentrations. Spherical particles are produced for each of the precursor concentrations. Doubling the precursor concentration from 1.25 mM to 3.5 mM has a limited effect on the particle size distribution. However, increasing the precursor concentration to 7 mM widens the particle size distribution and increases the mean particle size. This is since a precursor concentration 7mM has a higher rate of nucleation and particle aggregation relative to nanoparticles synthesised at a precursor concentration of 1.25 mM and 3.5 mM. Therefore, the precursor concentration used for further synthesis of CuAg nanoparticles was 3.5 mM as this concentration would ensure a high yield of nanoparticles for the same synthesis volume while achieving a narrow particle size distribution and small mean particle.

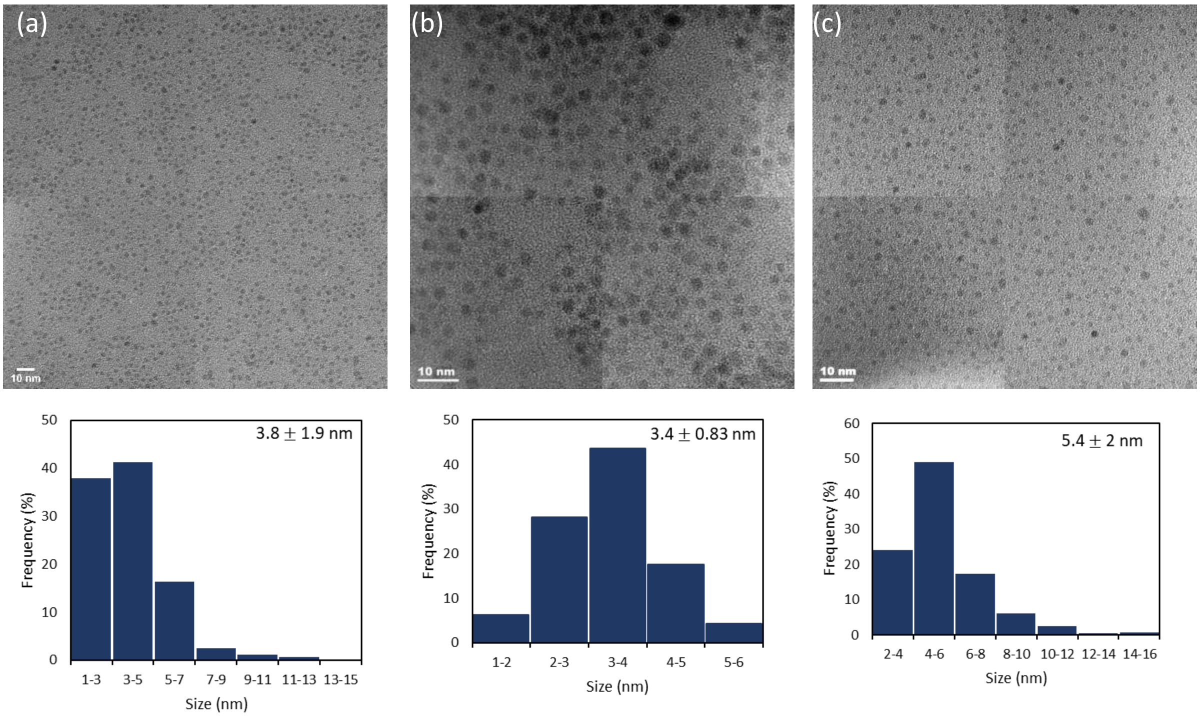

Figure 5-2: CuAg(50:50) nanoparticles synthesised at different precursor concentrations and 0 °C, after 1 h. Total metal concentration: (a) 1.25 mM, (b) 3.5 mM, (c) 7.0 mM.

Experiments were conducted at a fixed precursor concentration to determine the effect of temperature on particle morphology, which is shown in Figure 5-3. Figure 5-3 shows that the particle size and distribution increase and widen, respectively, with a temperature rise. At 25 °C there is slight aggregation of nanoparticles which continues to persist with a rise in temperature. The rise in temperature increases the rate of particle nucleation, leading to a high yield of new particles over the time period, thus a higher probability of particle collision. At 50 °C, monodisperse nanoparticles can still be observed, while some nanoparticles begin to cluster to form chains which would lead to a loss of surface area. Chain formation of the CuAg system has been observed in literature, with the chain links being shown to occur due to Cu oxidation, which binds multiple nanoparticles (Deo Malviya, Srivastava & Chattopadhyay, 2017).

X-ray diffractograms of the three samples, Figure 5-4, show that both Cu and Ag phases are present in all the nanoparticle samples. Cu oxidation is not observed, though Cu is highly susceptible to oxidation at this temperature range (Kim et al., 2014). This observation is further discussed in section 5.2.2. As the synthesis temperature rises, a slight positive shift of the Ag (111) Bragg angle value is observed, which corresponds to a decrease in the lattice parameter, and therefore a possible incorporation of the Cu in the Ag lattice. Additionally, the sharpness of the diffractogram increases with a rise in synthesis temperature. This indicates that at higher temperatures, a more ordered crystal structure is obtained.

To limit the loss in surface area during agglomeration, nanoparticles synthesised via Method A and Method B, were synthesised at a total metal precursor concentration of 3.5mM and a temperature of 0 °C.

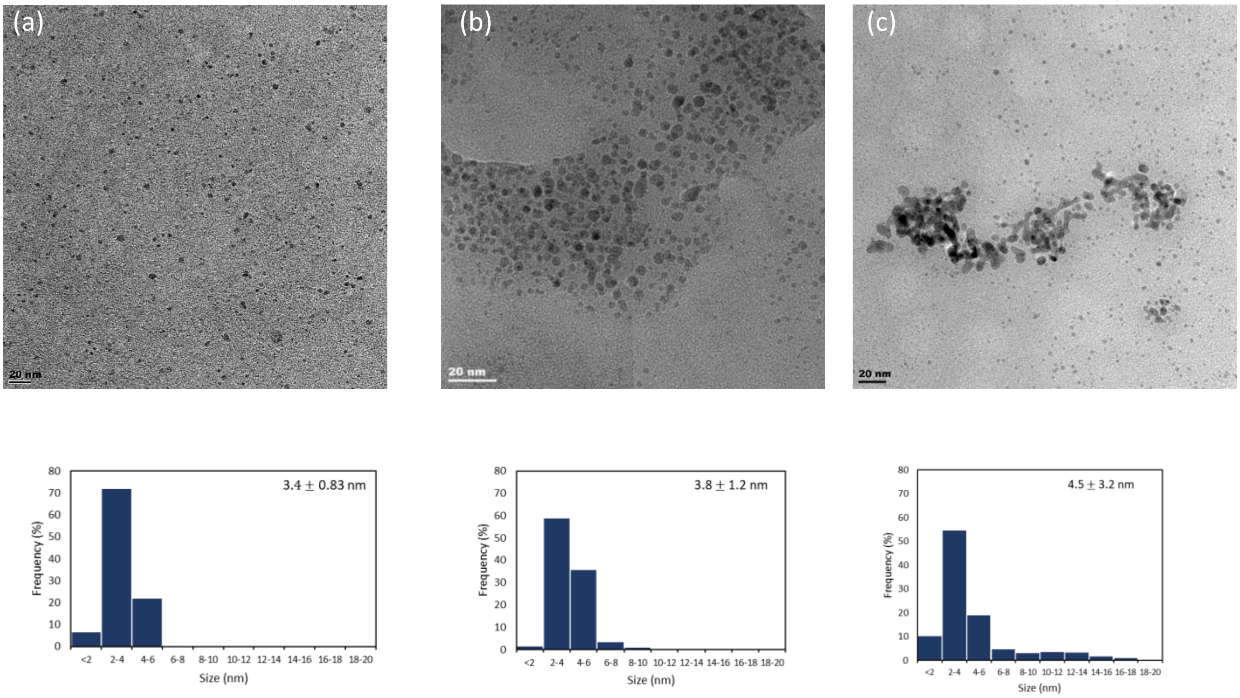

Figure 5-3: CuAg(50:50) nanoparticles synthesised at different temperatures, and a fixed precursor concentration of 3.5 mM for 1h. (a) 0 °C, (b) 25 °C, (c) 50 °C.

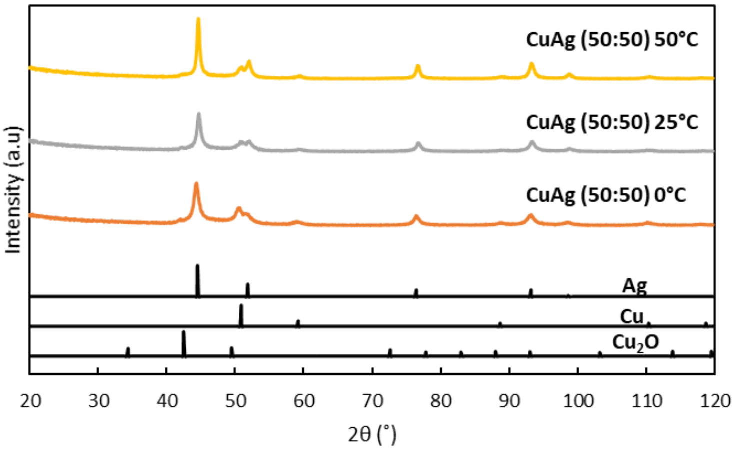

Figure 5-4: X-ray diffractograms of CuAg(50:50) synthesised under different temperature conditions.

5.1.3 Nanoparticle deposition on carbon support

After one-hour of synthesis (Figure 5-1 (c)), the as-prepared nanoparticles were left to settle for 15 minutes, after which the supernatant was decanted, and a small layer of solvent was left above the nanoparticles. The resulting colloid was then split into four equal volumes and washed with various combination of solvents (ethanol, water, and acetone) as shown in Figure 5-5. The purpose of washing procedure was to remove the excess reducing agent and metal precursor ligands.

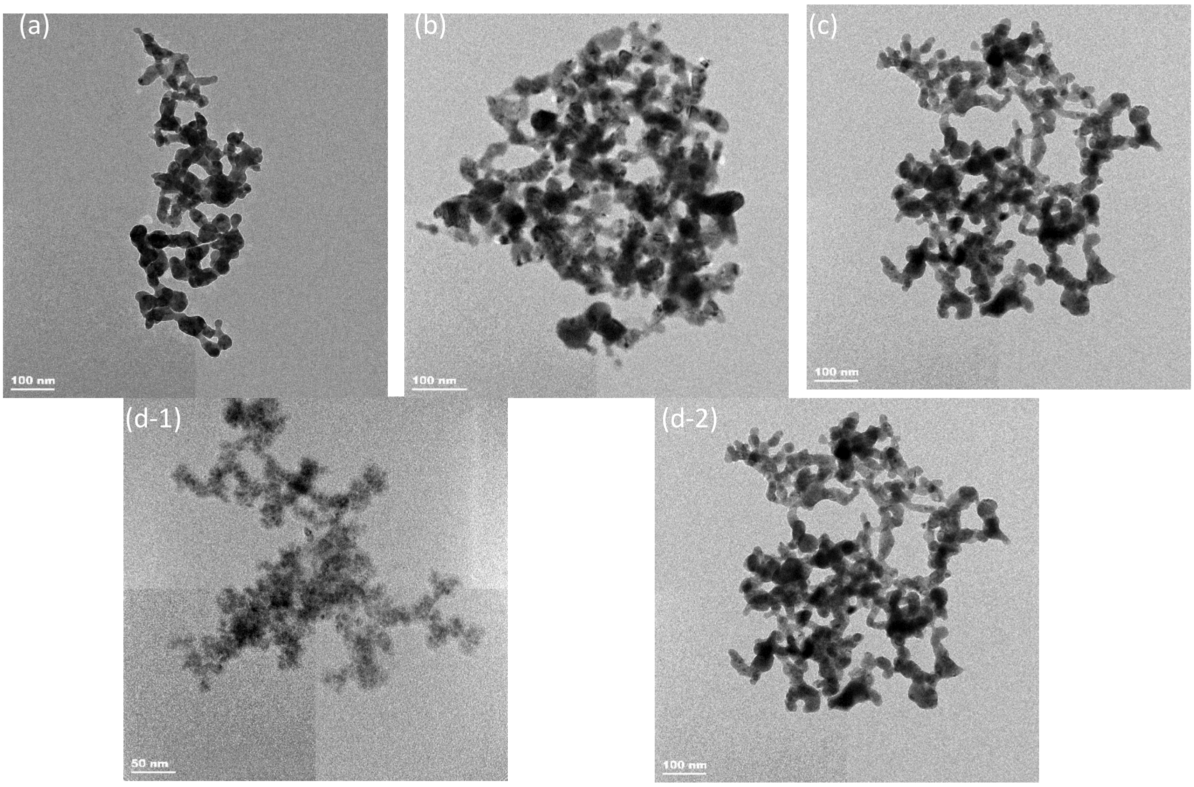

Figure 5-5: The effects of washing with various solvents, with each round of washing performed for 15 minutes with stirring at 500 rpm. (a) washing with ethanol, followed by water, and then acetone, (b) washing with acetone, (c) washing with water, (d-1): one round of washing with ethanol, (d-2): two rounds of washing with ethanol.

In contrast to Figure 5-1 (c), Figure 5-5 indicates that the immediate washing of the as-prepared nanoparticles with solvents culminates in nanoparticle agglomeration. As this limits the available nanoparticle surface area for reaction, it is undesired. $NaBH_4$ has been shown to play the role of a reducing agent, as well as capping nanoparticles by forming a BH_4^- shell (Das et al., 2014). Therefore, the removal of $NaBH_4$ through the washing process leads to nanoparticle agglomeration.

To limit the extent of agglomeration, deposition of nanoparticles onto the carbon support prior to washing was investigated. This was performed by supporting the as-prepared nanoparticles via their sonication with the carbon support. The solvent was then removed through rotary evaporation, which was followed by washing with water, ethanol, and acetone. Finally, the supported nanoparticles were dried in an oven operated at 60 °C. Figure 5-6 which shows the supported nanoparticles after drying indicates that agglomeration was limited, with free nanoparticles widely distributed throughout the support without chain formation.

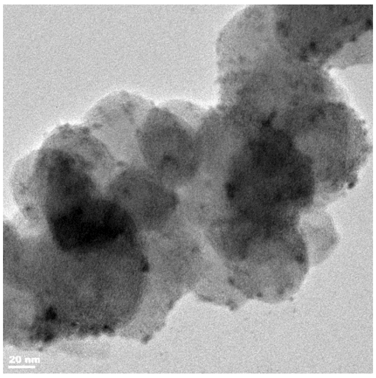

Figure 5-6: CuAg(50:50) supported on carbon after washing and drying in an oven operated at 60 °C.

5.2 Catalyst Physical Characterisation

Two methods were followed for the synthesis of bimetallic catalysts. The distinction between these two methods was in that catalysts produced via Method A were synthesised in the absence of HDA, while catalysts synthesised with Method B included the addition of HDA at the beginning of synthesis, at a total metal precursor to HDA molar ratio of 1:2.5.

5.2.1 Monometals physical characterisation

5.2.1.1 Transmission electron microscopy

Monometallic catalysts were prepared via Method B in the presence of HDA. Figure 5-7 shows the TEM images of the as prepared and supported nanoparticles, while Figure 5-8 shows the particles size distribution. The monometal synthesis yielded spherical nanoparticles of CuAg (100:0) and CuAg (0:100) catalysts. The as prepared CuAg (0:100) sample has a broad particle size distribution, with a standard deviation of 2.5 nm. A majority of CuAg(0:100) nanoparticles lie in the range 3 to 9 nm, while nanoparticles up to 17 nm could also be observed. In contrast, CuAg(100:00) has a smaller mean particle size and a narrower particle size distribution, with a standard deviation of 1.6 nm.

This significant difference in the monometals particle size distribution is due to their difference in electron affinity. The standard electrode potential for Ag^+/Ag^0 is 0.78 eV, which is higher than that of Cu^{2+}/Cu^0 of 0.34 eV. Ag^+ ions are reduced much faster than Cu^{2+} ions, which leads to Ag having a higher rate of nucleation than Cu. Over the one hour synthesis period, Ag nuclei have more time to undergo the growth phase in comparison to Cu nuclei, hence CuAg (0:100) has a larger mean particle size relative to CuAg (100:0) as shown in Figure 5-7.

Figure 5-8 shows that the particle size distribution for both monometallic catalysts shifted positively to larger particles following the nanoparticle deposition onto the carbon support. In particular, the mean particle size of as prepared CuAg(0:100) grew by 83%, from 6.5 nm to 11.9 nm, with the particle size distribution also widening. In contrast, the mean particle size of CuAg(100:0) grew by 39%, with all observed nanoparticles being below 12 nm. This shift in the particle size distribution indicates that aggregation occurred during the carbon deposition step. This is due to the agitation introduced when the nanoparticles were sonicated with the support and the addition of more solvent during this step. This culminates in the removal of surfactant from the nanoparticle surface, thus nanoparticles aggregate. Though the nanoparticles grow during the deposition step, nanoparticle chain formation is not observed, as previously seen in Figure 5-5.

CuAg(100:0)_B CuAg(100:0)/C_B

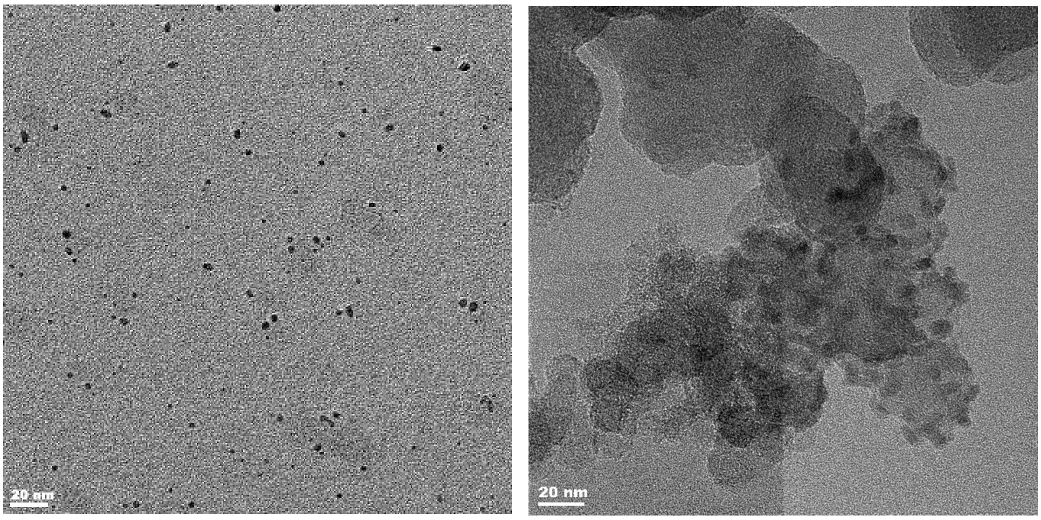

CuAg(0:100)_B CuAg(0:100)/C_B

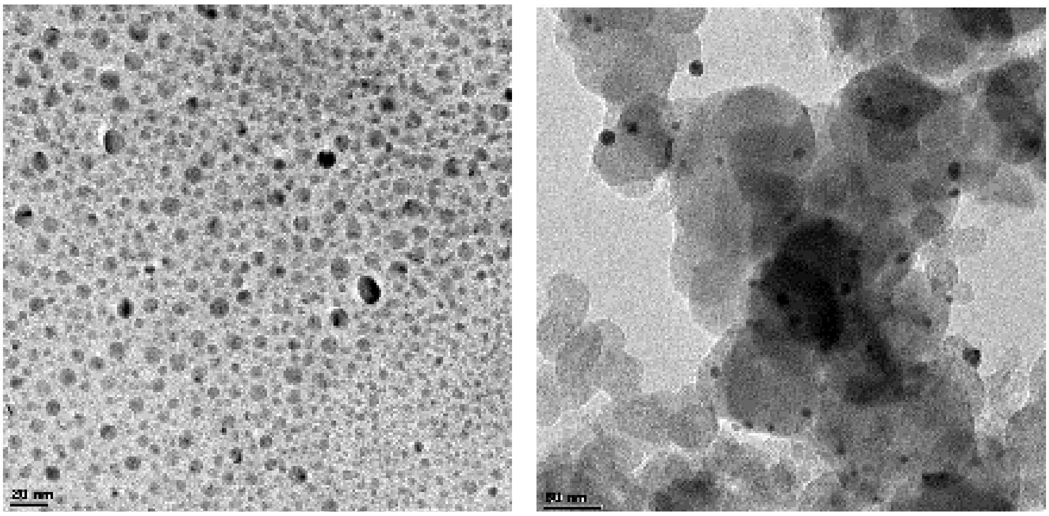

Figure 5-7: TEM images of as-prepared and supported bimetallic nanoparticles prepared in the presence of HDA at 0°C (Method B).

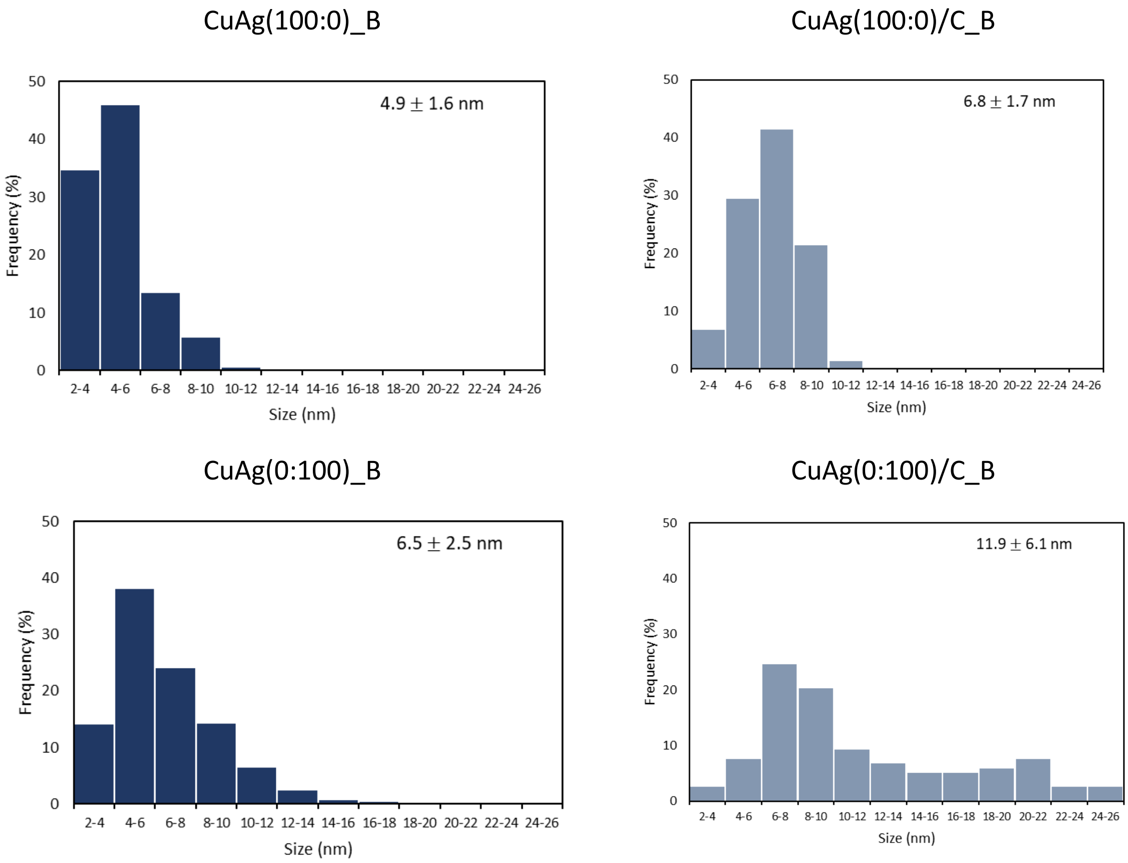

Figure 5-8: Particle size distribution histograms for as prepared and supported monometallic nanoparticles synthesised via Method B.

5.2.1.2 Powder X-ray Diffraction (PXRD)

Figure 5-9 shows the PXRD diffractograms of the supported monometallic catalysts.

The CuAg(0:100)/C_B and CuAg(100:0)/C_B monometal diffractograms display distinct diffraction lines demonstrating the high crystallinity of the catalysts. The CuAg(0:100)/C_B diffractogram shows that a pure Ag fcc phase was formed without impurities. On the other hand, the CuAg(100:0)/C_B diffractogram indicates the presence of both the Cu and Cu_2O phases. Cu oxidation most likely occurred during the drying step of the synthesis process, where a rotary evaporator was used. The broad Cu_2O diffraction line and its lower intensity relative to the Cu phase indicates that the possible structure of the CuAg(100:0)/C_B catalyst is one where a thin layer of Cu_2O is formed around the Cu core of the nanoparticles (Hung, Ling-I et al., 2010). The diffraction lines below a Bragg's angle of 30° are attributed to the Vulcan (XC-72R) support.

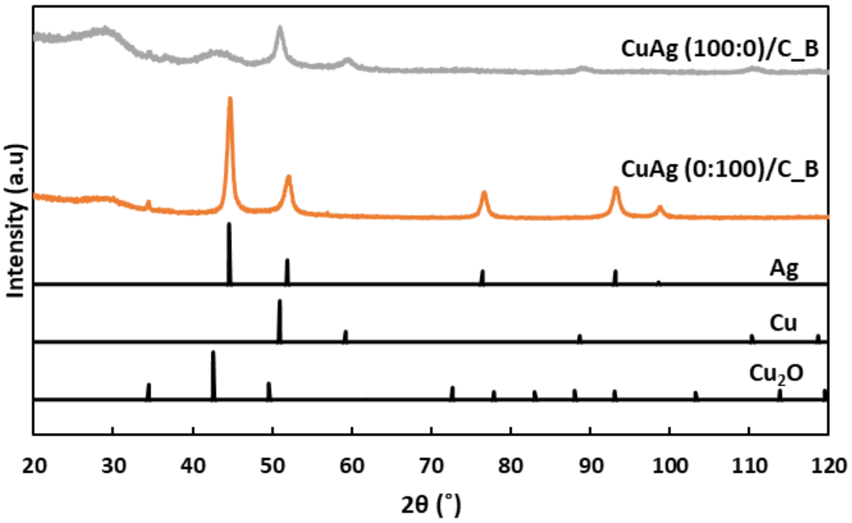

Figure 5-9: X-ray Diffraction of CuAg(100:0)/C_B, and CuAg(0:100)/C_B

5.2.1.3 Thermo-gravimetric Analysis (TGA)

Thermo-gravimetric analysis was used to determine the total catalyst metal loading. Figure 5-10 shows the weight vs temperature profile of the supported monometals. The weight loss below 150 °C is attributable to the evaporation of absorbed water, while the weight loss between 150 °C and 350 °C is due to the oxidation of residual HDA surfactant. Above 350 °C, the Vulcan (XC-72R) oxidation commences.

The loss of water and HDA was excluded in the determination of the metal loading. Table 5-1 compares the actual and expected metal loading of the two catalysts. These results show that the actual metal loading is close to the expected metal loading.

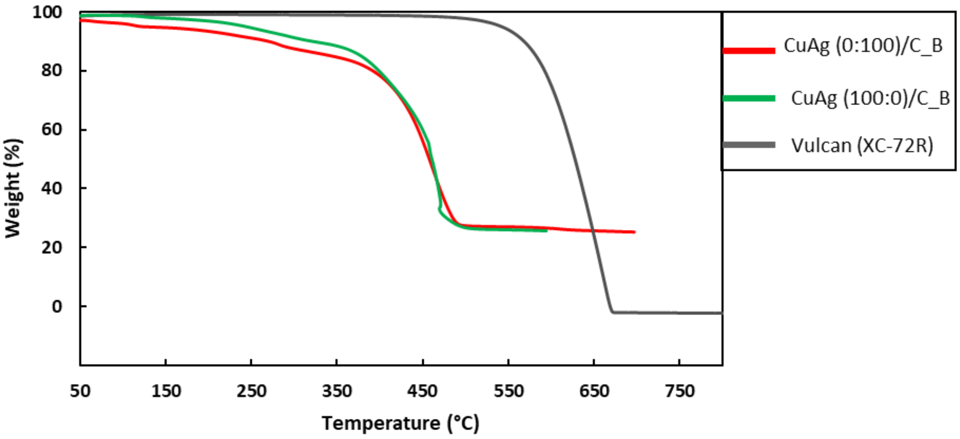

Figure 5-10: CuAg(1:0)/C, CuAg(0:1)/C, and Vulcan (XC-72R) Thermogravimetric analysis profile. Performed at a ramp rate of 5˚C/min in air which was fed at a rate 10 ml/min.

Table 5-1: Expected and actual metal loading of monometallic catalysts. These were obtained from TGA analysis.

Sample	Expected metal loading (wt%)	Actual Metal loading (wt%)
CuAg(100:0)/C_B	30.0	28.3
CuAg(0:100)/C_B	30.0	27.0

5.2.2 Method A bimetallic catalysts physical characterisation

5.2.2.1 Transmission electron microscopy (TEM)

Figure 5-11 shows the TEM images of as prepared and supported bimetallic nanoparticles synthesised via Method A (in the absence of HDA). Figure 5-12 and Table 5-2 show the particle size distribution of the nanoparticles and their composition, respectively.

The TEM images show that spherical nanoparticles were formed for all CuAg bimetallic ratios. The as prepared nanoparticles of CuAg(20:80)_A and CuAg(50:50)_A are monodispersed, while for CuAg(80:20)_A the nanoparticles are arranged in close clusters. The nanoparticles successfully adhered to the support with an even distribution across the support for all CuAg ratios.

There is no visible trend on the effect of CuAg ratio on the nanoparticle size distribution. The particle size distribution of the as prepared nanoparticles shows that CuAg(50:50)_A has the smallest mean particle size at 3.4 nm, followed by CuAg(20:80)_A at 4.8 nm, and CuAg(80:20)_A at 6.0 nm. The formation of nanoparticles is highly dependent on the rate in which reducing agent is added onto the synthesis vessel (Dongjo, Sunho & Jooho, 2006). Since the rate of reducing agent addition could not be controlled during synthesis, this had an effect on the rate of nanoparticle nucleation, and hence the nanoparticle growth.

Figure 5-12 further indicates that the carbon deposition process of the nanoparticles influences the nanoparticle morphology. This is since after carbon deposition the mean particle size for all CuAg bimetallic ratios increased and their particle size distribution widened significantly. During synthesis, the BH_4^- ions surround the nanoparticles to form a shell, which prevents the nanoparticle from agglomerating (Das et al., 2014). The deposition involves the addition of more solvent and sonication, which removes BH_4^- ions from the surface of the nanoparticles, culminating in nanoparticle agglomeration.

Table 5-2 shows that both Cu and Ag are present in the bimetallic phase, though there are deviations between the expected and actual CuAg ratio. All the samples have a higher Cu content than was expected.

CuAg(20:80)_A CuAg(20:80)/C_A

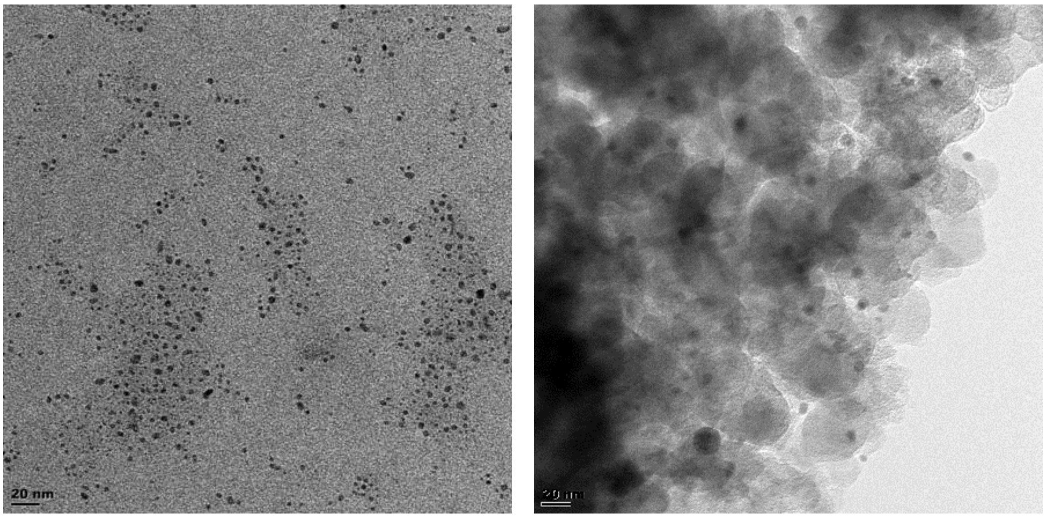

CuAg(50:50)_A CuAg(50:50)/C_A

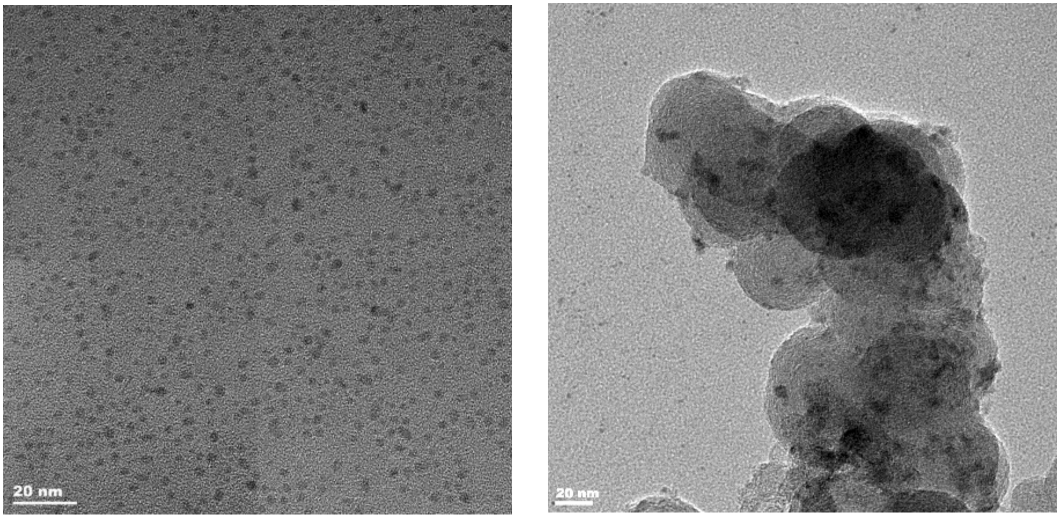

CuAg(80:20)_A CuAg(80:20)/C_A

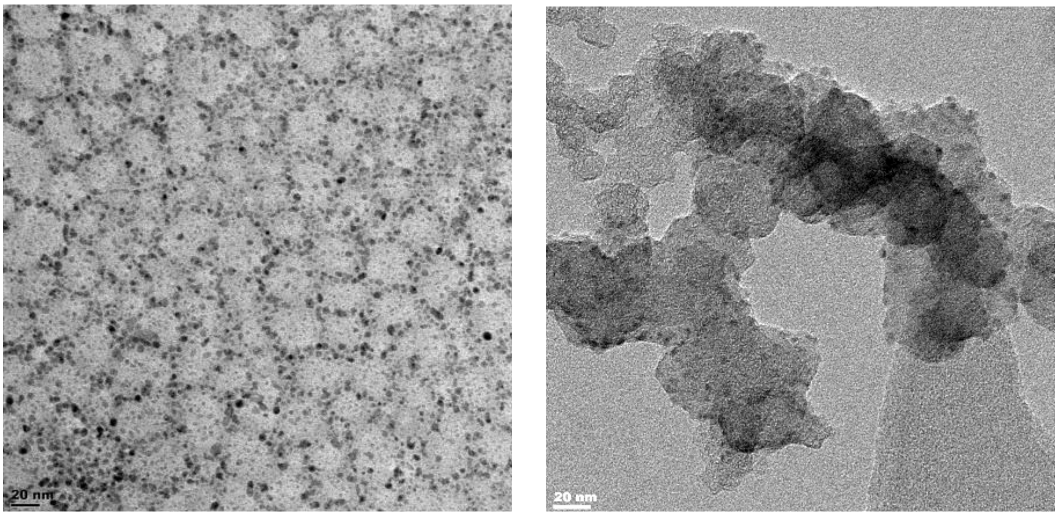

Figure 5-11: TEM images showing as-prepared and supported bimetallic nanoparticles prepared in the absence of HDA at 0°C (Method A).

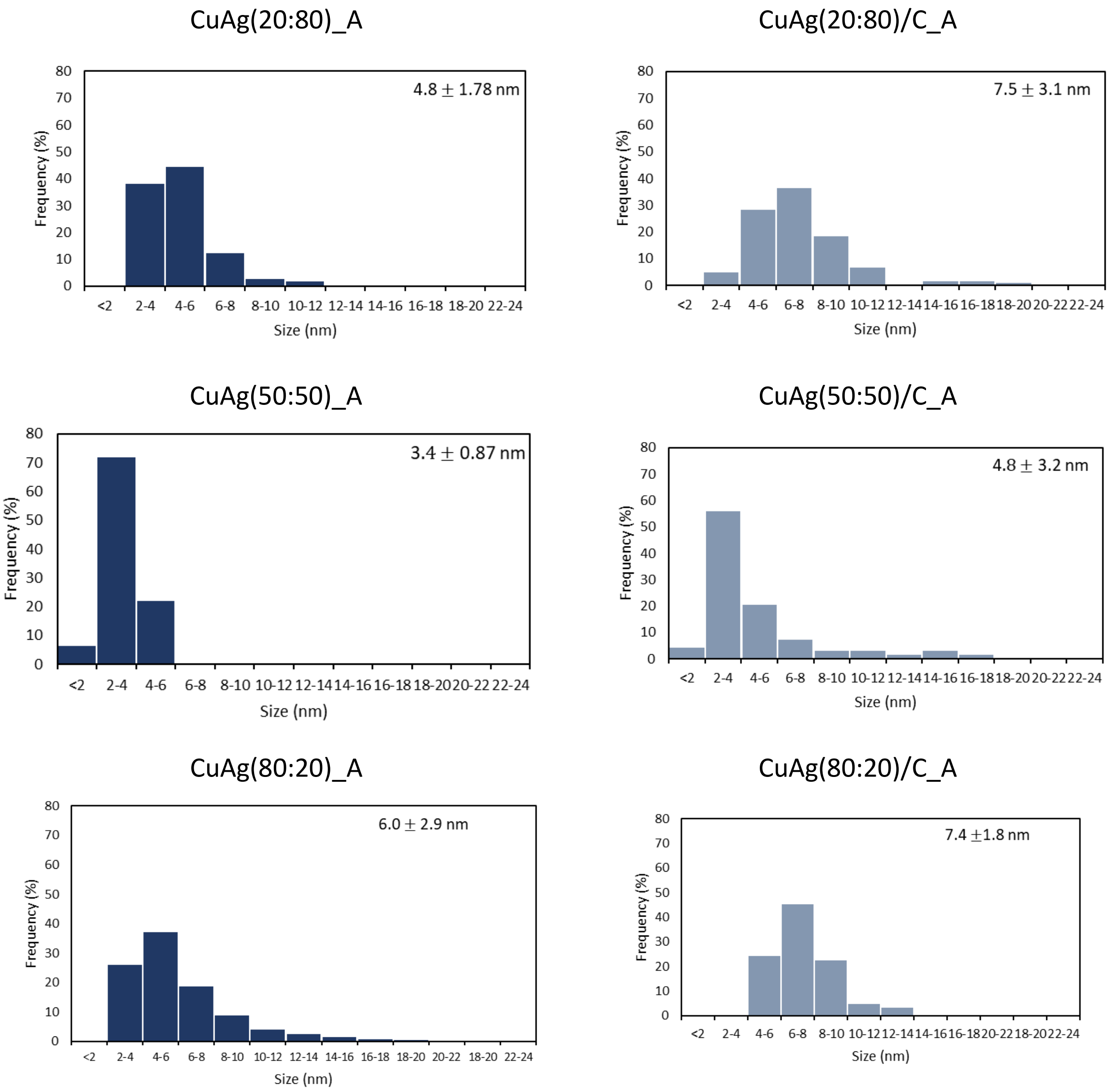

Figure 5-12: Particle size distribution histograms for as prepared and supported nanoparticles, synthesised via Method A.

Table 5-2: SEM EDX results of various ratios of supported nanoparticles prepared via Method A.

Sample	**Expected (at %)**		**SEM EDX (at %)**	
	Cu	**Ag**	**Cu**	**Ag**
CuAg(20:80)/C_A	20.0	80.0	28.7	71.3
CuAg(50:50)/C_A	50.0	50.0	53.8	46.2
CuAg(80:20)/C_A	80.0	20.0	83.3	16.7

5.2.2.2 Powder X-ray Diffraction (PXRD)

Powder XRD was performed on the prepared catalysts to determine the phases present, and this is presented in Figure 5-13. Both the fcc Cu and fcc Ag phase are present in each of the catalysts. As the Cu content increases, this coincides well with an increase in the Cu phase diffractogram intensity and a reduction in the Ag phase peak intensity, thus showing an increase in Cu content. This trend is also confirmed by the CuAg ratios presented in Table 5-2.

The presence of both Cu and Ag phases in all the samples does indicate that there is limited alloying in these samples. Hence a phase-separated bimetallic system is formed through the Method A synthesis route. However, the structure of the nanoparticles is unclear as to whether they have Ag core with a Cu rich shell or vice versa. It should be noted that there is a slight shift of the Ag(111) Bragg's angle position, which corresponds to a smaller lattice spacing, and therefore slight incorporation of Cu into the Ag lattice.

Relative to Figure 5-9, Figure 5-13 does not indicate the presence of XRD detectable Cu_2O. This demonstrates that introducing Ag stabilises the bulk Cu^0 phase. Figure 8-1 in appendices further shows that even after three months of storage at normal room conditions, there are no peak deviations indicating Cu oxidation. Previous studies hold differing views on the role of Ag in enhancing the oxidation resistance of the Cu phase. One perspective is that the Cu oxidation resistance may be due to Ag coating the Cu nanoparticles to form a shell, hence limiting Cu oxidation (Shang et al., 2018). Another perspective is that the difference in ionisation potential of Cu and Ag enhances Cu resistance to oxidation. This is since Cu is easily ionised relative to Ag, which leads to electron transfer from Cu to Ag and the non-availability of Cu electrons for reaction with oxygen (Kim et al., 2014, Zhang, Zailei et al., 2015).

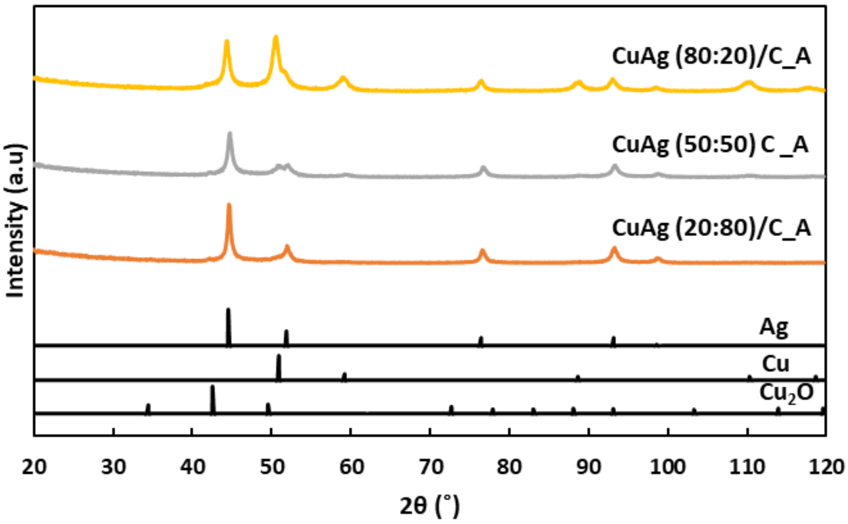

Figure 5-13: X-ray diffractogram of bimetallic samples synthesised via Method A.

5.2.2.3 Thermo-gravimetric Analysis (TGA)

Thermo-gravimetric analysis was performed to determine the total metal loading on the support, which is shown in Figure 5-14. Below 150°C, the drop in weight can be attributed to the evaporation of absorbed water. Between 150°C and 350°C, there is limited weight loss which demonstrates that the bimetallic catalysts did not contain any organic impurities. Above 350 °C the weight of the samples begins to decline sharply due to the carbonisation of the Vulcan support.

Table 5-3 indicates the final catalyst metal loading on the carbon support. The computation of the metal loading only considered weight loss above 350 °C. Table 5-3 shows that CuAg(20:80)/C_A and CuAg(50:50)/C_A are within a reasonable degree of the expected catalyst metal loading. However, the metal loading of CuAg(80:20)/C_A is 21% higher than the expected. In contrast to the other catalysts, the higher metal loading will significantly influence the activity of CuAg(80:20)/C_A.

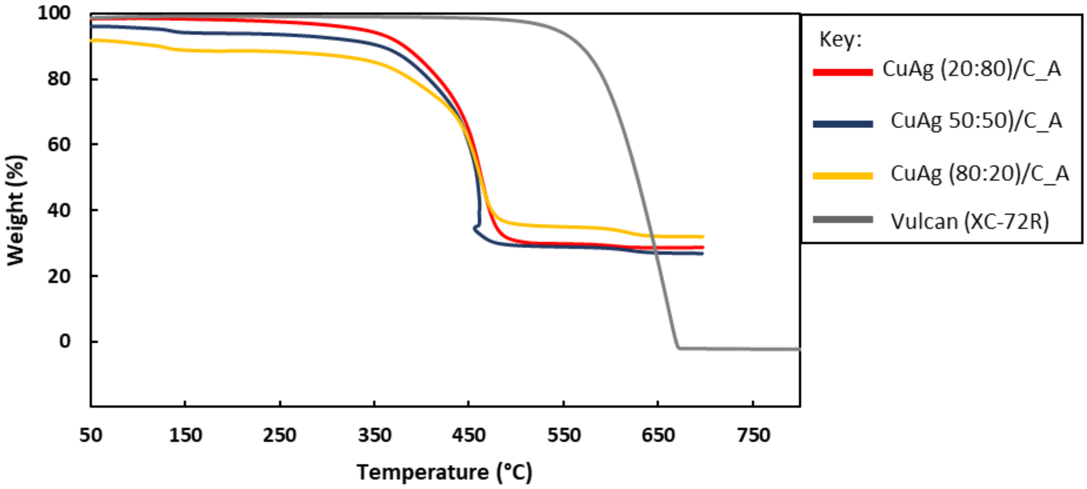

Figure 5-14: CuAg(20:80)/C_A, CuAg(50:50)/C_A, CuAg(80:20)/C_A and Vulcan (XC-72R) Thermogravimetric analysis profile. Performed at a ramp rate of 5˚C/min in air which was fed at a rate 10 ml/min.

Table 5-3: Expected and actual metal loading of bimetallic catalysts prepared via Method A. These were obtained from TGA analysis.

Sample	Expected metal loading (wt%)	Actual Metal loading (wt%)
CuAg(20:80)/C_A	30.0	29.5
CuAg(50:50)/C_A	30.0	28.7
CuAg(80:20)/C_A	30.0	36.2

5.2.3 Method B bimetallic catalysts physical characterisation

Bimetallic catalysts were also prepared via Method B. Synthesis via Method B followed the same procedure as Method A, except that HDA was added.

5.2.3.1 Transmission electron microscopy (TEM)

Figure 5-15 shows the TEM images of the as prepared and carbon supported nanoparticles. The particle size distribution and the nanoparticle metal composition is presented in Figure 5-16 and Table 5-4, respectively. Table 5-4 shows that the composition of prepared CuAg bimetallic nanoparticles does not deviate significantly from the expected composition.

Nanoparticles prepared via Method B yielded nanoparticles with larger mean particle sizes and a broader size distribution relative to catalysts prepared via Method A. This is since, HDA can act as both a reducing agent and surfactant (Hou et al., 2011). The addition of HDA in already excess sodium borohydride increases the yield of nuclei formed at the initial stages of the synthesis. However, since HDA is added at a low concentration – at a total metal concentration to HDA molar ratio of 1:2.5 – this limits nanoparticle capping potential.

The rise nanoparticle Cu content correlates with an increase in the mean particle size and a wider distribution (see Figure 5-15), with CuAg(80:20)_B having mean particle size 11% larger than CuAg(20:80)_B. Studies have shown that the rate of reducing agent or precursor addition significantly influences the nanoparticle size (Dongjo, Sunho & Jooho, 2006). Therefore, the role of the CuAg ratio on nanoparticle size is inconclusive as the rate of reducing agent addition during synthesis could not be controlled.

For all CuAg ratios, a majority of the as prepared nanoparticles lie below 11 nm in size. After the deposition process, the nanoparticle distribution is broader, and it shifts positively towards larger nanoparticles. This rise in mean particle size increases with nanoparticle Ag content. The positive shift in the nanoparticle size distribution shows that the smaller nanoparticles are unstable, and they transfer to the larger nanoparticles through the Ostwald ripening process (Gommes, 2019).

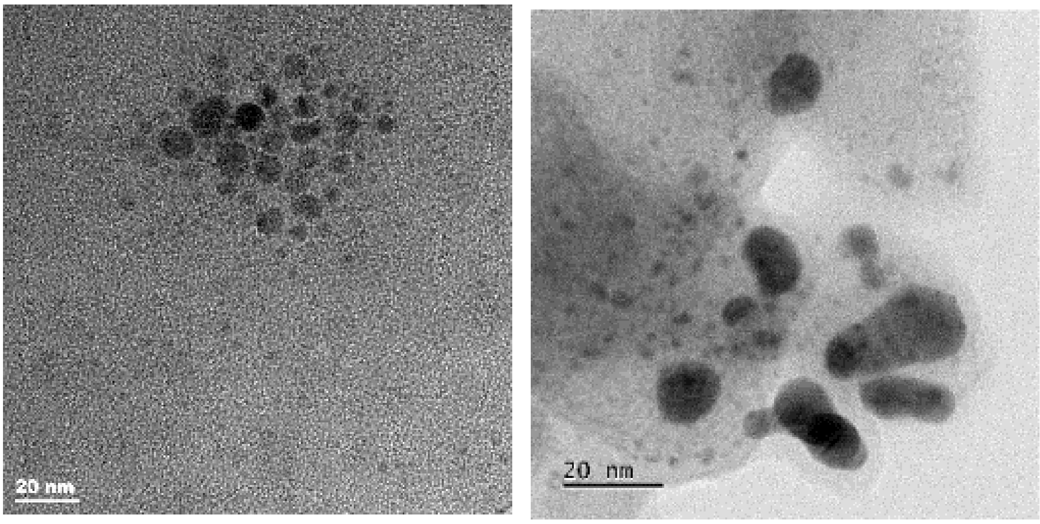
CuAg(20:80)_B

CuAg(20:80)/C_B

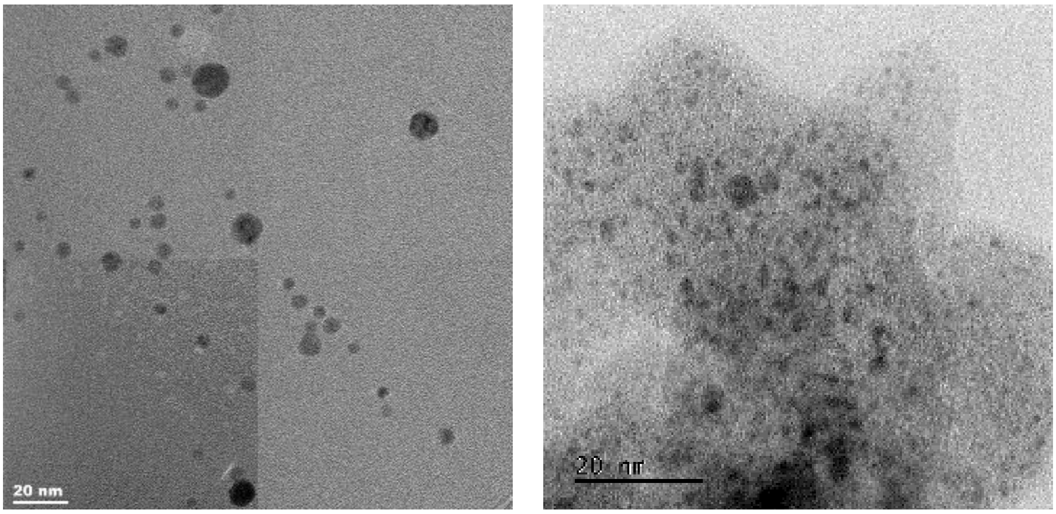
CuAg(50:50)_B

CuAg(50:50)/C_B

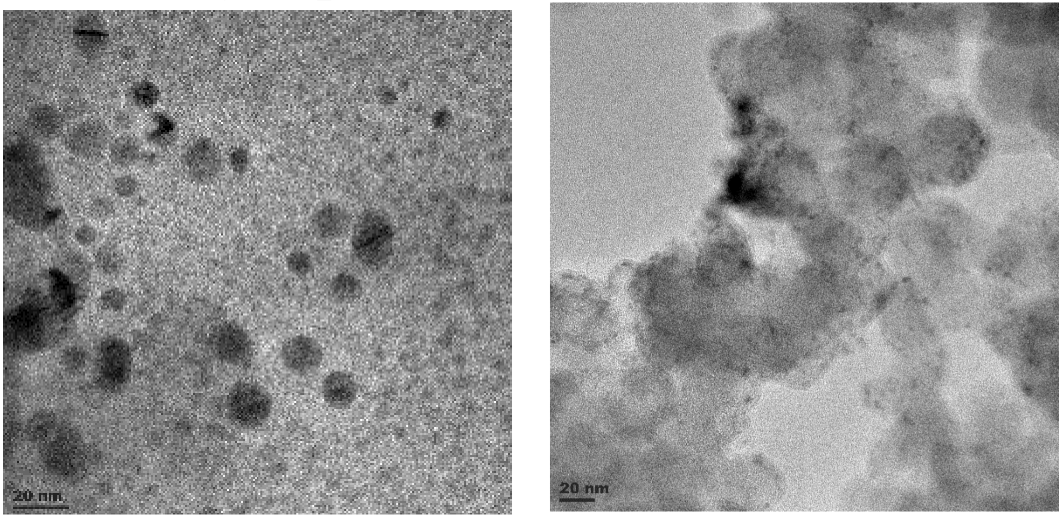
CuAg(80:20)_B

CuAg(80:20)/C_B

Figure 5-15: TEM images showing as-prepared and supported bimetallic nanoparticles prepared in the presence of HDA (Method B)

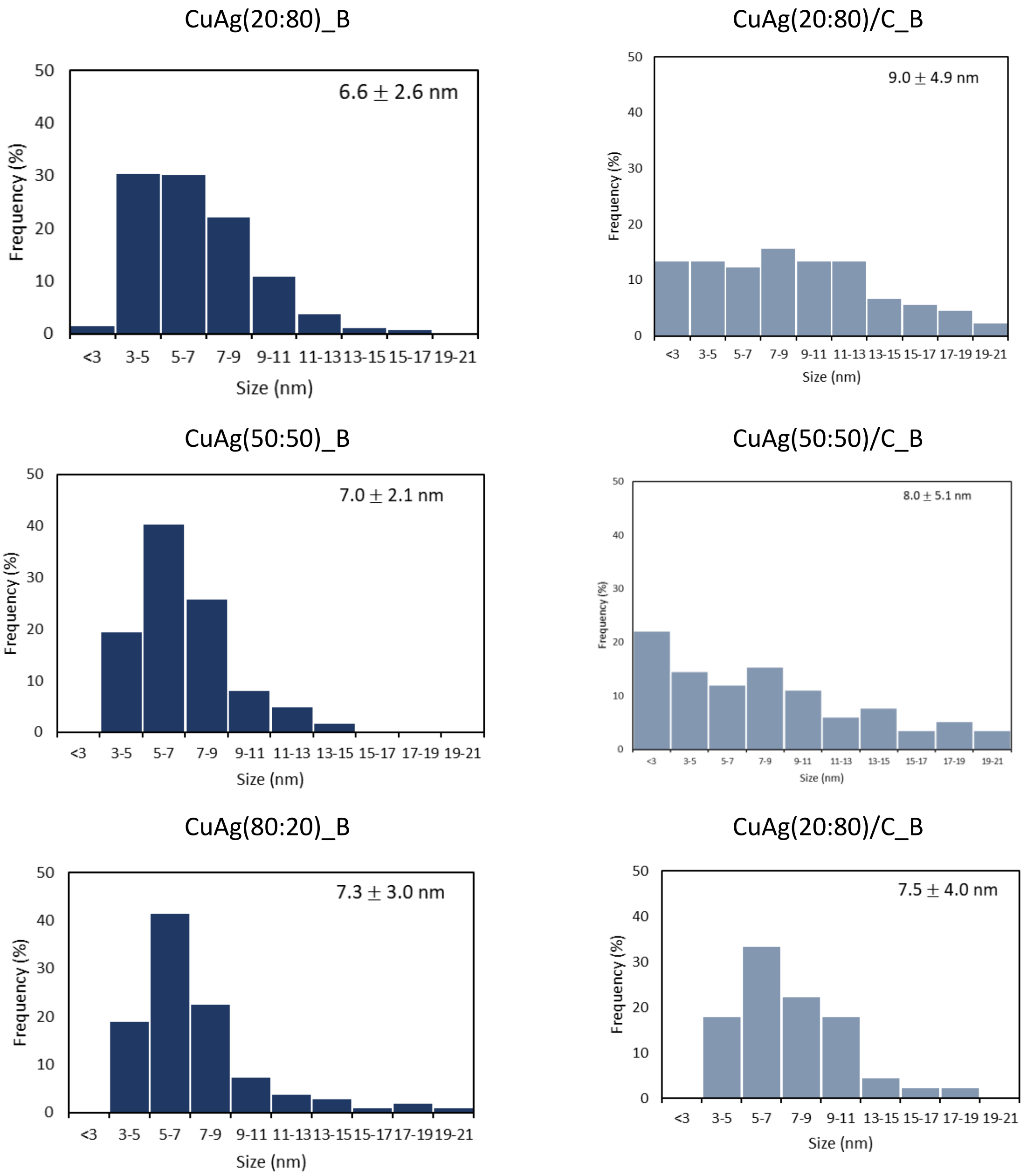

CuAg(20:80)_B

CuAg(20:80)/C_B

CuAg(50:50)_B

CuAg(50:50)/C_B

CuAg(80:20)_B

CuAg(20:80)/C_B

Figure 5-16: Particle size distribution histograms for as prepared and supported nanoparticles, synthesised via Method B.

Table 5-4: SEM EDX results of various ratios of supported nanoparticles prepared via Method B.

Sample	**Expected (at %)**		**SEM EDX (at %)**	
	Cu	**Ag**	**Cu**	**Ag**
CuAg(20:80)/C_B	20.0	80.0	22.6	77.4
CuAg(50:50)/C_B	50.0	50.0	60.0	40.0
CuAg(80:20)/C_B	80.0	20.0	79.4	20.6

HAADF-STEM and EDX images of carbon supported bimetallic nanoparticles prepared via Method B are presented in Figure 5-17. The EDX mapping shows that both Cu and Ag are present in the prepared nanoparticles, and they almost entirely overlap. The intensity of Ag reduces with a reduction in Ag content, and the EDX mapping is, therefore, in agreement with CuAg composition presented in Table 5-4. EDX mapping shows the presence of oxygen which follows the Cu intensity, demonstrating that some Cu atoms are oxidised.

As Ag has an atomic number (Z) larger than Cu, it will present a stronger intensity than Cu on HAADF images (Mourdikoudis, Pallares & Thanh, 2018). The HAADF images show that the nanoparticles have an invariable intensity, with overlapping and homogeneous EDX Cu and Ag intensities without phase segregation. This indicates that the bimetallic nanoparticles synthesised via Method B form a solid solution.

CuAg(20:80)/C_B

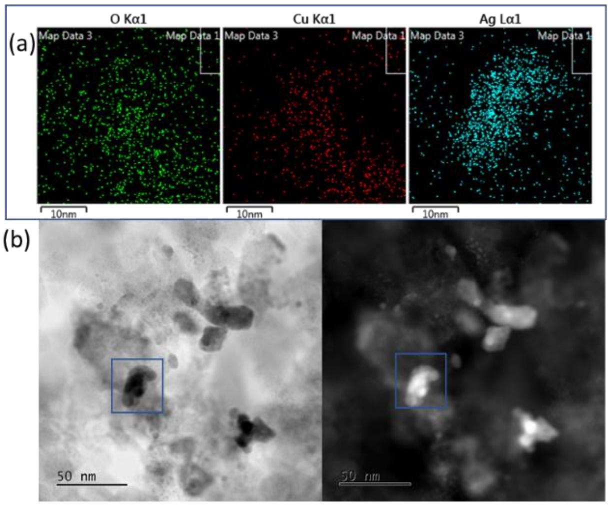

CuAg(50:50)/C_B

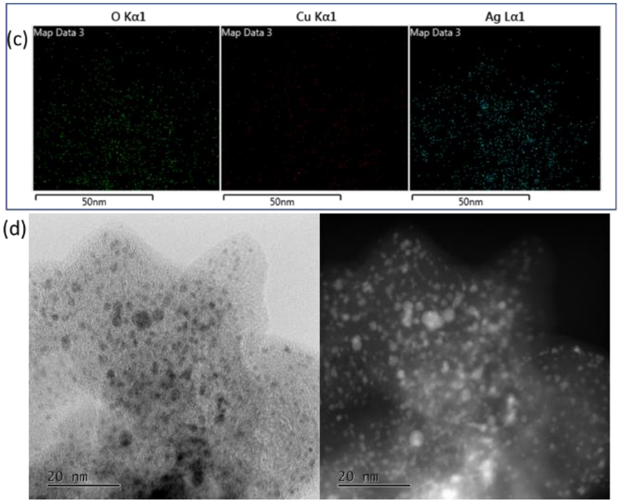

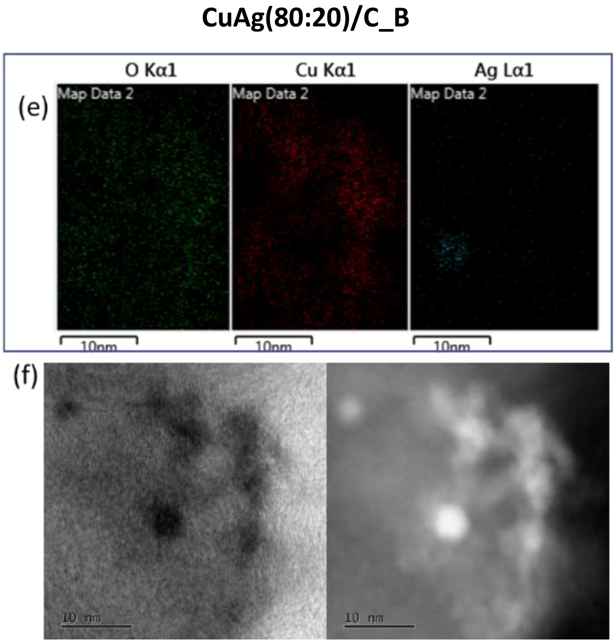

Figure 5-17: High angle annular dark field (HAADF) scanning electron microscope (STEM) images, and energy dispersive X-ray (EDX) mapping indicating O, Cu, and Ag mapping of carbon supported CuAg nanoparticles synthesised via Method B.

5.2.3.2 Powder X-ray Diffraction (PXRD)

X-ray diffraction of the bimetallic catalysts prepared via Method B was performed to determine the phases present, and this is presented in Figure 5-18.

The CuAg composition presented in Table 5-5 shows that both Cu and Ag are presented in each of the bimetallic nanoparticles. However, only a single phase can be observed through XRD, which is close to the Ag fcc phase. All the samples indicate a positive shift of the Bragg's angle, relative to the reference Ag (111) diffractogram. There is a slight increase in this shift, with the increase in sample Cu content, showing the reduction in lattice spacing. This further supports the formation of a CuAg solid solution when nanoparticles are synthesised via Method B (Balkan et al., 2020), as also observed in section 5.2.3.1. Additionally, an oxidised Cu phase in all the CuAg catalysts is not observed on each of the XRD diffractograms. Since XRD is a bulk analysis technique, it can be concluded that Cu oxidation, as observed in Figure 5-17, only occurs at the surface of the nanoparticles.

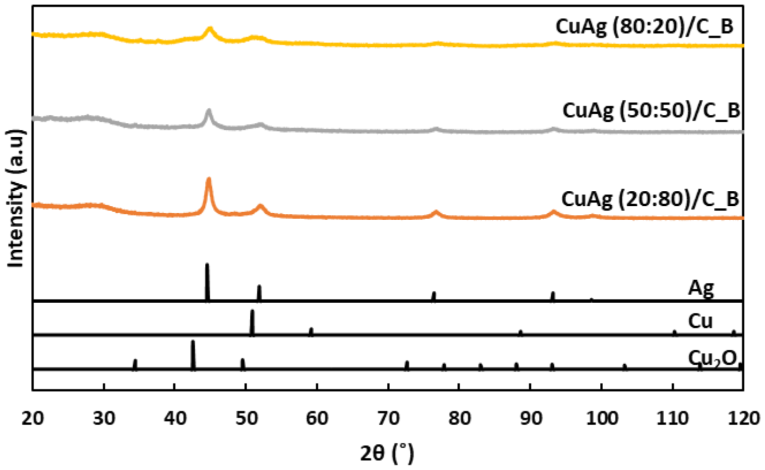

Figure 5-18: X-ray diffractogram of bimetallic samples synthesised in the presence of HDA.

5.2.3.3 Thermo-gravimetric Analysis (TGA)

Thermo-gravimetric Analysis (TGA) was used to determine the total metal loading of each catalyst. Figure 5-19 shows the weight profile over a temperature range for each of the catalysts. The drop in weight below 150°C can be attributed to the evaporation of absorbed water. In the range 150°C and 350°C there is a weight loss that was not observed for catalysts prepared via Method A. It is expected that this drop in weight is due to the removal of the surfactant HDA. From 350°C, the weight drop is due to the carbonation of the Vulcan (XC-72R). Additionally, Table 5-5 demonstrates that the metal loading of the catalysts is within a reasonable level of the expected values.

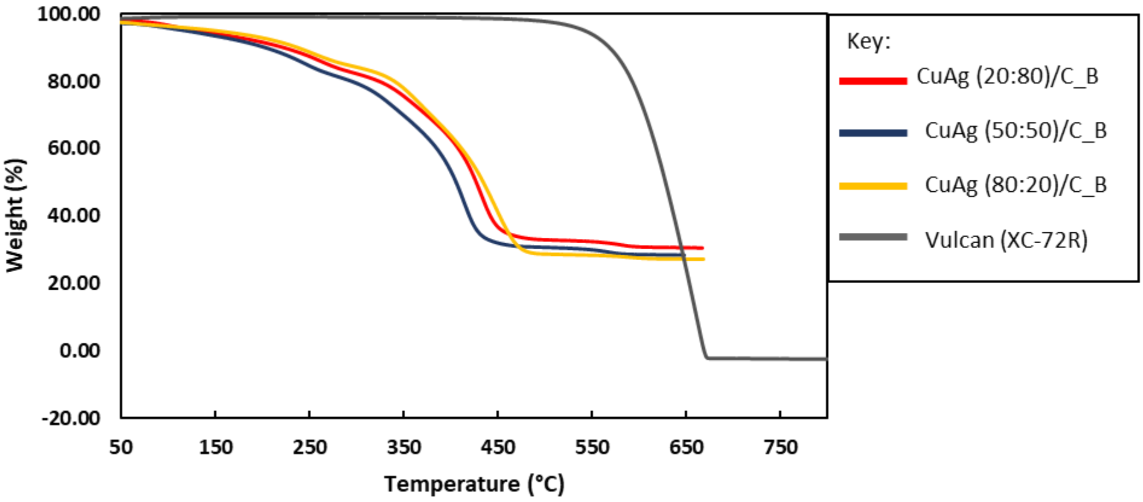

Figure 5-19: Thermogravimetric plots of nanoparticles supported on Vulcan XC-72R. Performed at a ramp rate of 5˚C/min in air which was fed at a rate of 10 ml/min.

Table 5-5: Expected and actual metal loading of bimetallic catalysts prepared via Method B. These were obtained from the TGA analysis.

Sample	Expected metal loading (wt%)	Actual Metal loading (wt%)
CuAg(20:80)/C_B	30.0	33.9
CuAg(50:50)/C_B	30.0	31.5
CuAg(80:20)/C_B	30.0	29.7

5.3 Development of batch reactor

The flow-cell design was adapted from studies by Geschiere (2014). The supported catalyst was sprayed onto a semi-permeable membrane, whereby the housing of the cell allows gas permeation while ensuring contact with the electrolyte. The gas products are identified through gas chromatography are the liquid products are identified through HPLC.

5.3.1 Improvement of cell design

Initially, a gas leakage test was performed. This was done by feeding the cell with nitrogen, while it was filled with 750 ml electrolyte. The flowrate of nitrogen at the inlet of the reactor was compared to the inlet of the GC using a flowmeter. The body of the cell was found to be airtight, however, it was observed that the working electrode of the cell was leaking, as shown in Figure 5-20 (a). After the addition of silicon carbide to the electrode housing, no leaks were observed (see Figure 5-20 (b)). This is since the silicon carbide ensured that the gas was dispersed along the gas diffusion electrode.

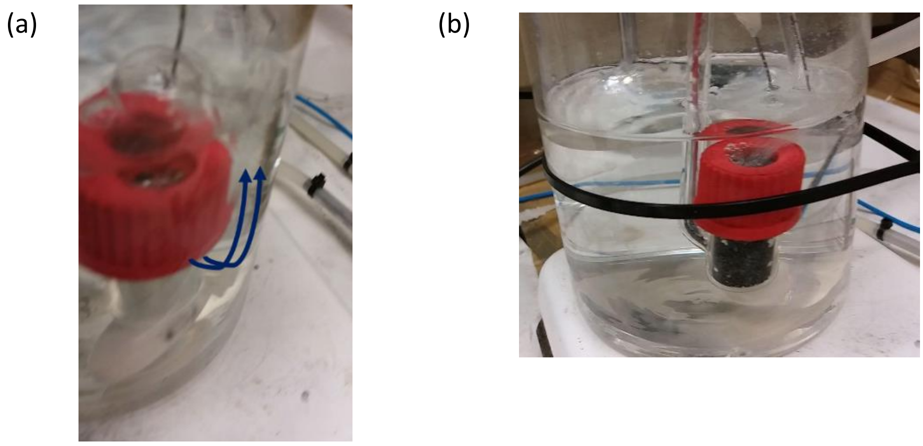

Figure 5-20: Illustration of electrode housing during cell leakage test. (a) Electrode chamber without the addition of silicon carbide (b) Electrode chamber with silicon carbide.

5.3.2 Initial catalytic evaluation

To ensure the functioning of the electrochemical cell, initial catalytic evaluation experiments were performed. Figure 5-21 indicates the cyclic voltammetry of the supported monometallic nanoparticles, compared to the GDE without any catalyst under CO_2RR conditions.

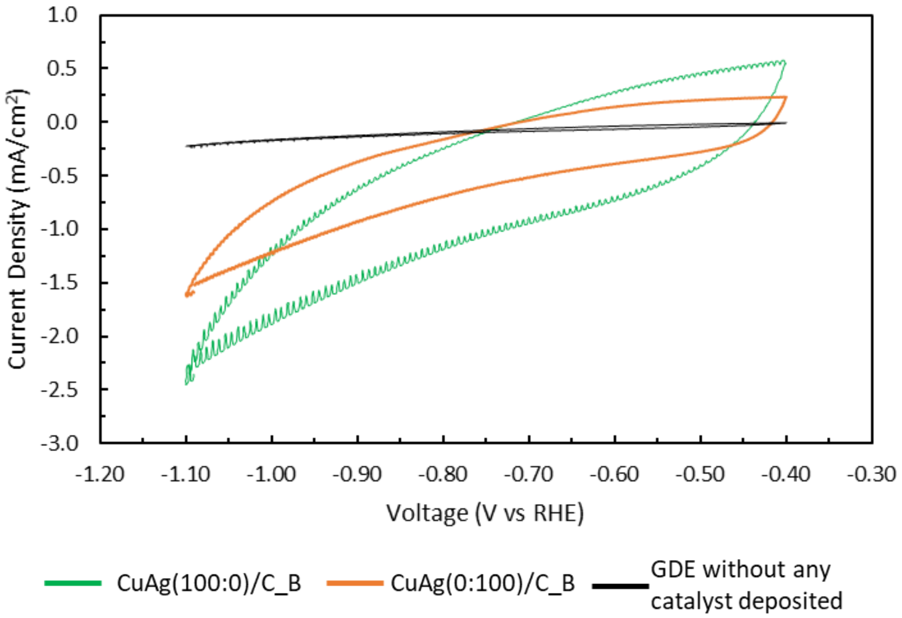

Figure 5-21: Cyclic voltammetry of monometallic catalysts and empty GDE under CO_2RR conditions. This was done in the range -0.4 and -1.10 V vs RHE, at a scan rate of 50 mV.s^{-1}.

It is clear from Figure 5-21 that the GDE without catalyst is not active for CO_2 reduction, as it has limited current density over the potential region. However, CuAg(1:0)/C_B and CuAg(0:1)/C_B are both active for CO_2 reduction, with the former having the highest activity.

To identify possible products formed under CO_2RR conditions, batch reduction experiments were performed, whereby the catalysts were held at a fixed potential over a 1h period. During this period, the gas outlet of the electrochemical cell was analysed via a GC-TCD, while the electrolyte was analysed for products via HPLC. It was established that no gas or liquid products could be detected for CuAg(1:0)/C_B and CuAg(0:1)/C_B, even though it has previously been shown that these two monometals do produce a significant amount of products under CO_2RR conditions (Hatsukade et al., 2014, Kuhl et al., 2014).

Therefore, it is then concluded that the current cell would be inappropriate for CO_2RR product detection. This is because of a low catalyst surface area to cell volume ratio, which can be improved by significantly reducing the reactor size.

5.4 Catalyst evaluation in RRDE setup

An RRDE was used to evaluate the electrocatalytic performance of the prepared catalysts. The RRDE has a glassy carbon disc where catalyst is deposited (see Section 4.7.1) and a Pt ring. In CO_2RR conditions, as reaction products are generated, the Pt ring is set at an oxidative potential to oxidise chemical products, which leads to their identification.

5.4.1 Electrochemical calibration of Pt ring electrode

To understand the response profile of CO_2RR products on the RRDE, Pt-ring calibration experiments were performed in CO_2 saturated 0.1M $NaHCO_3$ electrolyte. In these experiments, no catalyst was deposited on the glassy carbon disc of the RRDE. The Pt-ring potential was cycled between 0 and 1.3 V vs RHE. Reagent grade chemicals were introduced by bubbling or through dissolving in electrolyte. CO was bubbled through the electrolyte, while formate and methanol were introduced through electrolyte dissolution. Figure 5-22 shows the results of applying an oxidising potential on the Pt-ring when each of these possible CO_2RR products were introduced.

Figure 5-22 (a) shows the CV performed on CO_2 saturated 0.1M $NaHCO_3$ electrolyte. Typical Pt features relating to hydrogen adsorption and desorption were not observed. However, above 0.9 V Pt oxidation (Pt-O) is observed, with the reverse scan indicating the oxygen desorption from the platinum electrode (Zhang, Jiujun & Oloman, 2005). This reaction is shown in equation (5-1).

$$Pt + H_2O \rightarrow Pt - O + 2H^+ + 2e^- \qquad (5\text{-}1)$$

CO electrooxidation on Pt is generally accepted to follow a Langmuir-Hinshelwood process. Oxidation of CO at a low CO coverage occurs rapidly, while at a high coverage, CO oxidation is suppressed, thus showing that the reaction involves the use of adjacent Pt sites (Zhang, Jiujun, 2008). CO oxidation involves the formation of an OH species through water oxidation, and its reaction with CO to form CO_2 (Lai et al., 2007). A sharp CO peak is observed at a potential of 0.62 V vs RHE in Figure 5-22 (b). In the reverse scan, a reduction peak is observed at a potential of 0.21 V vs RHE, which is associated with Pt-O oxidation.

$$H_2O + * \rightarrow OH_{ads} + H^+ + e^- \qquad (5\text{-}2)$$

$$CO_{ads} + OH_{ads} \rightarrow COOH_{ads} \qquad (5\text{-}3)$$

$$COOH_{ads} \rightarrow CO_2 + H^+ + e^- + 2\,* \qquad (5\text{-}4)$$

The electrooxidation of formate can occur via two pathways. The first is a direct pathway through the hydrogenation of adsorbed formate ($HCOO_{ads}$), the second is an indirect pathway through CO_{ads} (She et al., 2014). Generally, the direct pathway is the most dominant.

$$HCOO_{ad} \rightarrow CO_2 + H^+ + e^- \tag{5-5}$$

$$HCOO_{ads} \rightarrow CO_{ads} + OH \rightarrow CO_2 + H^+ + e^- \tag{5-6}$$

Figure 5-22 (c) indicates that a formate oxidation peak occurs at a lower voltage than CO, at 0.35 V vs RHE. Additionally, a shoulder is observed at 0.9 V vs RHE. Increasing the concentration of formate has been shown to lead to a positive shift in the formate peak and an increase in current (Xu et al., 2013).

Methanol oxidation is shown in Figure 5-22 (c), where two peaks are observed in the forward scan, at 0.55 V and above 0.9V vs RHE and one peak in the reverse scan at 0.20 V vs RHE. In the forward scan, methanol is dehydrated on the Pt surface, forming adsorbed CO (Chung, Lee & Sung, 2016). The adsorbed CO is removed via its reaction with OH to form CO_2. As the potential increases, the coverage of adsorbed OH increases, limiting methanol oxidation (indicated at 0.7 V vs RHE). The potential increase further leads to the oxidation of Pt-OH_{ad} to Pt-O_x (Chung, Lee & Sung, 2016). The formation of the third peak, at 0.20 V vs RHE, on the reverse scan is unclear, with some researchers attributing this peak to the oxidation of carbon species (Mancharan & Goodenough, 1992). In contrast, other studies associate it with the reduction of PtO, which would lead to further oxidation of methanol (Hofstead-Duffy et al., 2012). However, it has been conclusively shown that since Pt-O reduction occurs at the same potential, the methanol oxidation peak in the reverse scan is only observed at high methanol concentrations (Seland, Tunold & Harrington, 2010).

$$CH_3OH + Pt \rightarrow Pt - CO_{ad} + 4H^+ + 4e^- \tag{5-7}$$

$$H_2O + Pt \rightarrow Pt - OH_{ads} + H^+ + e^- \tag{5-8}$$

$$Pt - CO_{ad} + Pt - OH_{ad} \rightarrow CO_2 + 2Pt + H^+ + e^- \tag{5-9}$$

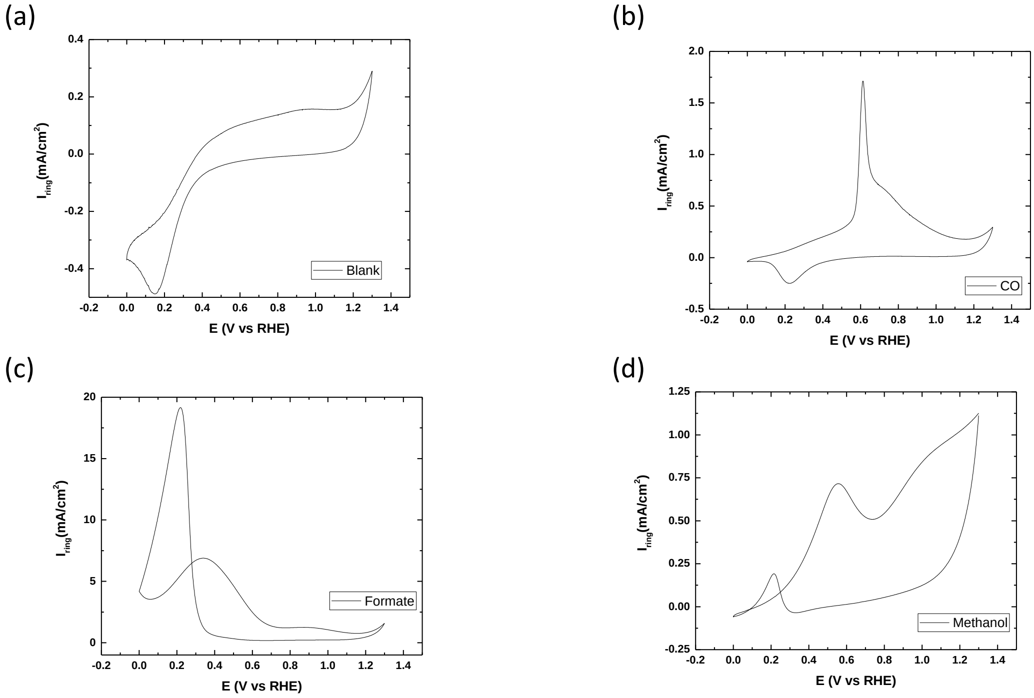

Figure 5-22: Pt-ring cyclic voltammetry scans for calibration of CO_2RR products in CO_2-saturated 0.1M $NaHCO_3$. Cyclic voltammetry scans were performed between 0 and 1.3V vs RHE, at a scan rate of 50 mV.s^{-1}, and rotation of 1500 rpm. (a) Blank cyclic voltammetry with no species added (b) Carbon monoxide (c) Potassium formate (d) Methanol.

It should be noted that the identification of chemical products through this method is limited to electroactive chemical species. Therefore, compounds such as methane and ethylene could not be identified directly.

5.4.1 Monometallic catalyst evaluation

5.4.1.1 Cyclic voltammetry of disc at fixed ring potential

Cyclic voltammetry experiments were performed under an Ar, and a CO_2 atmosphere for carbon supported Cu and Ag monometallic catalysts. The disc potential was scanned between 0 and -1.7 V vs RHE, while the Pt-ring electrode was held at 0.9 V vs RHE. This was done to determine the difference in activity under the two atmospheres, shown in Figure 5-23.

In an Ar atmosphere, only HER is expected to occur on the disc electrode, while in CO_2 conditions, the competing HER would occur alongside the CO_2RR (Zhu et al., 2018). Between 0 and -1 V vs RHE, the CuAg (0:100)/C_B has a comparable activity in both gaseous atmospheres. Above -1V vs RHE, the activity of CuAg (0:100)/C_B in a CO_2 saturated electrolyte increases sharper than in an Ar saturated electrolyte. In contrast, CuAg (100:0)/C_B does not display a significant difference in activity in the two electrolytes across the potential range. Figure 5-23 indicates that CuAg (100:0)/C_B is more active for CO_2 and hydrogen reduction than CuAg (0:100)/C_B, which is consistent with literature (Kuhl et al., 2014). Though the catalysts have the same metal loading (see section 5.2.1.3), CuAg (100:0)/C_B does have a significantly lower mean particle size relative to CuAg (0:100)/C_B, which would contribute to the higher catalyst activity.

(a) CuAg(100:0)/C_B in Ar (b) CuAg(100:0)/C_B in CO_2

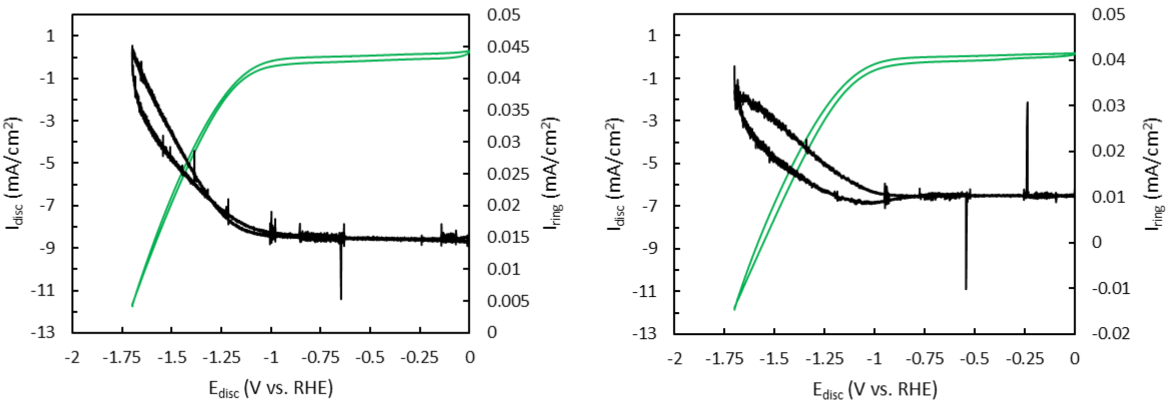

(c) CuAg(0:100)/C_B in Ar (d) CuAg(0:100)/C_B in CO_2

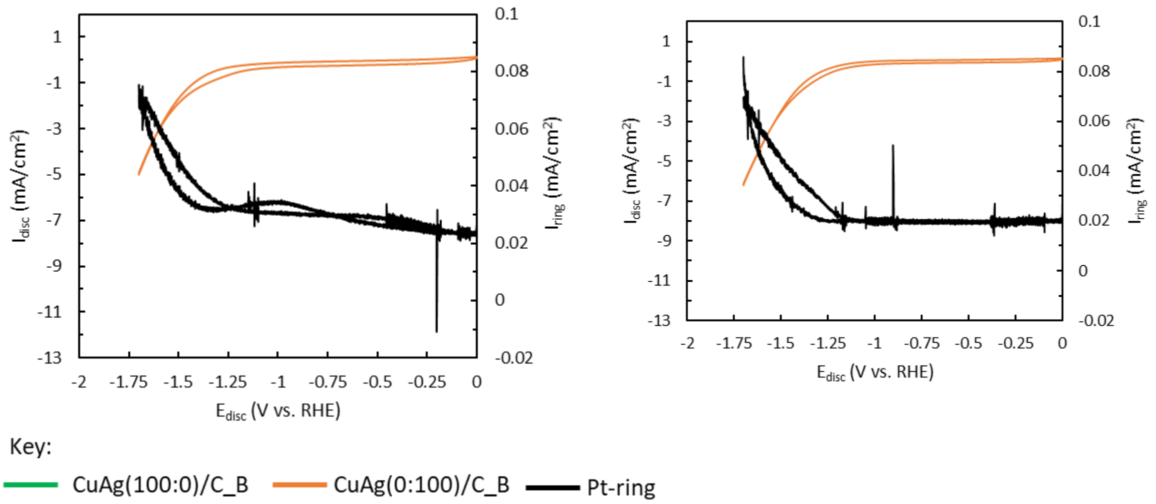

Figure 5-23: Cyclic voltammetry scans of the RRDE in Ar and CO_2 conditions. The disc electrode containing supported monometallic nanoparticles was cycled between 0 and -1.7 V vs RHE. The Pt-ring electrode was held at a potential of 0.9 V vs RHE. Scan rate: 100 mV.s^{-1}, constant rotating speed of 1500 rpm.

5.4.1.2 Cyclic voltammetry of ring at fixed disc potential

The monometallic catalysts are deposited on the RRDE disc. Figure 5-24 indicates cyclic voltammetry scans of the Pt-ring electrode, with fixed potentials at the disc electrode.

At a disc potential of -1.0 V vs RHE, CuAg(100:0)/C_B does not produce significant CO_2 reduction products, as it resembles a blank electrolyte scan (see Figure 5-22 (a)). However, at a fixed disc potential of -1.3V, two oxidative peaks can be observed at 0.3 V vs RHE and 1.0 V vs RHE, which resemble formate production (see Figure 5-22 (c)). The first oxidative peak increases with an increase in disc overpotential, up to -1.5 V vs RHE. This indicates a rise in formate yield. However, a further increase in overpotential up to -1.7V vs RHE leads to a decline in the peak current density. This decline cannot be regarded as catalyst deactivation as Figure 5-23 demonstrates that the activity at this potential rises. It is, however, as a result of an increase in the rate of the competing HER at higher overpotentials (Hori, Murata & Takahashi, 1989).

On the other hand, at a disc potential of -1.2 V vs RHE, CuAg(0:100)/C_B has an oxidative peak at 0.55 V vs RHE, which could be CO formation. An increase in overpotential leads to a rise in the current density of the main oxidative peak, implying an increased CO_2RR products yield. This oxidative peak broadens at highly negative disc potentials, and a significant negative shift in the oxidative peak is observed. This peak shifts from an oxidative potential of 0.58 to 0.38 V vs RHE, at disc potentials of -1.2 V vs RHE and -1.7 V vs RHE, respectively. This occurs due to a shift in product distribution, where at disc potentials of -1.2 V vs RHE, CO is the primary product. At highly negative disc potentials, formate begins to be produced, while CO formation is suppressed. A similar shift in product distribution with potential was observed when a Ag foil was used in the electrochemical reduction of CO_2 (Hatsukade et al., 2014).

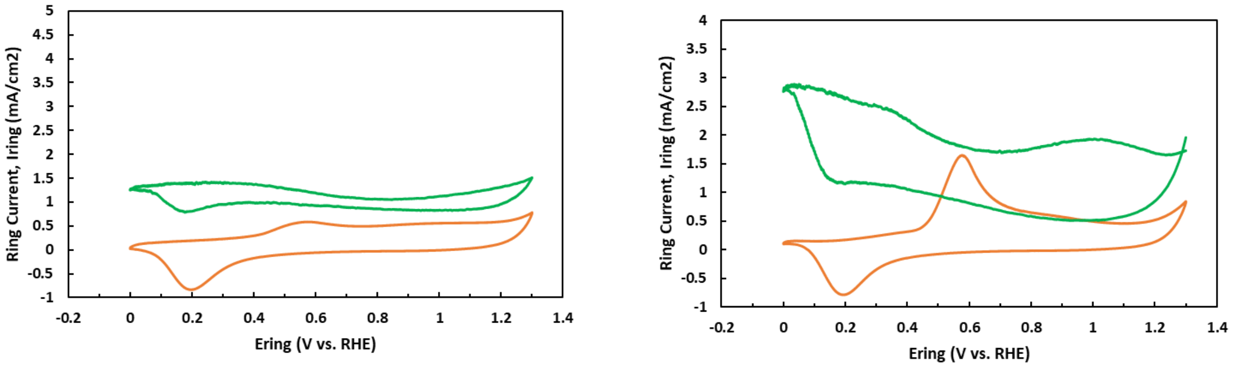
(a) Disc fixed at -1.2 V vs RHE

(b) Disc fixed at -1.3 V vs RHE

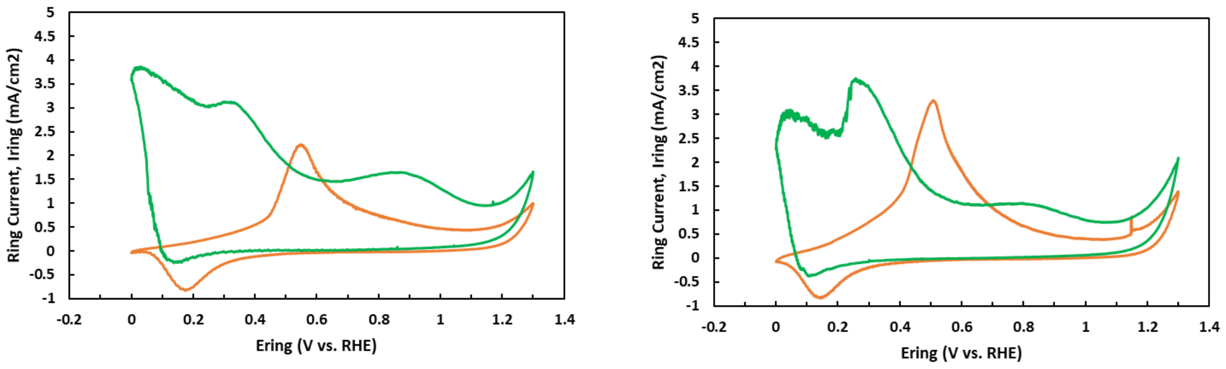
(c) Disc fixed at -1.4 V vs RHE

(d) Disc fixed at -1.5 V vs RHE

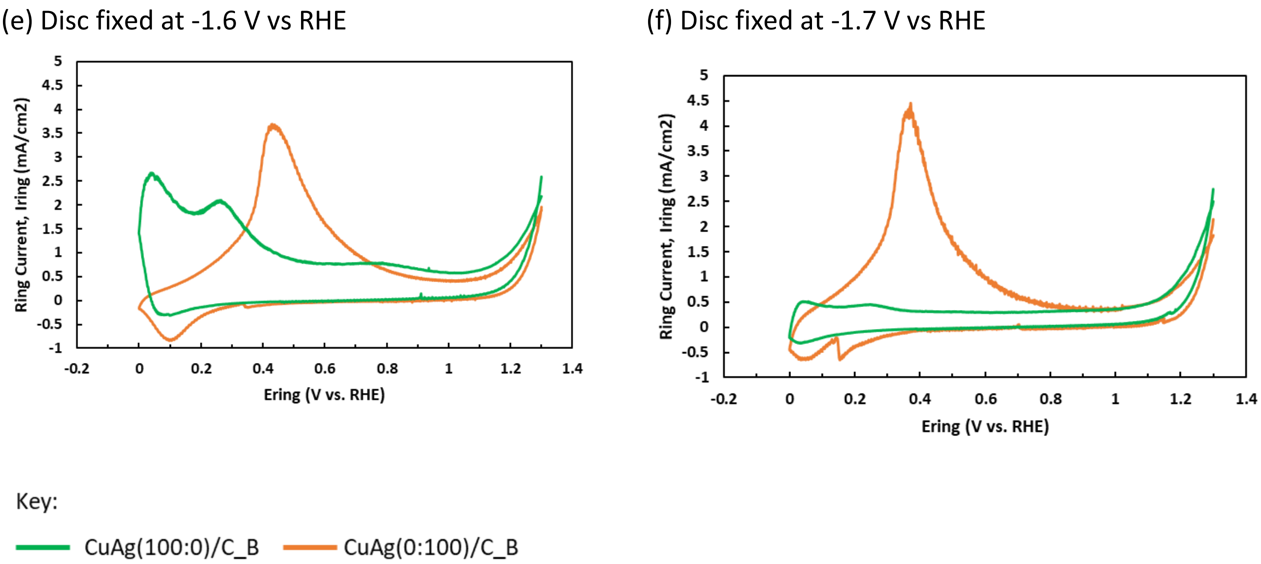
(e) Disc fixed at -1.6 V vs RHE

(f) Disc fixed at -1.7 V vs RHE

Figure 5-24: Cyclic voltammetry scans of the Pt-ring electrode, while holding the disc electrode at fixed potentials. Pt-ring scanned between 0 and 1.3 V vs RHE. Scan rate: 100 mV.s^{-1}, constant rotating speed of 1500 rpm. The disc has deposited monometallic catalysts, CuAg(100:0)/C_B and CuAg(0:100)/C_B.

5.4.2 Method A catalyst evaluation

5.4.2.1 Cyclic voltammetry of disc at fixed ring potential

The activity of supported bimetallic nanoparticles prepared via Method A was determined by taking cyclic voltammograms in an Ar, and CO_2 saturated electrolyte. This is shown in Figure 5-25.

In Ar conditions, the activity of the catalyst increases with rising catalyst Cu content, due to high Cu HER activity relative to Ag (Kuhl et al., 2014). In CO_2 conditions, the activity of CuAg(20:80)/C_A and CuAg(50:50)/C_A declines relative to Ar conditions, while CuAg(80:20)/C_A experiences a slight rise in activity. This decline in activity is potentially due to strong adsorption of CO_2RR intermediates which blocks catalyst sites (Dembinska et al., 2017, Hori, Murata & Takahashi, 1989).

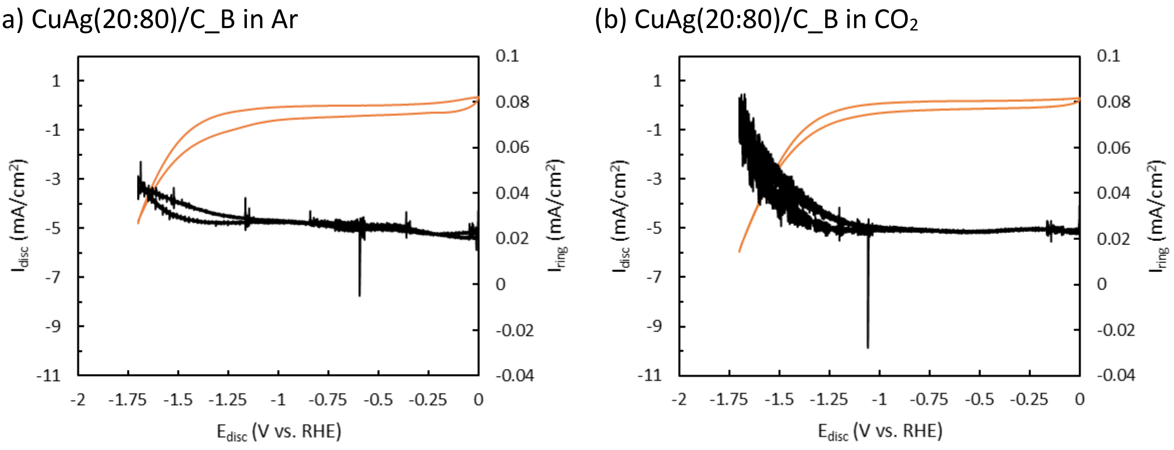
(a) CuAg(20:80)/C_B in Ar

(b) CuAg(20:80)/C_B in CO_2

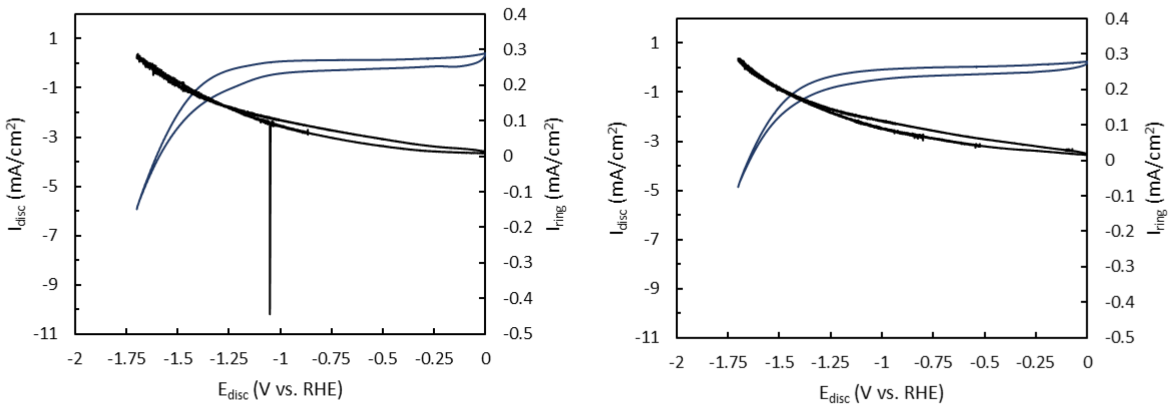
(c) CuAg(50:50)/C_B in Ar

(d) CuAg(50:50)/C_B in CO_2

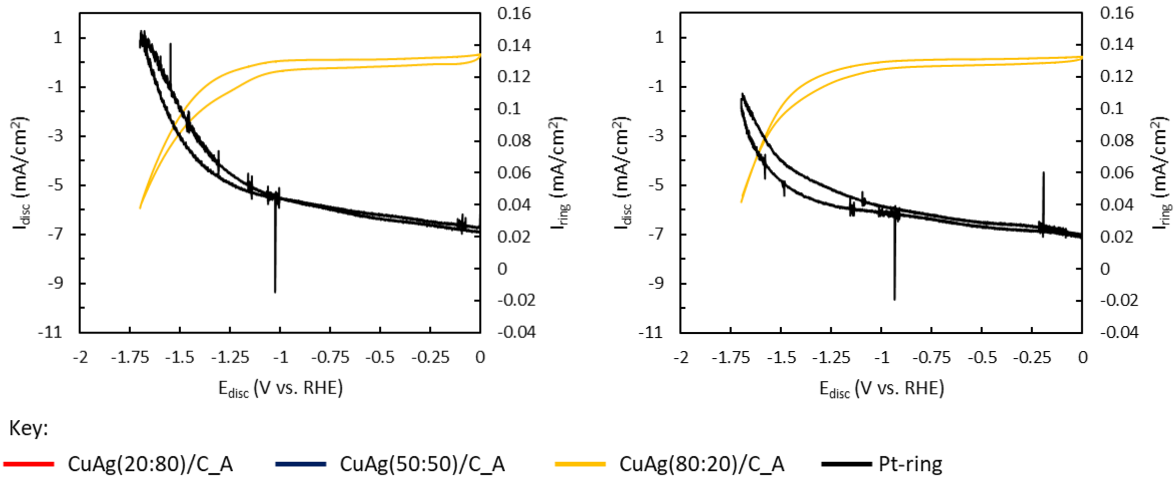
(e) CuAg(80:20)/C_B in Ar

(f) CuAg(80:20)/C_B in CO_2

Figure 5-25: Cyclic voltammetry scans of the RRDE in Ar and CO_2 conditions. The disc electrode containing supported CuAg bimetallic nanoparticles prepared via Method A was cycled between 0 and -1.7 V vs RHE. The Pt-ring electrode was held at a potential of 0.9 V vs RHE. Scan rate: 100 mV.s^{-1}, constant rotating speed of 1500 rpm.

5.4.2.2 Cyclic voltammetry of ring at fixed disc potential

The RRDE disc electrode was deposited with supported bimetallic nanoparticles prepared via Method A. Figure 5-26 shows the Pt-ring cyclic voltammetry, while the disc of the RRDE held at a fixed disc potential.

At the various disc potentials, CuAg(20:80)/C_A and CuAg(50:50)/C_A produce the same product – formate. An increase in disc overpotential correlates with an increase in peak current density, indicating an increase in formate yield. In contrast to the product distribution of monometallic Ag, Figure 5-26 indicates that the introduction of Cu shifts the product distribution away from CO formation towards the production of formate.

(a) Disc fixed at -1.2 V vs RHE

(b) Disc fixed at -1.3 V vs RHE

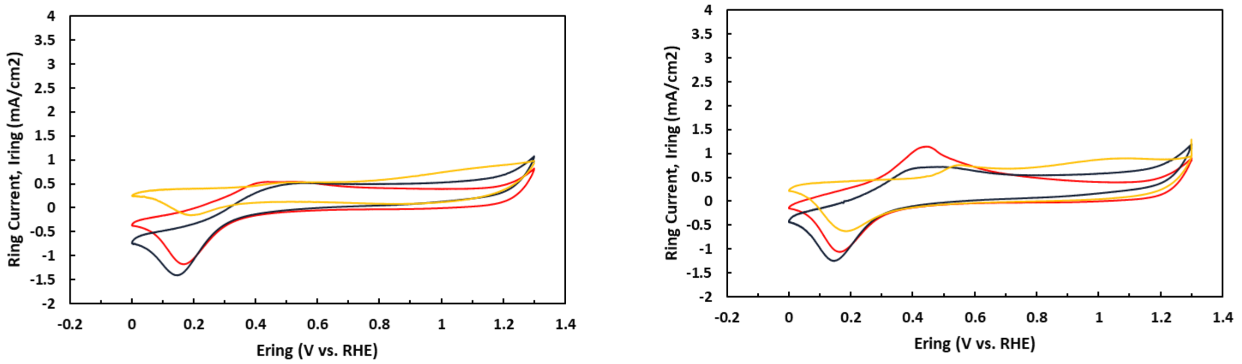

(c) Disc fixed at -1.4 V vs RHE

(d) Disc fixed at -1.5 V vs RHE

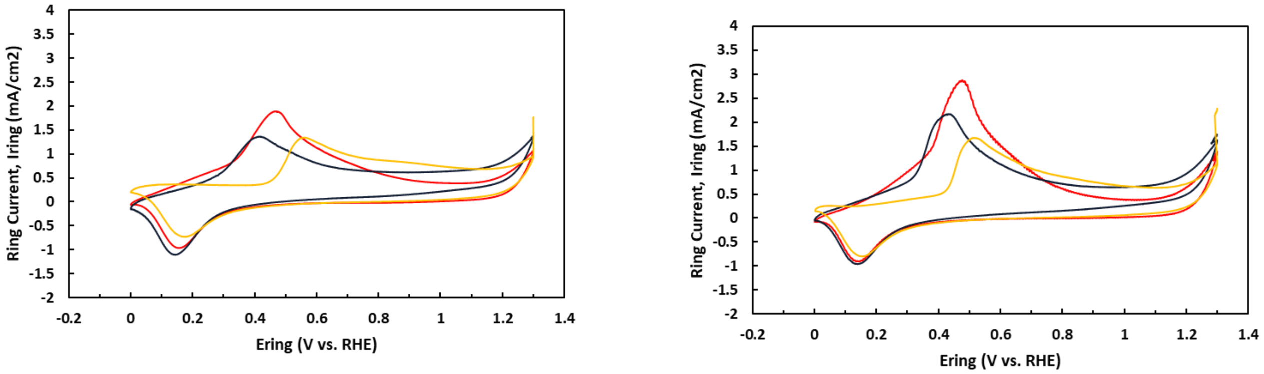

(e) Disc fixed at -1.6 V vs RHE

(f) Disc fixed at -1.7 V vs RHE

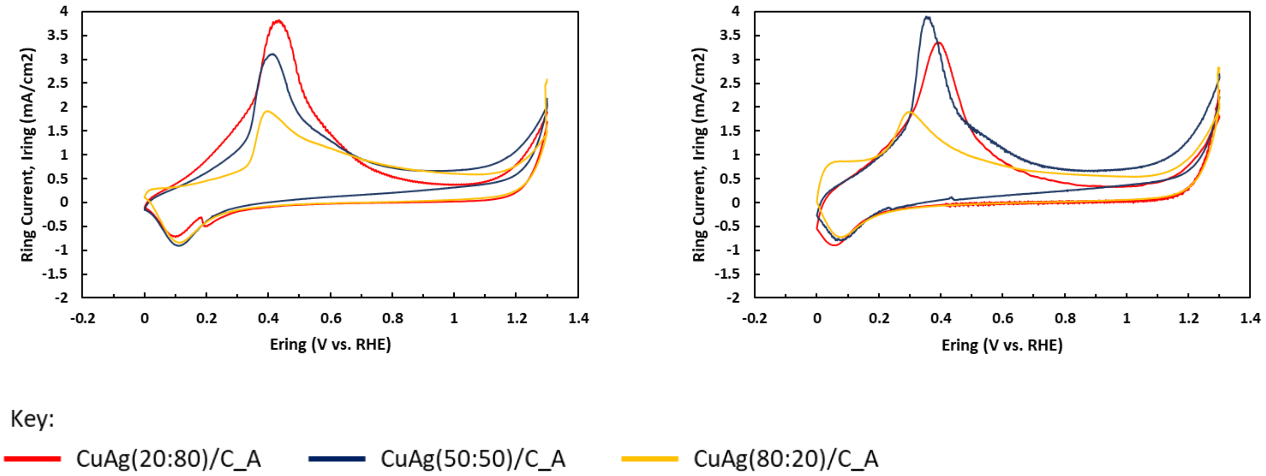

Figure 5-26: Cyclic voltammetry scans of the Pt-ring electrode, while holding the disc electrode at fixed potentials. Pt-ring scanned between 0 and 1.3 V vs RHE. Scan rate: 100 mV.s^{-1}, constant rotating speed of 1500 rpm. The disc has deposited bimetallic catalysts prepared via Method A.

At disc potentials of -1.2 V vs RHE and -1.3 V vs RHE, CuAg(80:20)/C_A predominantly produces methanol. At a potential of -1.4V vs RHE, the main peak shifts towards the production of CO. However, as the overpotential increases, the main peak shifts negatively, broadens, and its current density increases, signifying an increasing yield of formate. Figure 5-26 shows that electroactive products of monometallic CuAg(100:0)/C begin to decline with increasing overpotential due to increasing competing HER. This does show that the introduction of Ag to Cu via Method A has culminated in the limiting the HER at high overpotentials.

5.4.3 Method B catalyst evaluation

5.4.3.1 Cyclic voltammetry of disc at fixed ring potential

The activity of supported nanoparticles prepared via Method B was investigated. Figure 5-27 indicates the cyclic voltammetry of the disc electrode of the RRDE, with the Pt-ring potential held at a fixed potential of 0.9 V vs RHE.

In both Ar and CO_2 conditions, the activity of the catalyst increases with rising catalyst Cu content. However, relative to Ar conditions, the activity of the catalysts decline in CO_2RR conditions, with this decline in activity being significant for CuAg(50:50)/C_B. In Ar conditions the HER reaction is expected to occur, while in CO_2 conditions, both the CO_2RR and the HER is expected to occur. The decline in current density in CO_2RR conditions is due to the introduction of inhibiting CO_2RR adsorbates, which limits catalyst active sites (Dembinska et al., 2017, Hori, Murata & Takahashi, 1989).

Figure 5-27 shows that in CO_2RR conditions, the activity of the catalyst rises with an increase in its Cu content. There are multiple contributing factors to this difference in activity. Though the three catalysts have a similar metal loading (see 5.2.3.3), section 5.2.3.1 shows that mean nanoparticle size of the final catalyst decreases with increasing Cu content, thus the CuAg(80:20)/C_B catalyst has the smallest mean particle size. The low mean particle size increases the available surface area for reaction. Additionally, it has been shown in literature that in CO_2RR conditions, Cu has higher activity Ag (Kuhl et al., 2014).

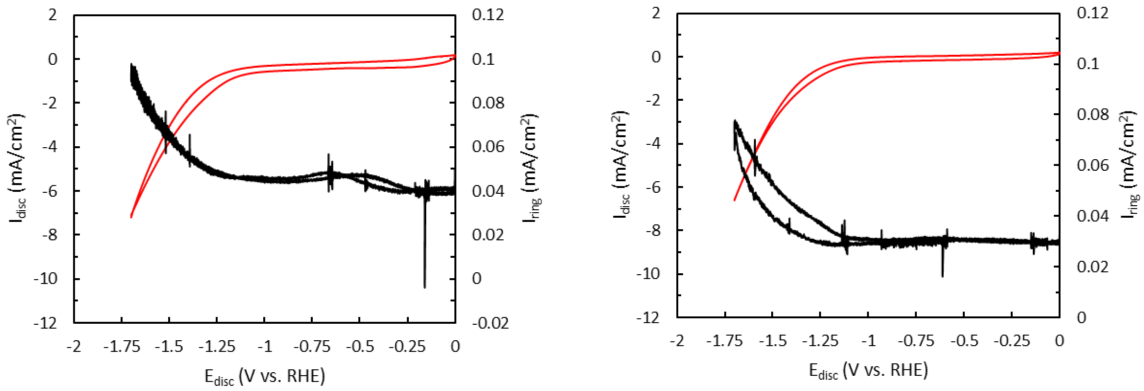

(a) CuAg(20:80)/C_B in Ar

(b) CuAg(20:80)/C_B in CO_2

(c) CuAg(50:50)/C_B in Ar

(d) CuAg(50:50)/C_B in CO_2

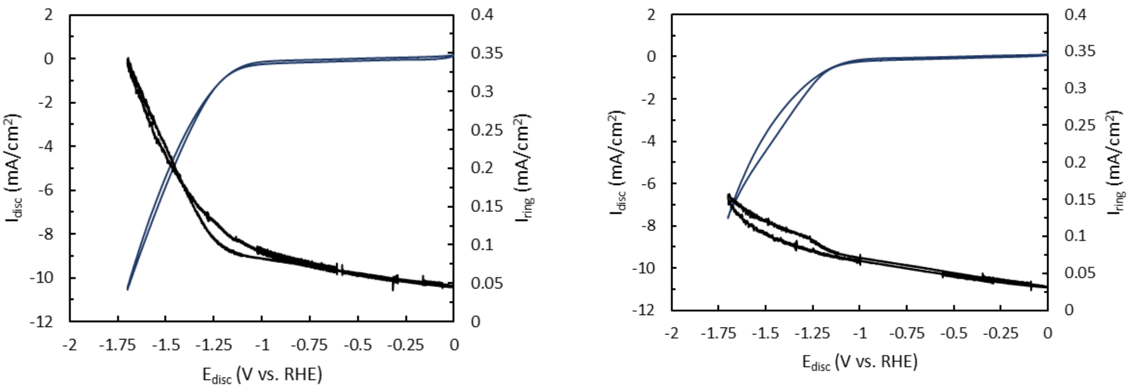

(e) CuAg(80:20)/C_B in Ar

(f) CuAg(80:20)/C_B in CO_2

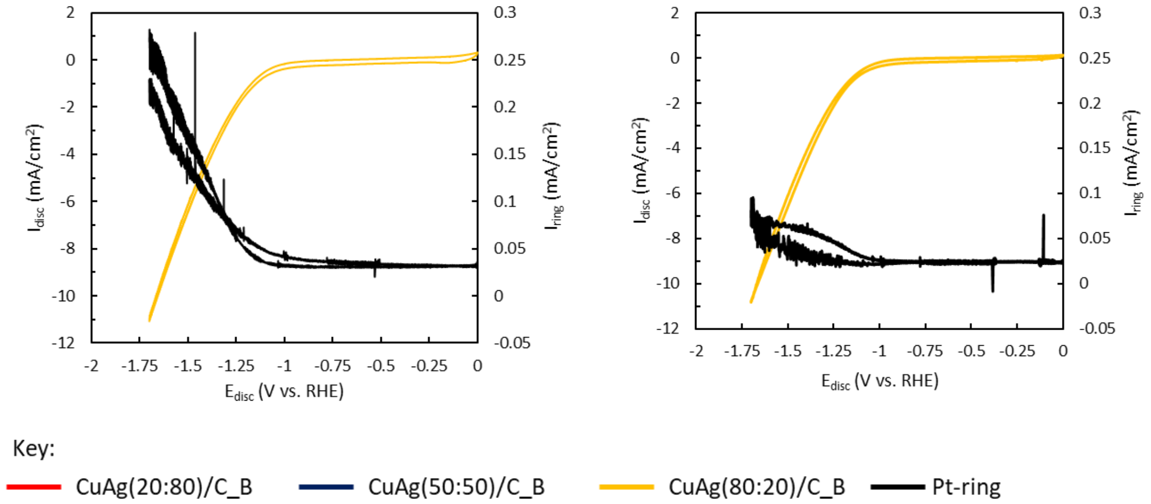

Figure 5-27: Cyclic voltammetry scans of the RRDE in Ar and CO_2 conditions. The disc electrode containing supported CuAg bimetallic nanoparticles prepared via Method B was cycled between 0 and -1.7 V vs RHE. The Pt-ring electrode was held at a potential of 0.9 V vs RHE. Scan rate: 100 mV.s^{-1}, constant rotating speed of 1500 rpm.

5.4.3.2 Cyclic voltammetry of ring at fixed disc potential

Figure 5-28 shows the cyclic voltammetry experiments of the Pt-ring of the RRDE while holding the disc at several fixed potentials. The peaks of all catalyst samples shift negatively with an increase in overpotential. For catalysts with a high Cu composition, the peak position is at a lower oxidising potential, across all disc potentials. This signifies that the CuAg catalysts have distinct product distributions.

(a) Disc fixed at -1.2 V vs RHE (b) Disc fixed at -1.3 V vs RHE

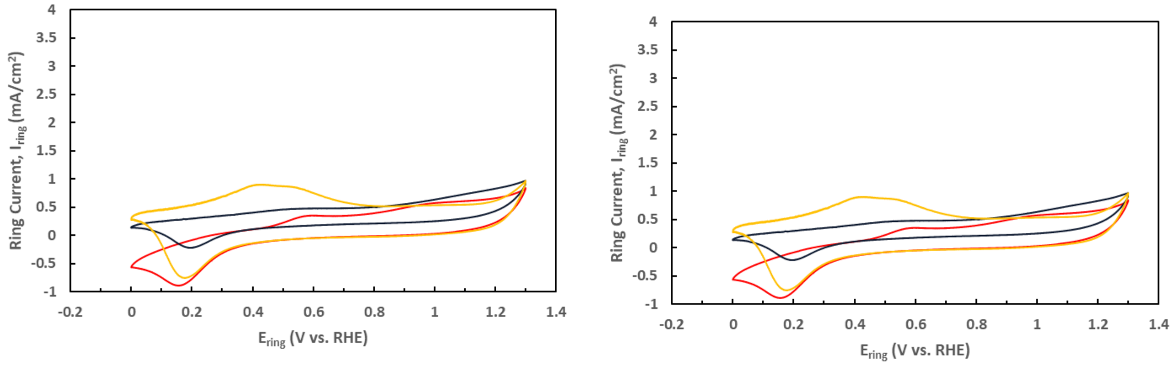

(c) Disc fixed at -1.4 V vs RHE (d) Disc fixed at -1.5 V vs RHE

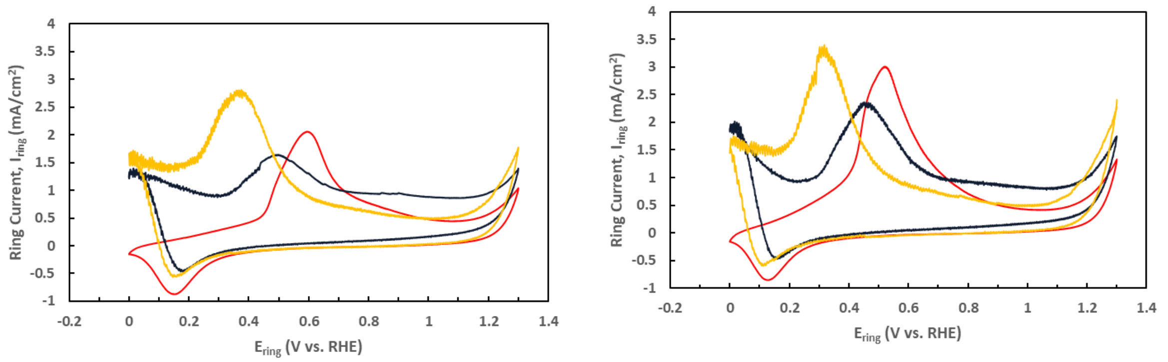

(e) Disc fixed at -1.6 V vs RHE (f) Disc fixed at -1.7 V vs RHE

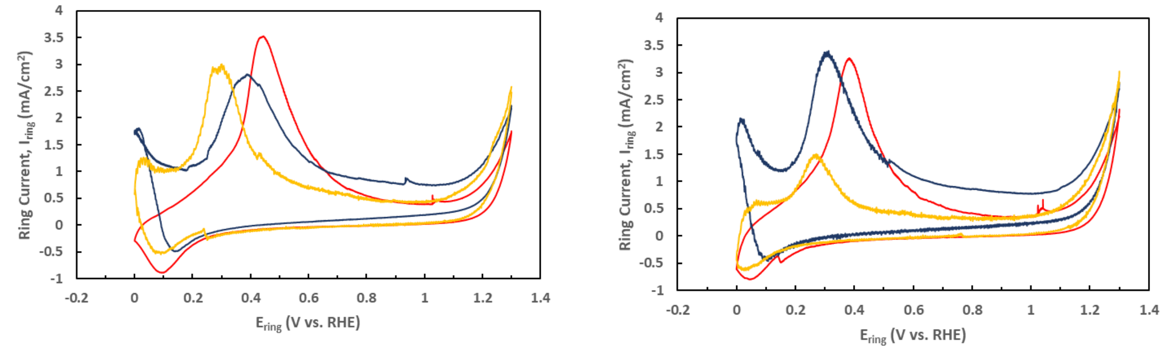

Key:

🟥 CuAg(20:80)/C_B 🟦 CuAg(50:50)/C_B 🟨 CuAg(80:20)/C_B

Figure 5-28: Cyclic voltammetry scans of the Pt-ring electrode, while holding the disc electrode at fixed potentials. Pt-ring scanned between 0 and 1.3 V vs RHE. Scan rate: 100 mV.s^{-1}, constant rotating speed of 1500 rpm. The disc has deposited bimetallic catalysts prepared via Method B.

At a potential of -1.2V vs RHE, CuAg(20:80)/C_B produces predominantly CO. Similar to observations for CuAg(0:100)/C (see section 5.4.1.2), the product distribution in CuAg(20:80)/C_B shifts towards a high formate yield with an increase in overpotential. The sample CuAg(50:50)/C_B produces methanol at a potential of -1.2V vs RHE. As the disc overpotential rises, this shifts towards the production of formate.

Initially, at a disc potential of -1.2 V vs RHE, the peak of CuAg(80:20)/C_B is broad, indicating possible production of formate, some methanol and carbon monoxide. As the overpotential increases, this peak is sharper, shifts negatively, and begins to resemble that of CuAg(100:0)/C_B at the same potentials. This is because of a shift in product distribution, culminating in higher formate yield. At a potential of -1.7 V vs RHE, the peak current density reduces significantly, perhaps due to the increased competing HER at such high overpotentials. This observation is similar to the one observed in CuAg(100:0)/C_B.

5.5 Comparison of catalytic performance of Method A and Method B

Bimetallic nanoparticles were synthesised via two methods: Method A (in the absence of HDA), and Method B (in the presence of HDA). Method B produced bimetallic nanoparticles with a larger mean particle size and a wider particle size distribution relative to Method A. It was further concluded that Method B produced a CuAg solid solution, while Method A produced particles that had a phase separated structure.

Based on electrocatalytic evaluation, the proposed CO_2RR reaction mechanism was adapted from Hatsukade et al. (2014), as shown in Figure 5-29. It should be noted that this mechanism is based on CO_2RR electroactive products, as these could be analysed through the RRDE. The proposed reaction mechanism indicates two routes towards formate production. The first is through the adsorption of CO_2 to form the OCHO* intermediate, which occurs through the stabilisation of the intermediate's oxygen bonds. The second is via the formation of COOH*, whereupon proton and electron transfer, formate can be produced. Upon further reduction of the COOH* intermediate, CO is formed, which can either desorb as a final product or undergo further reduction to methanol.

The catalytic evaluation experiments are consistent with this mechanism. Throughout the evaluated potential range, CuAg(100:0)/C_B predominantly produces formate. This is due to Cu's high oxygen affinity (Peterson & Nørskov, 2012), hence CuAg(100:0)/C_B stabilises the OCHO* intermediate's oxygen atom to form formate through route 2a (see Figure 5-29). However, it should be noted that at a disc potential of -1.7 V vs RHE, the CO_2RR activity of CuAg(100:0)/C_B declines due to the rise in the HER. In comparison, the formation of CO_2RR products for the monometallic CuAg(0:100)/C_B catalyst will progress via route 1b, as it has a weak oxygen affinity (Peterson & Nørskov, 2012). At low overpotentials, Figure 5-24 demonstrates that CuAg(0:100)/C_B primarily produces CO via route 2c, while at high overpotentials formate production via route 2b is favoured. Through DFT study, Cheng, Xiao & Goddard (2016) have shown that route 2c is favoured at low overpotentials as it has a lower activation energy, while the onset production of $HCOO^-$ through route 2c, occurs at higher overpotentials because of its higher activation energy.

CuAg(20:80)/C_A and CuAg(50:50)/C_A phase separated bimetallic nanoparticles produce primarily formate over the evaluated potential range. This since the addition of Cu to Ag for this synthesis route increases the stability of the OCHO* due to Cu's high oxygen affinity, hence formate is produced via route 2a. However, the production distribution of CuAg(80:20)/C_A shifts from methanol to formate as overpotential rises. It should also be noted that in contrast to CuAg(100:0)/C_B, the product yield from CO_2RR CuAg(80:20)/C_A does not decline at a potential of -1.7V vs RHE. This indicates that the addition of Ag to Cu limits the HER.

The catalytic evaluation of bimetallic catalysts produced via Method B demonstrates that the catalysts behave as monometallic catalysts, with limited synergistic properties. This is since CuAg(20:80)/C_B and CuAg(80:20)/C_B have similar product distributions to CuAg(0:80)/C_B and CuAg(100:0)/C_B, respectively. In addition to this, the product distribution of CuAg(50:50)/C_B is almost a superimposition of the product distribution of the two monometals.

The catalytic evaluation has demonstrated that the synthesis method of the CuAg bimetallic nanoparticles has a strong influence on the catalyst's activity and product distribution. This is because of their different atomic arrangements which influence the stability of certain CO_2RR intermediates.

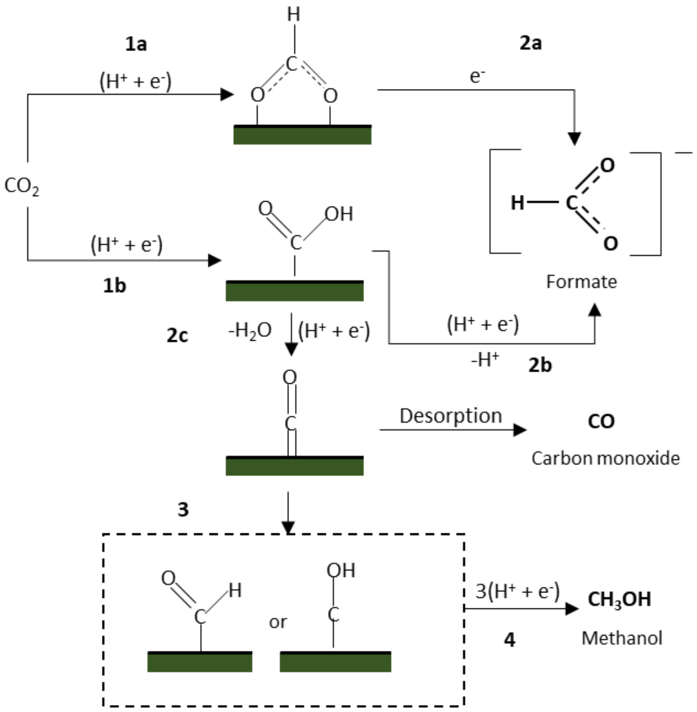

Figure 5-29: Proposed mechanism, adapted from Hatsukade et al. (2014).

6 Conclusion

This study investigated the conditions for the synthesis of supported CuAg bimetallic nanoparticles, by exploring synthesis temperature, total metal concentration, and washing procedure. It was found that at a total metal concentration of 3.5 mM, a rise in the synthesis temperature to 50 °C increases the extent of nanoparticle agglomeration. Additionally, it was found that nanoparticle supporting prior to washing was effective in reducing the extent of nanoparticle agglomeration.

The addition of Ag to Cu limited the extent of Cu oxidation. Synthesised monometallic Cu was oxidised to Cu_2O, however, bulk Cu oxidation was not observed via XRD for CuAg bimetallic nanoparticles. This is because of possible electron transfer from Cu to Ag, due to Ag having a higher electron affinity. This culminates in Cu electrons being unavailable to form bonds with oxygen.

Hexadecylamine (HDA) has an influence on the morphology of CuAg nanoparticles as well as the extent of alloying. CuAg bimetallic nanoparticles prepared without HDA formed phase-separated bimetallic nanoparticles. On the other hand, the introduction of HDA at a total metal precursor to HDA molar ratio of 1:2.5 culminated in an increase in the average nanoparticle size relative to when the synthesis was performed in the absence of HDA. Additionally, CuAg bimetallic nanoparticles synthesised in the presence of HDA formed a metallic solid solution.

The current design of the batch reactor was found to be limiting in the identification of CO_2RR chemical products. This is because of its large volume relative to the electrode surface area, which leads to the dilution of liquid products that are formed. On the other hand, employing the RRDE allowed for the electrocatalytic performance evaluation of each catalyst, as well as the identification of electroactive CO_2RR products.

By employing the RRDE, it was found that Cu and Ag form distinct products. The Cu monometallic catalyst was found to have a higher CO_2RR activity than Ag. In the range of the overpotential studied, monometallic Cu forms predominantly formate, while Ag forms CO at low overpotentials and the product distribution shifts to formate production at higher overpotentials. These observations are consistent with existing body of literature (Hatsukade et al., 2014, Kuhl et al., 2014).

The RRDE study demonstrated that the product distribution agreed with the CO_2RR mechanism proposed by Hatsukade et al. (2014). CuAg(20:80)/C_A and CuAg(50:50)/C_A synthesised without HDA formed the same product – formate – at all product distributions. This is since the addition of Cu to Ag stabilises the formate intermediate through Cu bond formation with oxygen. At low overpotentials, CuAg(80:20)/C_A forms methanol, however, this shifts towards formate at higher overpotentials. On the other hand, nanoparticles prepared in the presence of HDA displayed a different product distribution than those prepared in its absence. As the Cu content of the catalyst increased, the product distribution shifted from CO production to methanol, and then finally formate.

This study has developed a method towards the synthesis of monodisperse bimetallic CuAg nanoparticles. Additionally, it has demonstrated that the CuAg bimetallic ratio, as well as the catalyst atomic arrangement strongly influence the activity of the catalyst, as well as the resulting CO_2RR product distribution.

7 Recommendations

The suggested future work from this study is as follows.

7.1 Nanoparticle synthesis and characterisation

These recommendations are with regards to the improvement of nanoparticle synthesis.

- Characterise the produced mono and bimetallic nanoparticles from the two synthesis methods using X-ray Photoelectron Spectroscopy, to understand the metallic surface concentration, as well as the extent of surface Cu oxidation.
- Perform a nanoparticle growth series for all bimetallic nanoparticle ratios, so as to understand the growth mechanism. This can be achieved by taking TEM samples over the nanoparticles synthesis period for different CuAg ratios, rather than at a fixed CuAg ratio. This will assist in unpacking the formation mechanism followed by CuAg nanoparticles.
- Make use of a syringe in which the rate of reducing agent addition can be controlled. This is since it has been shown that the particle size distribution is largely influenced by the rate of reducing agent injection (Dongjo, Sunho & Jooho, 2006).
- Explore the synthesis of CuAg nanoparticles at higher temperatures in various organic solvents as this can improve the extent of alloying.
- Investigate the utilisation of high concentrations of HDA in the synthesis of CuAg nanoparticles to improve nanoparticle capping (Ahn, Abu-Baker & Palmore, 2017).

7.2 Electrochemical batch reactor evaluation

- Increase the gas diffusion electrode area to electrolyte volume ratio, which would allow the detection of liquid products. This can be achieved by increasing the electrode surface area or reducing the cell volume. For the current cell design, it would be more practical to reduce the cell volume.
- Reduce the piping distance between the cell and the GC which would reduce piping dead volume, therefore preventing the dilution of CO_2RR products.
- The role of copper oxide on the electrochemical reduction of carbon dioxide requires investigation. Analysis of the transformation between Cu_xO and Cu^0 during electrochemical reduction requires investigation to decouple the role of oxides on electron transfer during electrochemical reduction of CO_2 (Kas et al., 2014). A proposal here is that Cu^{2+} is reduced to Cu^{+1}, which is then further reduced to Cu^0. The last reaction may facilitate the transfer of electrons to Cu.

7.3 Rotating ring disc electrode

- When performing initial CVs on the disc containing catalysts, the ring potential should be held at the various oxidation peak potentials identified for each of the CO_2RR products. These experiments will give a preliminary indication of the disc potentials in which certain CO_2RR products most likely form.
- Conduct batch reduction experiments at fixed potentials to study the liquid products that form for each catalyst. To enable product detection, these experiments will need to be performed at low reactor volumes.

8 Appendices

8.1 Effect of storage on bimetallic nanoparticles

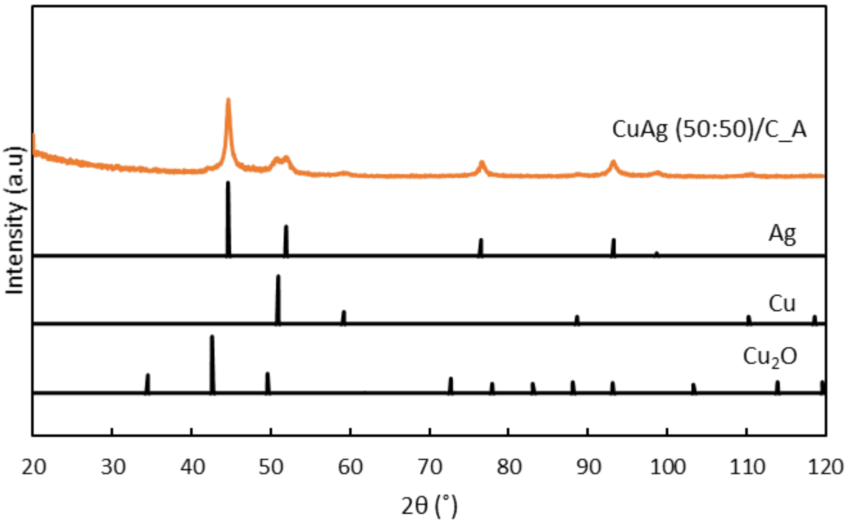

Figure 8-1: CuAg (50:50)/C_A nanoparticles after storage for 3 months.

8.2 GC TCD calibration

Table 8-1: GC-TCD calibration data and response factors

Gas Component, i	**N_2**	**H_2**	**CO_2**	**CH_4**	**CO**	**Ar**
Volume %	5.8	39.8	10.1	15.9	18.5	9.9
Average area of 5 peaks	354	21651	889	3730	1121	-
Response Factor (R_i)	1.000	0.112	0.694	0.260	1.007	-

9 List of references

Abid, J.P., Wark, A.W., Brevet, P.F. & Girault, H.H. 2002. Preparation of silver nanoparticles in solution from a silver salt by laser irradiation. *Chemical Communications.* (7):792-793. DOI:https://doi.org/10.1039/B200272H.

Ahn, S.T., Abu-Baker, I. & Palmore, G.T.R. 2017. Electroreduction of CO2 on polycrystalline copper: Effect of temperature on product selectivity. *Catalysis Today.* 288:24-29. DOI:https://doi.org/10.1016/j.cattod.2016.09.028.

Ali, Z.I., Ghazy, O.A., Meligi, G., Saleh, H.H. & Bekhit, M. 2018. Copper Nanoparticles: Synthesis, Characterization and Its Application as Catalyst for p-Nitrophenol Reduction. *Journal of Inorganic and Organometallic Polymers and Materials.* DOI:10.1007/s10904-018-0780-4.

Balkan, T., Küçükkeçeci, H., Zarenezhad, H., Kaya, S. & Metin, Ö. 2020. One-pot synthesis of monodisperse copper–silver alloy nanoparticles and their composition-dependent electrocatalytic activity for oxygen reduction reaction. *Journal of Alloys and Compounds.* 831:154787. DOI:https://doi.org/10.1016/j.jallcom.2020.154787.

Bandyopadhyay, S. & Chakravorty, D. 2011. Preparation of nanocrystalline copper by electrodeposition. *Journal of Materials Research.* 12(10):2719-2724. DOI:https://doi.org/10.1557/JMR.1997.0362.

Belloni, J., Mostafavi, M., Remita, H., Marignier, J.-L. & Marie-Odile Delcourt, a. 1998. Radiation-induced synthesis of mono- and multi-metallic clusters and nanocolloids. *New Journal of Chemistry.* 22(11):1239-1255. DOI:https://doi.org/10.1039/A801445K.

Brooks, K.P., Hu, J., Zhu, H. & Kee, R.J. 2007. Methanation of carbon dioxide by hydrogen reduction using the Sabatier process in microchannel reactors. *Chemical Engineering Science.* 62(4):1161-1170. DOI:https://doi.org/10.1016/j.ces.2006.11.020.

Chen, A. & Holt-Hindle, P. 2010. Platinum-Based Nanostructured Materials: Synthesis, Properties, and Applications. *Chemical Reviews.* 110(6):3767-3804. DOI:https://doi.org/10.1021/cr9003902.

Cheng, T., Xiao, H. & Goddard, W.A. 2016. Reaction Mechanisms for the Electrochemical Reduction of CO2 to CO and Formate on the Cu(100) Surface at 298 K from Quantum Mechanics Free Energy Calculations with Explicit Water. *Journal of the American Chemical Society.* 138(42):13802-13805. DOI:10.1021/jacs.6b08534.

Chung, D.Y., Lee, K.-J. & Sung, Y.-E. 2016. Methanol Electro-Oxidation on the Pt Surface: Revisiting the Cyclic Voltammetry Interpretation. *The Journal of Physical Chemistry C.* 120(17):9028-9035. DOI:https://doi.org/10.1021/acs.jpcc.5b12303.

Das, A., Chadha, R., Maiti, N. & Kapoor, S. 2014. Role of Surfactant in the Formation of Gold Nanoparticles in Aqueous Medium. *Journal of Nanoparticles.* 2014:916429. DOI:https://doi.org/10.1155/2014/916429.

Dembinska, B., Kiciński, W., Januszewska, A., Dobrzeniecka, A. & Kulesza, P.J. 2017. Carbon Dioxide Electroreduction at Highly Porous Nitrogen and Sulfur Co-Doped Iron-Containing Heterogeneous

Carbon Gel. *Journal of The Electrochemical Society.* 164(7):H484-H490. DOI:https://doi.org/10.1149/2.0721707jes.

Deo Malviya, K., Srivastava, C. & Chattopadhyay, K. 2017. Phase formation and stability of Ag–60 at%Cu alloy nanoparticles synthesized by chemical routes in aqueous media. *Physical Chemistry Chemical Physics.* 19(41):28006-28013. DOI:https://doi.org/10.1039/C7CP05738E.

Dohyung, K., Resasco, J., Yu, Y., Asiri, A.M. & Yang, P. 2014. Synergistic geometric and electronic effects for electrochemical reduction of carbon dioxide using gold–copper bimetallic nanoparticles. *Nature Communications.* 5(1):4948. DOI:https://doi.org/10.1038/ncomms5948.

Dongjo, K., Sunho, J. & Jooho, M. 2006. Synthesis of silver nanoparticles using the polyol process and the influence of precursor injection. *Nanotechnology.* 17(16):4019. Available: http://stacks.iop.org/0957-4484/17/i=16/a=004.

Feaster, J.T., Jongerius, A.L., Liu, X., Urushihara, M., Nitopi, S., Hahn, C., Chan, K., Norskov, J. et al. 2017. Understanding the Influence of [EMIM]Cl on the Suppression of the Hydrogen Evolution Reaction on Transition Metal Electrodes. *American Chemical Society.* 33:9464-9471.

Ferrando, R., Jellinek, J. & Johnston, R.L. 2008. Nanoalloys: From Theory to Applications of Alloy Clusters and Nanoparticles. *Chemical Reviews.* 108(3):845-910. DOI:https://doi.org/10.1021/cr040090g.

Garza, A.J., Bell, A.T. & Head-Gordon, M. 2018. Mechanism of CO2 Reduction at Copper Surfaces: Pathways to C2 Products. *ACS Catalysis.* 8(2):1490-1499. DOI:https://doi.org/10.1021/acscatal.7b03477.

Geschiere, S.D. 2014. Electrocatalytic reduction of carbon dioxide on copper-gold nanoparticles. Tu Delft.

Gommes, C.J. 2019. Ostwald ripening of confined nanoparticles: chemomechanical coupling in nanopores. *Nanoscale.* 11(15):7386-7393. DOI:https://doi.org/10.1039/C9NR01349K.

Goodpaster, J.D., Bell, A.T. & Head-Gordon, M. 2016. Identification of Possible Pathways for C–C Bond Formation during Electrochemical Reduction of CO2: New Theoretical Insights from an Improved Electrochemical Model. *The Journal of Physical Chemistry Letters.* 7(8):1471-1477. DOI:https://doi.org/10.1021/acs.jpclett.6b00358.

Guerra, L., Rossi, S., Rodrigues, J., Gomes, J., Puna, J. & Santos, M.T. 2018. Methane production by a combined Sabatier reaction/water electrolysis process. *Journal of Environmental Chemical Engineering.* 6(1):671-676. DOI:https://doi.org/10.1016/j.jece.2017.12.066.

Hatsukade, T., Kuhl, K.P., Cave, E.R., Abram, D.N. & Jaramillo, T.F. 2014. Insights into the electrocatalytic reduction of CO2 on metallic silver surfaces. *Physical Chemistry Chemical Physics.* 16(27):13814-13819. DOI:https://doi.org/10.1039/C4CP00692E.

Hofstead-Duffy, A.M., Chen, D.-J., Sun, S.-G. & Tong, Y.J. 2012. Origin of the current peak of negative scan in the cyclic voltammetry of methanol electro-oxidation on Pt-based electrocatalysts: a revisit to the current ratio criterion. *Journal of Materials Chemistry.* 22(11):5205-5208. DOI:https://doi.org/10.1039/C2JM15426A.

Hori, Y., Murata, A. & Takahashi, R. 1989. Formation of hydrocarbons in the electrochemical reduction of carbon dioxide at a copper electrode in aqueous solution. *Journal of the Chemical Society, Faraday*

Transactions 1: Physical Chemistry in Condensed Phases. 85(8):2309-2326. DOI:https://doi.org/10.1039/F19898502309.

Hori, Y., Murata, A., Takahashi, R. & Suzuki, S. 1988. Enhanced formation of ethylene and alcohols at ambient temperature and pressure in electrochemical reduction of carbon dioxide at a copper electrode. *Journal of the Chemical Society, Chemical Communications.* (1):17-19. DOI:https://doi.org/10.1039/C39880000017.

Hori, Y., Takahashi, I., Koga, O. & Hoshi, N. 2002. Selective Formation of C2 Compounds from Electrochemical Reduction of CO2 at a Series of Copper Single Crystal Electrodes. *The Journal of Physical Chemistry B.* 106(1):15-17. DOI:https://doi.org/10.1021/jp013478d.

Hou, X., Zhang, X., Fang, Y., Chen, S., Li, N. & Zhou, Q. 2011. 1-Hexadecylamine as both reducing agent and stabilizer to synthesize Au and Ag nanoparticles and their SERS application. *Journal of Nanoparticle Research.* 13(5):1929-1936. DOI:https://doi.org/10.1007/s11051-010-9945-y.

Hung, L.-I., Tsung, C.-K., Huang, W. & Yang, P. 2010. Room-Temperature Formation of Hollow Cu2O Nanoparticles. *Advanced Materials.* 22(17):1910-1914. DOI:https://doi.org/10.1002/adma.200903947.

Hung, L.I., Tsung, C.K., Huang, W. & Yang, P. 2010. Room-Temperature Formation of Hollow Cu2O Nanoparticles. *Advanced Materials.* 22(17):1910-1914. DOI:https://doi.org/10.1002/adma.200903947.

Jeanty, P., Scherer, C., Magori, E., Wiesner-Fleischer, K., Hinrichsen, O. & Fleischer, M. 2018. Upscaling and continuous operation of electrochemical CO2 to CO conversion in aqueous solutions on silver gas diffusion electrodes. *Journal of CO2 Utilization.* 24:454-462. DOI:https://doi.org/10.1016/j.jcou.2018.01.011.

Kas, R., Kortlever, R., Milbrat, A., Koper, M.T.M., Mul, G. & Baltrusaitis, J. 2014. Electrochemical CO2 reduction on Cu2O-derived copper nanoparticles: controlling the catalytic selectivity of hydrocarbons. *Physical Chemistry Chemical Physics.* 16(24):12194-12201. DOI:https://doi.org/10.1039/C4CP01520G.

Kim, N.R., Shin, K., Jung, I., Shim, M. & Lee, H.M. 2014. Ag–Cu Bimetallic Nanoparticles with Enhanced Resistance to Oxidation: A Combined Experimental and Theoretical Study. *The Journal of Physical Chemistry C.* 118(45):26324-26331. DOI:https://doi.org/10.1021/jp506069c.

Kuhl, K.P., Cave, E.R., Abram, D.N. & Jaramillo, T.F. 2012. New insights into the electrochemical reduction of carbon dioxide on metallic copper surfaces. *Energy & Environmental Sciences.* (5).

Kuhl, K.P., Hatsukade, T., Cave, E.R., Abram, D.N., Kibsgaard, J. & Jaramillo, T.F. 2014. Electrocatalytic Conversion of Carbon Dioxide to Methane and Methanol on Transition Metal Surfaces. *Journal of the American Chemical Society.* 136(40):14107-14113. DOI:https://doi.org/10.1021/ja505791r.

Lai, S.C.S., Lebedeva, N.P., Housmans, T.H.M. & Koper, M.T.M. 2007. Mechanisms of Carbon Monoxide and Methanol Oxidation at Single-crystal Electrodes. *Topics in Catalysis.* 46(3):320-333. DOI:https://doi.org/10.1007/s11244-007-9010-y.

LaMer, V.K. & Dinegar, R.H. 1950. Theory, Production and Mechanism of Formation of Monodispersed Hydrosols. *Journal of the American Chemical Society.* 72(11):4847-4854. DOI:https://doi.org/10.1021/ja01167a001.

Le, M., Ren, M., Zhang, Z., Sprunger, P.T., Kurtz, R.L. & Flake, J.C. 2011. Electrochemical Reduction of CO2 to CH3OH at Copper Oxide Surfaces. *Journal of The Electrochemical Society.* 158(5):45-49. DOI:https://doi.org/10.1149/1.3561636.

Li, C.W. & Kanan, M.W. 2012. CO2 Reduction at Low Overpotential on Cu Electrodes Resulting from the Reduction of Thick Cu2O Films. *Journal of the American Chemical Society.* 134(17):7231-7234. DOI:10.1021/ja3010978.

Lu, X., Leung, D.Y.C., Wang, H., Maroto-Valer, M.M. & Xuan, J. 2016. A pH-differential dual-electrolyte microfluidic electrochemical cells for CO2 utilization. *Renewable Energy.* 95:277-285. DOI:https://doi.org/10.1016/j.renene.2016.04.021.

Ma, S., Sadakiyo, M., Heima, M., Luo, R., Haasch, R.T., Gold, J.I., Yamauchi, M. & Kenis, P.J.A. 2017. Electroreduction of Carbon Dioxide to Hydrocarbons Using Bimetallic Cu–Pd Catalysts with Different Mixing Patterns. *Journal of the American Chemical Society.* 139(1):47-50. DOI:https://doi.org/10.1021/jacs.6b10740.

Mancharan, R. & Goodenough, J.B. 1992. Methanol oxidation in acid on ordered NiTi. *Journal of Materials Chemistry.* 2(8):875-887. DOI:https://doi.org/10.1039/JM9920200875.

Manthiram, K., Beberwyck, B.J. & Alivisatos, A.P. 2014. Enhanced Electrochemical Methanation of Carbon Dioxide with a Dispersible Nanoscale Copper Catalyst. *Journal of the American Chemical Society.* 136(38):13319-13325. DOI:https://doi.org/10.1021/ja5065284.

Mistry, H., Varela, A.S., Bonifacio, C.S., Zegkinoglou, I., Sinev, I., Choi, Y.-W., Kisslinger, K., Stach, E.A. et al. 2016. Highly selective plasma-activated copper catalysts for carbon dioxide reduction to ethylene. *Nature Communications.* 7.

Mourdikoudis, S., Pallares, R.M. & Thanh, N.T.K. 2018. Characterization techniques for nanoparticles: comparison and complementarity upon studying nanoparticle properties. *Nanoscale.* 10(27):12871-12934. DOI:https://doi.org/10.1039/C8NR02278J.

Nie, X., Esopi, M.R., Janik, M.J. & Asthagiri, A. 2013. Selectivity of CO2 Reduction on Copper Electrodes: The Role of the Kinetics of Elementary Steps. *Angewandte Chemie International Edition.* 52(9):2459-2462. DOI:https://doi.org/10.1002/anie.201208320.

Parveen, F., Sannakki, B., Mandke, M.V. & Pathan, H.M. 2016. Copper nanoparticles: Synthesis methods and its light harvesting performance. *Solar Energy Materials and Solar Cells.* 144:371-382. DOI:https://doi.org/10.1016/j.solmat.2015.08.033.

Peterson, A.A. & Nørskov, J.K. 2012. Activity Descriptors for CO2 Electroreduction to Methane on Transition-Metal Catalysts. *The Journal of Physical Chemistry Letters.* 3(2):251-258. DOI:https://doi.org/10.1021/jz201461p.

Polte, J. 2015. Fundamental growth principles of colloidal metal nanoparticles – a new perspective. *CrystEngComm.* 17(36):6809-6830. DOI:https://doi.org/10.1039/C5CE01014D.

Qiao, J., Liu, Y., Hong, F. & Zhang, J. 2014. A review of catalysts for the electroreduction of carbon dioxide to produce low-carbon fuels. *Chemical Society Reviews.* 43(2):631-675. DOI:https://doi.org/10.1039/C3CS60323G.

Quang Huy, T., Van Quy, N. & Anh-Tuan, L. 2013. Silver nanoparticles: synthesis, properties, toxicology, applications and perspectives. *Advances in Natural Sciences: Nanoscience and Nanotechnology.* 4(3):033001. Available: http://stacks.iop.org/2043-6262/4/i=3/a=033001.

Schouten, Perez Gallent, E. & Koper, M.T.M. 2013. Structure Sensitivity of the Electrocehmical Reduction of Carbon Monoxide on Copper Single Crystals. *ACS Catalysis.* 3(6):1292-1295.

Schouten, Kwon, Y., van der Ham, C.J.M., Qin, Z. & Koper, M.T.M. 2011. A new mechanism for the selectivity to C1 and C2 species in the electrochemical reduction of carbon dioxide on copper electrodes. *Chemical Science.* 2(10):1902-1909. DOI:https://doi.org/10.1039/C1SC00277E.

Seland, F., Tunold, R. & Harrington, D.A. 2010. Activating and deactivating mass transport effects in methanol and formic acid oxidation on platinum electrodes. *Electrochimica Acta.* 55(9):3384-3391. DOI:https://doi.org/10.1016/j.electacta.2010.01.040.

Shang, S., Kunwar, A., Wang, Y., Qi, X., Ma, H. & Wang, Y. 2018. Synthesis of Cu@Ag core–shell nanoparticles for characterization of thermal stability and electric resistivity. *Applied Physics A.* 124(7):492. DOI:https://doi.org/10.1007/s00339-018-1887-8.

Sharma, S. & Pollet, B.G. 2012. Support materials for PEMFC and DMFC electrocatalysts—A review. *Journal of Power Sources.* 208:96-119. DOI:https://doi.org/10.1016/j.jpowsour.2012.02.011.

She, Y., Lu, Z., Fan, W., Jewell, S. & Leung, M.K.H. 2014. Facile preparation of PdNi/rGO and its electrocatalytic performance towards formic acid oxidation. *Journal of Materials Chemistry A.* 2(11):3894-3898. DOI:https://doi.org/10.1039/C3TA14546H.

Singh, S., Gautam, R.K., Malik, K. & Verma, A. 2017. Ag-Co bimetallic catalyst for electrochemical reduction of CO2 to value added products. *Journal of CO2 Utilization.* 18:139-146. DOI:https://doi.org/10.1016/j.jcou.2017.01.022.

Thi My Dung, D., Thi Thu Tuyet, L., Eric, F.-B. & Mau Chien, D. 2011. The influence of solvents and surfactants on the preparation of copper nanoparticles by a chemical reduction method. *Advances in Natural Sciences: Nanoscience and Nanotechnology.* 2(2):025004. Available: http://stacks.iop.org/2043-6262/2/i=2/a=025004.

Varela, A.S., Kroschel, M., Reier, T. & Strasser, P. 2016. Controlling the selectivity of CO2 electroreduction on copper: The effect of the electrolyte concentration and the importance of the local pH. *Catalysis Today.* 260:8-13. DOI:https://doi.org/10.1016/j.cattod.2015.06.009.

Xu, J., Yuan, D., Yang, F., Mei, D., Zhang, Z. & Chen, Y.-X. 2013. On the mechanism of the direct pathway for formic acid oxidation at a Pt(111) electrode. *Physical Chemistry Chemical Physics.* 15(12):4367-4376. DOI:https://doi.org/10.1039/C3CP44074E.

Yu, W., Xie, H., Chen, L., Li, Y. & Zhang, C. 2009. Synthesis and Characterization of Monodispersed Copper Colloids in Polar Solvents. *Nanoscale Research Letters.* 4(5):465. DOI:https://doi.org/10.1007/s11671-009-9264-3.

Zhang, J. 2008. *PEM Fuel Cell Electrocatalysts and Catalyst Layers.* Springer.

Zhang, J. & Oloman, C.W. 2005. Electro-Oxidation of Carbonate in Aqueous Solution on a Platinum Rotating Ring Disk Electrode. *Journal of Applied Electrochemistry.* 35(10):945-953. DOI:https://doi.org/10.1007/s10800-005-7078-2.

Zhang, Z., Ji, Y., Li, J., Zhong, Z. & Su, F. 2015. Synergistic effect in bimetallic copper–silver (CuxAg) nanoparticles enhances silicon conversion in Rochow reaction. *RSC Advances.* 5(67):54364-54371. DOI:https://doi.org/10.1039/C5RA04575D.

Zheng, J., Sheng, W., Zhuang, Z., Xu, B. & Yan, Y. 2016. Universal dependence oxidation and evolution reaction activity of platinum-group metals on pH and hydrogen binding energy. *American Association for the Advancement of Science.* 2.

Zhu, X., Gupta, K., Bersani, M., Darr, J.A., Shearing, P.R. & Brett, D.J.L. 2018. Electrochemical reduction of carbon dioxide on copper-based nanocatalysts using the rotating ring-disc electrode. *Electrochimica Acta.* 283:1037-1044. DOI:https://doi.org/10.1016/j.electacta.2018.07.025.